Department of Precision and Microsystems Engineering

OPTIMIZATION OF CONTROLLED MOTION SYSTEMS USING ROBUSTNESS RESPONSE SURFACES

Ruben Willemen

Report no : 2022.017
Coach : Ir. A. Delissen
Professor : Dr. Ir. M. Langelaar
Specialisation : Mechatronic System Design
Type of report : Master thesis
Date : 10-05-2022

Optimization of Controlled Motion Systems using Robustness Response Surfaces

by

R. Willemen

to obtain the degree of Master of Science
at the Delft University of Technology,
to be defended publicly on Tuesday May 24, 2022 at 03:30 PM.

Student number:	4490525	
Project duration:	November, 2019 – May, 2022	
Thesis committee:	Dr. ir. M. Langelaar,	TU Delft, supervisor
	Dr. H. HosseinNia,	TU Delft
	Ir. A. Delissen,	TU Delft, supervisor

An electronic version of this thesis is available at `http://repository.tudelft.nl/`.

Abstract

An important aspect of designing high performance feedback-controlled motion systems is stability as a pitfall of feedback control is that it can make a system unstable, even if the uncontrolled system is stable. The performance is lost when instability occurs and therefore it is crucial to consider stability in design and analysis. Besides the importance of stability in general, it becomes more challenging with increasing performance requirements.

The concept of optimal design can aid in designing controlled motion systems. Using optimization can be of great help to the designer to determine actuator and sensor configurations or to design structural components. Consecutively optimizing/designing the components leads to sub-optimal performance. Simultaneously optimizing two or more components results in better performance compared to a design approach in which the components are designed consecutively.

In this thesis, a method is presented for designing one or more components of a controlled motion system using optimization. During the optimization process, the set of modes that violates the stability criterion might change. This is not desired from an optimization point of view. Therefore, a key aspect of this method is to ensure stability by imposing a constraint regarding the stability of each vibration individually considered in the model. The stability constraint, as proposed in this thesis, aids in well-performing optimization that converge to feasible designs.

A new way of modeling the open-loop response is presented. It uses a standard PID controller often used in industry and the structural model is a function of the poles and zeros of the system instead of the conventional modal parameters. Only three parameters are required to evaluate the robustness of a single mode. Using this model a robustness response surface was obtained via simulations and put into a mathematical model using NURBS. The robustness response surface is used in the evaluation of the proposed robustness constraint. The surface model is suited for gradient-based optimization methods.

The proposed method was tested on a relatively simple model of a motion system. Even though the test case is relatively simple, it is representative of more complex systems as this system possesses the aspects that are important in controlled motion system design. The optimizer converged to unconventional solutions that in most cases outperformed designs obtained using engineering principles.

Preface

This thesis describes a new approach to designing control motion systems. It is a product of my final master's project which is the last and final requirement in obtaining the degree of Master of Science in Mechanical Engineering at the Delft University of Technology. I did this project within the Structural Optimization and Mechanics group at the Department of Precision and Microsystems Engineering.

It is an understatement to say that this project lasted 'a bit longer' and I experienced ups and downs along the way. I owe my thanks to many people who supported me during this journey. Hereby I would like to mention a few of these people.

First of all, I would like to thank Matthijs and Arnoud, my supervisors for this project, for their advice, feedback, and support.

I would also like to thank the students I met during the master's program and with whom I experienced great times studying and relaxing. Special thanks to Ricardo and Lodewijk, who are true friends since day one of the bachelor's program.

Last but not least I thank my parents, brother, and sister. Their love and support are unconditional.

R. Willemen
Delft, May 2022

Contents

1 Introduction

1.1. Designing controlled motion systems

Many industrial processes and scientific measurements require accurate and/or fast motions. Examples from the field of microscopy are the Atomic Force Microscope (AFM) and the Scanning Electron Microscope (SEM). These microscopes perform very accurate scanning motions to get a clear image of the sample. Furthermore, speed and accuracy are factors that determine the performance of printing systems, see Figure 1.1, in terms of resolution and throughput. Also, one can find many examples in the semiconductor industry. Photolithography, an essential step in computer chip manufacturing, is one example. A lithography system is shown in Figure 1.3. In this system a positioning system aligns the substrate with the illumination system before exposure and measuring, shown in Figure 1.2. The positioning accuracy for this alignment is within the subnanometer range. This accuracy is needed to achieve the small features on the computer chip and is related to the speed and efficiency of the computer chip. Other steps in computer chip manufacturing that employ accurate and fast motions are wire bonding, assembly, and inspection. In the examples mentioned, a Controlled Motion System (CMS) provides the movement and is responsible that this movement meets the requirements.

Controlled motion systems are mechatronic systems that generally consist of a structural component, an actuation system, a sensing system, and a control part. The dynamics of these components, as well as the interaction between them, partly determine the systems' performance. The performance also depends on the nature (the frequency content and intensity) of disturbances and how well the system can reject these. Designing these systems is thus far from trivial, and the overall performance is a complex interplay between the individual components mentioned in combination with the disturbances, which are unique for every design challenge. Design engineers must have knowledge and experience in multiple disciplines such as control, mechanics, and electronics to design controlled motion systems. Tools from each of these fields exist that can aid the engineer during the design process. However, combining these disciplines and tools is still a challenge. Therefore, the performance a high-tech motion system can achieve is largely determined by the experience and skillset of the design engineer.

One specific aspect that is of great importance in designing feedback-controlled motion systems is stability. The application of feedback control can introduce instability even if the uncontrolled system is stable. Instability means that the system has an unbounden response to a bounded input. The performance is lost when instability occurs, and the system is said to be out of control. Therefore stability is crucial when considering the design and analysis of feedback control systems.

1.2. Optimal design

The concept of optimal design can aid in designing motion systems [17] [7]. In optimal design, a mathematical model that consists of multiple elements describes the design problem. First, parameterization of the system creates a set of designs. The design variables that describe a design are combined in the so-called design vector $\mathbf{x}$. The next element is the objective function $f(\mathbf{x})$ that describes the performance of the system mathematically. This objective is either maximized or minimized during the optimization. The last elements

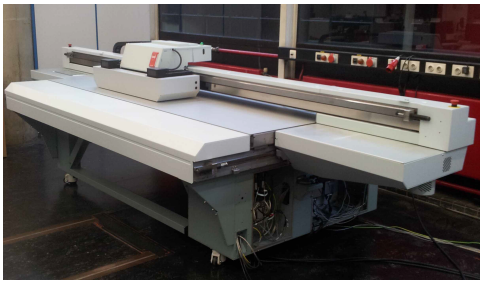

Figure 1.1: Industrial flatbed printer. adopted from [16].

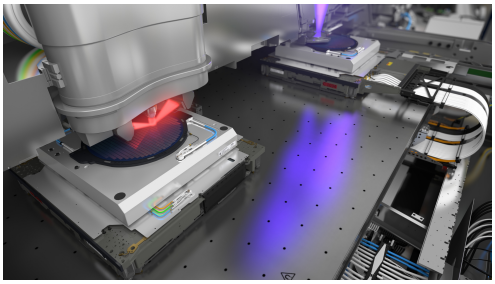

Figure 1.2: Inside the ASML's TWINSCAN NXE:3400C depicted in Figure 1.3. The wafer stage performs extreme accurate motions for exposing (right) and measuring (left).

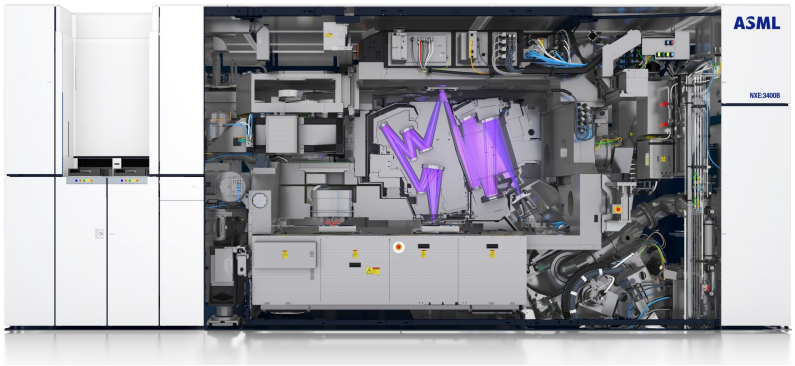

Figure 1.3: Lithography system of ASML: the TWINSCAN NXE:3400C.

are the constraints. Two types of constraints exist, equality constraints $\mathbf{h}(\mathbf{x}) = \mathbf{0}$ and inequality constraints $\mathbf{g}(\mathbf{x}) \leq \mathbf{0}$ that must be satisfied at the end of the optimization. The formal formulation of an optimization problem is:

$$\begin{aligned} \text{minimize} \quad & f(\mathbf{x}) \\ \text{subject to} \quad & \mathbf{h}(\mathbf{x}) = \mathbf{0}, \\ & \mathbf{g}(\mathbf{x}) \leq \mathbf{0}, \\ & \mathbf{x} \in \chi \subseteq \mathcal{R}^n. \end{aligned} \tag{1.1}$$

Using optimization can be of great help to the designer. One example is determining the actuator and sensor locations, as these strongly affect the performance of motion systems. A poorly chosen actuator configuration can induce structural vibrations, which can significantly limit the system's bandwidth. On the other hand, with a poorly chosen sensor configuration, the measurement picks up structural vibrations that limit the maximum performance. Two concepts from control theory [29] have often been applied in determining actuator and sensor locations via optimization. The first concept is the use of measures of controllability and observability. The second concept is using so-called system norms such as the $\mathscr{H}_2$-norm and $\mathscr{H}_\infty$-norm. These measures provide quantitative information on the presence of mode dynamics in a controlled system, and mode dynamics are a detrimental factor in the performance of controlled motion systems. Minimizing these measures could have potential in designing motion systems.

Another example of using optimization for control motion systems is the use of Structural Optimization (SO) [21] to design the structural components. SO is a method to determine the structural layout that maximizes performance using optimization. How this performance is defined depends on the design problem. With motion systems, the performance is often related to the dynamic properties of the structure, such as maximizing the lowest eigenfrequency. A last example is the use of optimization techniques in selecting the most appropriate control law and its parameters [28].

Consecutively optimizing the components using the techniques mentioned above leads to sub-optimal performance. Simultaneously optimizing two or more components results in better performance compared to a design approach in which the components are designed consecutively. Van der Veen et al. [24] used an integrated optimization approach for precision motion system design by selecting the structural topology and controller bandwidth simultaneously. Wang et al. [26] optimized a motion system by simultaneously selecting the structural topology, actuator locations, and controller parameters. While the holy grail of an integrated optimization framework that addresses the system as a whole is not within reach, there are still many opportunities for integrated optimization to explore. This thesis explores a new integrated optimization framework approach.

1.3. Research goals

The main goal of this research is to develop and test a new integrated optimization approach that can aid in the design of controlled motion systems. Integrated optimization refers to simultaneously optimizing the controller with one or more mechanical aspects, like the actuator location, sensor location, and structure. The starting point of this thesis is a *small idea* that has not been explored yet but might be worth exploring. This idea involves deriving a stability response surface that can be used to evaluate the robustness of controlled motion system designs. A model of the robustness response surface enables the application of gradient-based optimization algorithms and computationally efficient evaluations. These stability response surfaces can be used as constraints in a constrained optimization problem. To come to a new optimization approach the following subgoals are defined:

- Investigate the use of placement criteria proposed in the literature in designing controlled motion systems. Determine whether these criteria could be useful in obtaining good designs.
- Derive the stability response surface for a single-mode system.
- Extend the idea of the derived stability response surface for a single-mode system to a multi-mode system.
- Investigate the use of the stability response surface in a constrained optimization problem and explore its strengths and weaknesses.

In general, vibrations are the limiting factor of feedback-controlled motion systems. Therefore only the dynamics of the controller and the structural component are considered in this thesis. The dynamics of the sensor, actuator, and amplifiers are out of scope.

1.4. Outline

The remainder of this thesis is organized as follows. Chapter 2 provides background information on modeling of the structure and controller, and a test case of a simple controlled motion system that will be used throughout this thesis is defined.

Chapter 3 starts with a discussion on concepts of control theory. It first covers optimization criteria for actuator and sensor placement found in the literature which are based on these concepts. The second part of Chapter 3 looks into the usefulness of these criteria in designing controlled motion systems via simulations of a simple test case. Based on the simulation results, the chapter concludes with the finding that the criteria are not optimal in designing controlled motion systems and that a new approach is worth exploring.

Chapter 4 describes a new optimization approach for determining actuator and sensor locations and is the main contribution of this work. The chapter starts with a review on stability and robustness, two fundamental concepts in controlled motion system design. Then a mathematical model of a controlled motion system comprising one rigid-body mode and one flexible mode is derived. This model is then used to construct a so-called stability response surface. The surface can be used to quickly determine if a design of a single-mode system is robust or not. The idea of the stability response surface is extended to multi-mode systems. Finally, a mathematical model of the obtained stability surfaces is made using non-uniform rational B-splines (NURBS). The NURBS surfaces are suited to use in gradient-based optimization.

Chapter 5 proposes a new optimization approach that uses the stability response surfaces derived in Chapter 3 as constraints. After defining a relevant case, various tests are conducted to get insight into the strength and weaknesses of this new approach. First, actuator placement is considered. Then an integrated optimization of actuator and sensor placement is studied. Finally, structural optimization and a fully integrated optimization are performed.

Chapter 6 is the final chapter and gives the conclusions and recommendations of this thesis.

2

Background

This chapter provides theory regarding controlled motion system design that is used throughout this thesis. The first three sections provide theory regarding the structural model, controller model, and stability and robustness. The last section gives a mathematical model of a test case of a motion system that is used throughout this thesis.

2.1. Structural model

Some of the placement criteria proposed in the literature make use of properties of flexible mechanical structures. Therefore, this section concisely discusses the modal state-space description and the corresponding transfer function of such systems. Starting from the discretized equation of motion of a linear mechanical system with damping (*e.g.* finite element model):

$$\begin{aligned} \mathbf{M}\ddot{\mathbf{q}}(t) + \mathbf{D}\dot{\mathbf{q}}(t) + \mathbf{K}\mathbf{q}(t) &= \mathbf{E}\mathbf{u}(t), \\ \mathbf{y}(t) &= \mathbf{F}\mathbf{q}(t), \end{aligned} \tag{2.1}$$

where $\mathbf{q}(t) \in \mathbb{R}^n$ is the nodal coordinate vector, $\mathbf{y}(t) \in \mathbb{R}^m$ is the output vector, $\mathbf{u}(t) \in \mathbb{R}^r$ is the input vector. The matrices $\mathbf{M} \in \mathbb{R}^{n\times n}$ and $\mathbf{K} \in \mathbb{R}^{n\times n}$ are the symmetric (semi-) positive definite mass and stiffness matrix respectively. The matrix $\mathbf{D} \in \mathbb{R}^{n\times n}$ is the damping matrix. The matrix $\mathbf{E} \in \mathbb{R}^{n\times r}$ is the input matrix, and $\mathbf{F} \in \mathbb{R}^{m\times n}$ is the output matrix. The system of equations in Eq. (2.1) are generally coupled and can be decoupled by transforming the nodal coordinates into the so-called modal coordinate system via the following mapping:

$$\mathbf{q}(t) \cong \boldsymbol{\Psi}\boldsymbol{\eta}(t), \tag{2.2}$$

where $\boldsymbol{\eta}(t) \in \mathbb{R}^l$ is the modal coordinate vector containing l modal degrees of freedom. The matrix $\boldsymbol{\Psi} \in \mathbb{R}^{n\times l}$ is the so-called modal matrix where each column denotes one structural mode shape obtained from the undamped eigenvalue problem given as:

$$\begin{aligned} \mathbf{K}\boldsymbol{\phi}_i &= \lambda_i \mathbf{M}\boldsymbol{\phi}_i \\ \text{s.t.} \quad \boldsymbol{\phi}_i^T \mathbf{M}\boldsymbol{\phi}_i &= 1, \end{aligned} \tag{2.3}$$

where $\boldsymbol{\phi}_i \in \mathbb{R}^n$ is the modeshape and $\sqrt{\lambda_i}$ is the undamped eigenfrequency of eigenmode i. The eigenmodes are ordered such that the condition $\lambda_{i+1} > \lambda_i$ holds. It is common practice to consider a mapping containing a subset of the first $l \ll n$ eigenmodes. Because generally, the lower eigenmodes contribute the most to the total system's motion. The contribution of a single eigenmode decreases for increasing eigenmode numbers because the potential energy of an eigenmode is proportional to the eigenfrequency squared: $E_{p,i} \propto \omega_i^2 \eta_i^2(t)$, where $\omega_i^2 = \lambda_i$. However, it may happen that a high-frequency eigenmode is of greater importance in comparison to a lower eigenmode if the frequency of a disturbance is close to that of the high-frequency mode for example. Only the first l eigenmodes are considered in this thesis and the effect of disturbances or the like on mode selection is not considered. Substitution of Eq. (2.2) into Eq. (2.1) and multiplying the left-hand side with the modal matrix transposed $\boldsymbol{\Psi}^T$ results in:

$$\begin{aligned} \mathbf{M_m}\ddot{\boldsymbol{\eta}}(t) + \mathbf{D_m}\dot{\boldsymbol{\eta}}(t) + \mathbf{K_m}\boldsymbol{\eta}(t) &= \mathbf{E_m}\mathbf{u}(t), \\ \mathbf{y}(t) &= \mathbf{F_m}\boldsymbol{\eta}(t), \end{aligned} \tag{2.4}$$

where the matrices are called modal matrices. Thus $\mathbf{M_m} \in \mathbb{R}^{l\times l}$ is the modal mass matrix, and $\mathbf{K_m} \in \mathbb{R}^{l\times l}$ is the modal stiffness matrix. The relations between the modal matrices and nodal matrices through the eigenvectors are as follows:

$$\begin{aligned}
\mathbf{M_m} &= \mathbf{\Psi}^T\mathbf{M}\mathbf{\Psi} = \mathbf{I},\\
\mathbf{K_m} &= \mathbf{\Psi}^T\mathbf{K}\mathbf{\Psi},\\
\mathbf{D_m} &= \mathbf{\Psi}^T\mathbf{D}\mathbf{\Psi},\\
\mathbf{E_m} &= \mathbf{\Psi}^T\mathbf{E},\\
\mathbf{F_m} &= \mathbf{F}\mathbf{\Psi}.
\end{aligned} \tag{2.5}$$

The eigenvectors obtained via the eigenvalue problem in Eq. (2.3) have the following orthogonality property:

$$\begin{aligned}
\boldsymbol{\phi}_i^T\mathbf{M}\boldsymbol{\phi}_j &= 0 \qquad (i \neq j),\\
\boldsymbol{\phi}_i^T\mathbf{K}\boldsymbol{\phi}_j &= 0 \qquad (i \neq j),
\end{aligned} \tag{2.6}$$

which means that the modal mass and modal stiffness matrices are diagonal matrices. This property generally does not hold for the damping matrix. Therefore damping realizes a coupling between the motions of individual eigenmodes, and the set of equations in Eq. (2.4) is still coupled. However, it can be shown [11] that this coupling is small in a lightly damped system which is often the case in mechanical structures. As a result, off-diagonal terms are set to zero, $(\mathrm{D_m})_{i,j} = 0$ for $i \neq j$, and is known as the modal damping assumption. By adopting the modal damping assumption, the system of equations in Eq. (2.4) can be rewritten in terms of modal damping coefficients and natural frequencies as follows:

$$\begin{aligned}
\ddot{\boldsymbol{\eta}}(t) + 2\mathbf{Z}\mathbf{\Omega}\dot{\boldsymbol{\eta}}(t) + \mathbf{\Omega}^2\boldsymbol{\eta}(t) &= \mathbf{M_m^{-1}}\mathbf{E_m}\mathbf{u}(t),\\
\mathbf{y}(t) &= \mathbf{F_m}\boldsymbol{\eta}(t).
\end{aligned} \tag{2.7}$$

The matrices $\mathbf{Z}$ and $\mathbf{\Omega}$ in Eq. (2.7) are diagonal matrices:

$$\begin{aligned}
\mathbf{Z} &= \mathrm{diag}(\zeta_1,\ \zeta_2,\ \cdots,\ \zeta_l),\\
\mathbf{\Omega} &= \mathrm{diag}(\omega_1,\ \omega_2,\ \cdots,\ \omega_l),
\end{aligned} \tag{2.8}$$

where ζ_l is the modal damping ratio of mode l and ω_l is the natural eigenfrequency of mode l obtained from the undamped eigenvalue problem in Eq. (2.3) in which $\lambda_i = \omega_i^2$. The system of equations in Eq. (2.7) are uncoupled in the modal coordinate $\eta(t)$ and describes the dynamics of a flexible structure in the modal form with the modal damping assumption.
The system in Eq. (2.7) can be rewritten into two different representations. The first one is the State-Space representation which, for linear time-invariant (LTI) systems, has the following form:

$$\begin{bmatrix}\dot{\mathbf{x}}(t)\\ \mathbf{y}(t)\end{bmatrix} = \begin{bmatrix}\mathbf{A} & \mathbf{B}\\ \mathbf{C} & \mathbf{D}\end{bmatrix}\begin{bmatrix}\mathbf{x}(t)\\ \mathbf{u}(t)\end{bmatrix}, \tag{2.9}$$

where $\mathbf{x}(t) \in \mathbb{R}^{2l}$ is the state of the system and $\dot{\mathbf{x}}(t) \in \mathbb{R}^{2l}$ is its derivative. The output vector $\mathbf{y}(t) \in \mathbb{R}^m$ and the input vector $\mathbf{u}(t) \in \mathbb{R}^r$ are the same as in Eq. (2.1) and Eq. (2.7). The matrix $\mathbf{A}(t) \in \mathbb{R}^{2l\times 2l}$ is the system matrix, $\mathbf{B}(t) \in \mathbb{R}^{2l\times r}$ is the input matrix, $\mathbf{C}(t) \in \mathbb{R}^{m\times 2l}$ is the output matrix, and $\mathbf{D}(t) \in \mathbb{R}^{m\times r}$ is the feedback matrix. The feedback matrix $\mathbf{D}(t)$ is zero because the output $\mathbf{y}(t)$ is not directly related to the input $\mathbf{u}(t)$ in Eq. (2.7). The feedback matrix $\mathbf{D}(t)$ will be omitted from now on. To transform the dynamic system in Eq. (2.7) into the modal state-space form in Eq. (2.9), a state vector is defined as:

$$\mathbf{x}(t) = \big(\dot{\eta}_1(t),\ \dot{\eta}_2(t),\ \cdots,\ \dot{\eta}_l(t),\ \omega_1\eta_1(t),\ \omega_2\eta_2(t),\ \cdots,\ \omega_l\eta_l(t)\big)^T, \tag{2.10}$$

where $\dot{\eta}_l(t)$ is the first time derivative of the modal coordinate $\eta_l(t)$ of mode l. The triple matrices ($\mathbf{A}$, $\mathbf{B}$, $\mathbf{C}$) in Eq. (2.9) in combination with the state vector in Eq. (2.10) that describe the system of Eq. (2.7) are:

$$\begin{aligned}
\mathbf{A} &= \begin{bmatrix}-2\mathbf{Z}\mathbf{\Omega} & -\mathbf{\Omega}\\ \mathbf{\Omega} & \mathbf{0}^{l\times l}\end{bmatrix},\\
\mathbf{B} &= \begin{bmatrix}\mathbf{M_m^{-1}}\mathbf{E_m}\\ \mathbf{0}^{l\times r}\end{bmatrix},\\
\mathbf{C} &= \begin{bmatrix}\mathbf{0}^{m\times l} & \mathbf{\Omega}^{-1}\mathbf{F_m}\end{bmatrix}.
\end{aligned} \tag{2.11}$$

Eq. (2.10) and Eq. (2.11) form the state-space description of the flexible mechanical structure in modal form, and this description is equivalent to Eq. (2.7). The difference between the two descriptions (state-space and nodal/modal coordinates) is that State-Space Analysis reduces the order of the set differential equations to 1. The second and last description describes the dynamics of the mechanical system in the frequency domain. This description is known as a transfer function of the system and is related to the matrices (**A**, **B**, **C**) as follows:

$$\mathbf{G}(\omega) = \mathbf{C}\left(j\omega\mathbf{I} - \mathbf{A}\right)^{-1}\mathbf{B}, \tag{2.12}$$

where $\mathbf{I}(t) \in \mathbb{R}^{2l\times 2l}$ is the identity matrix.
The description in Eq. (2.12) concludes this section on structural models. The descriptions discussed in this section are linear, and the modal damping assumption applies to the damping model. Both of these model decisions are valid and therefore commonly used in modeling the mechanics for the design of controlled motion systems. Using a linear model is accepted because the deformations are due to vibrations that are small. The two models, state-space and transfer function, are the basis of two placement criteria proposed in the literature. The following two sections discuss these two criteria.

2.2. Controller model

The control principle mostly applied in motion systems is the classical PID-control principle, despite the development of modern control methods in recent years. Its popularity makes it interesting to use PID-control in this thesis. In control theory, a PID-controller in continuous time and frequency domain are defined as:

$$u(t) = k_p e(t) + k_i \int_0^t e(\tau)\,\mathrm{d}\tau + k_d \frac{\mathrm{d}e(t)}{\mathrm{d}t}, \text{ and} \tag{2.13}$$

$$C_{\text{pid}}(s) = \frac{u(s)}{e(s)} = \left(k_p + \frac{k_i}{s} + k_d s\right), \tag{2.14}$$

respectively, where $u(t)$ is the controller output and $e(t)$ is the error signal. The two signals are related via the three terms in Eq. (2.13): a proportional, an integral, and a derivative term. PID-control is straightforward and generally achieves the required performance, therefore an often chosen solution by mechatronics engineers. However, the main reason to use PID-control is that the transfer function is a function of just two parameters if some general guidelines are applied. These guidelines, often referred to as rules of thumb, are commonly used in the industry, and the transfer function is as follows:

$$C(s) = \frac{1}{3}\left|\frac{1}{G\left(2\pi f_c\right)}\right|\left(1 + \frac{2\pi f_i}{s} + \frac{\dfrac{s}{2\pi f_d}}{\dfrac{s}{2\pi f_t}+1}\right) = \frac{1}{3}\left|\frac{1}{G\left(2\pi f_c\right)}\right|\left(1 + \frac{2\pi f_c}{10s} + \frac{\dfrac{3s}{2\pi f_c}}{\dfrac{s}{6\pi f_c}+1}\right), \tag{2.15}$$

where f_c is the desired bandwidth frequency in Hz and $\left|\frac{1}{G(2\pi f_c)}\right|$ is the absolute gain of the plant $G(s)$ at f_c. The parameter f_i is related to the integral action and the parameters f_d and f_t to the derivative action. These three terms are expressed in terms of the bandwidth frequency f_c by applying the rules of thumb: $f_d = \frac{f_c}{3}$, $f_t = 3f_c$, and $f_i = \frac{f_c}{10}$. Figure 2.1 shows the Bode plot of the controller in Eq. (2.15). The integral action increases the loop-gain in the low-frequency region. This, in addition to the proportional action, improves the reference signal tracking accuracy and disturbance rejection. The derivative action adds a phase lead in the bandwidth frequency region so that the system is stable and provides robustness. The derivative action is cut-off in the high-frequency region by adding one extra pole. Adding an extra pole limits the gain at high frequencies and is known as tamed PID-control. The reason for "taming" the derivative action is to limit the gain at high frequencies to suppress the effect of high-frequency disturbances and sensor noise, which often consists of high frequencies.

2.3. Absolute stability and robustness

Feedback control is essential to achieve the required performance for the majority of controlled motion systems. A simplified block diagram of a typical feedback controlled system is shown in Figure 2.2.

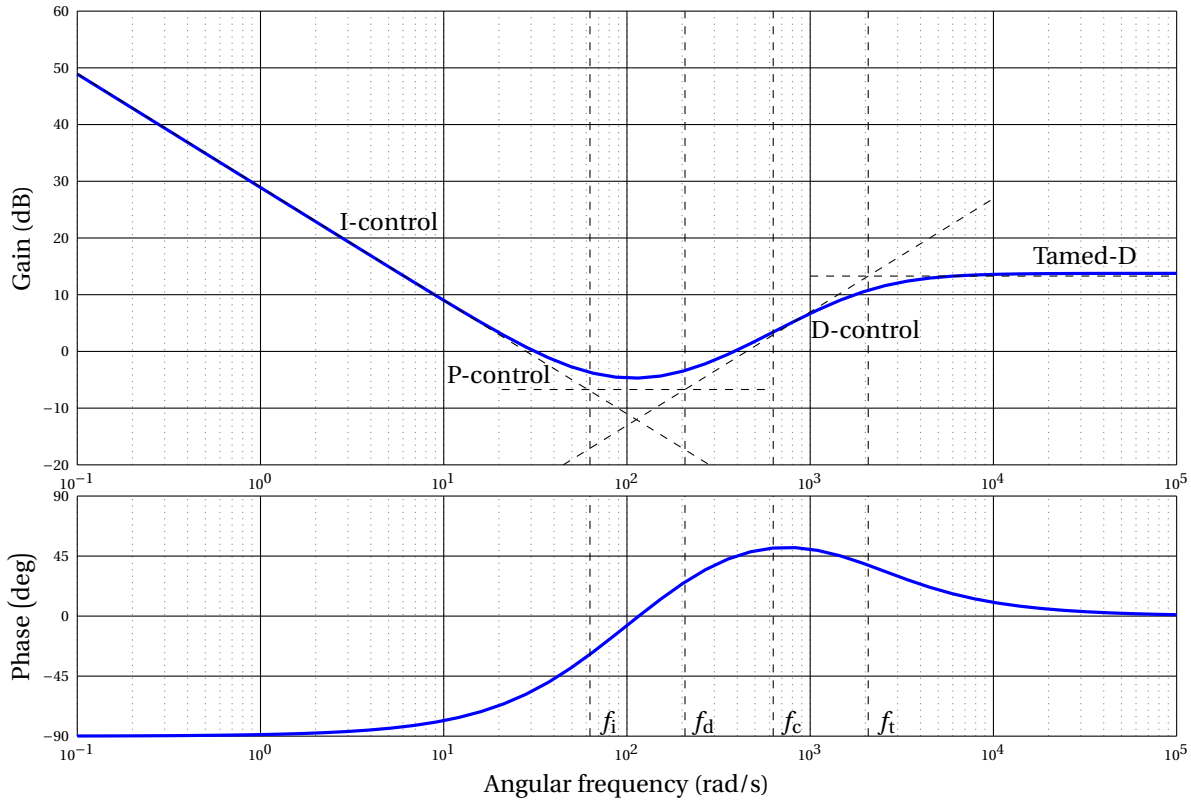

Figure 2.1: Bode plot of the tamed PID controller $C(s)$ with rules of thumb of Eq. (2.15) with $f_c = 100\text{Hz}$.

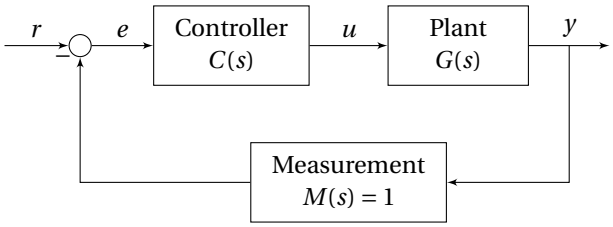

Figure 2.2: Simplified representation of a feedback loop. The measurement system does not influence the loop due to unity gain. The plant, the uncontrolled physical system, consists of the structural part only.

The measurement system measures the position which is then compared to the reference signal r. This results in an error signal e that is used to determine the correcting forces that act on the plant.
One of the main advantages of feedback control is the reduction of the effect of disturbances. Even though engineers aim to design systems that reduce external disturbances to the bare minimum, errors, yet small, are still present. In feedback control, the sensors observe disturbances so that the controller can actively suppress them. One of the other main advantages of feedback control is the handling of uncertainties. The controller design can be such that a system still meets the performance requirements, even for system parameter variations. How well a system is capable of dealing with uncertainties is known as the robustness of the system. Modeling errors and system parameters that change over time, e.g. due to bearing wear, are examples of uncertainties. On the other hand, a pitfall of feedback control is that it can introduce instability even if the uncontrolled system is stable. Instability means that the system has an unbounded response to a bounded input. The performance is lost when instability occurs, and the system is said to be out of control. Therefore stability is crucial when considering the design and analysis of feedback control systems.

Two terms to indicate system stability exist in control theory [3] [29]. The first term is absolute stability and

is a measure in a qualitative sense. It provides a yes or no answer to whether a system is stable or not stable. Further characterization of absolute stable systems is the degree of stability and is known as relative stability. Designing systems that meet a certain degree of stability is also referred to as design for robustness. Multiple tools exist to determine the absolute and relative stability of a system. One way to determine the absolute stability is by looking at the poles of the closed-loop transfer function. In this thesis, the system model consists of the structural part and the controller part only. Modeling of other aspects that usually comprise a complete motion system like sensors, actuators, and digital filters is omitted. Thus the closed-loop transfer function from the reference signal to the measured output signal, also known as the complementary sensitivity function, is defined as:

$$T(s) = \frac{y}{r} = \frac{G(s)C(s)}{1 + G(s)C(s)}, \tag{2.16}$$

where G(s) and C(s) are the transfer function of the mechanics and controller respectively. The most widely used tool in determining both absolute and relative stability is the Nyquist stability criterion. It is a frequency domain stability criterion without loopholes, hence its popularity. The criterion is based on Cauchy's argument principle [3] and relates the open-loop frequency response to the number of unstable closed-loop poles. Using Cauchy's argument principle, a so-called Nyquist diagram can be constructed. How this can be done is not discussed in this thesis, but can be found in textbooks on control [3] [29]. Figure 2.3 shows an example the Nyquist plot of the following transfer function:

$$G(s) = \frac{10}{\left(s^2 + 2s + 2\right)(s+2)}. \tag{2.17}$$

The transfer function $G(s)$ does not describe a realistic motion system or mechanical plant. It is just to show the idea of the Nyquist diagram and Nyquist stability. The blue line in Figure 2.3 is the mapping of $G(s)$

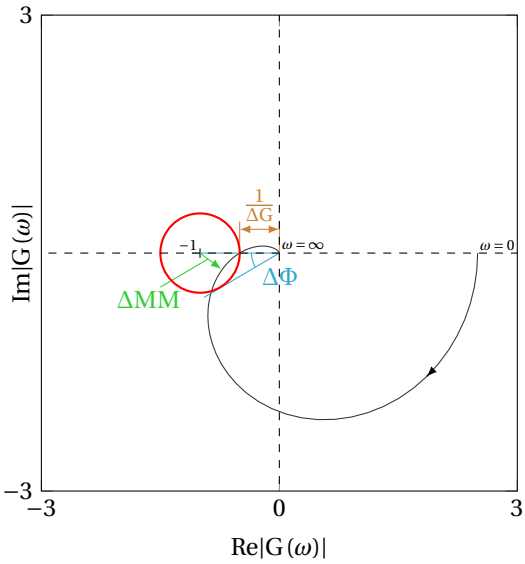

Figure 2.3: The Nyquist plot for Eq. (**??**)

on the Nyquist plot. The Nyquist stability criterion is defined in terms of the (-1, 0) point on the plot and the proximity of the blue line to this point is a measure of the relative stability. There exist three measures indicating the relative stability of a system. The first one is the gain margin and is a measure of the factor by which the system gain would have to be increased for the blue line to pass through the critical (-1, 0) point on the plot. The gain margin is mathematically defined as:

$$\Delta G = \frac{1}{\left|G\left(j\omega_{180}\right)\right|}, \tag{2.18}$$

where ω_{180} is the frequency for which the phase is $-180°$:

$$\Phi\left(\omega_{180}\right) = -180°. \tag{2.19}$$

Thus the gain margin is the gain of the open-loop system at the frequency for which the phase is $-180°$.

The second relative stability measure is the phase margin. The phase margin is the amount of phase shift at unity magnitude for the blue line to pass through the critical (-1, 0) point on the plot. The phase margin is mathematically defined as:

$$\Delta\Phi = 180° - \Phi(\omega_c), \tag{2.20}$$

where ω_c is the crossover frequency:

$$\left|OL(j\omega_c)\right| = 1. \tag{2.21}$$

The third and last relative stability margin is the modulus margin. It is defined as the shortest distance between the Nyquist contour and the critical point (-1, 0). The modulus margin is mathematically defined as:

$$\begin{aligned} \Delta\mathrm{M} = & \left|1 + OL(j\omega)\right|_{\min} \\ = & \left|S(j\omega)^{-1}\right|_{\min} \\ = & \left(\left|S(j\omega)\right|_{\max}\right)^{-1} \end{aligned}. \tag{2.22}$$

The three margins are indicated in Figure 2.3. In designing controlled motion systems a modulus margin of ΔM = 6 dB is commonly used in the industry. The standard margins used in industry for the gain margin and phase margin are ΔG = 6^{-1} dB and $\Delta\Phi = 30°$ respectively. If the modulus margin of a system is at least 6 dB, it automatically means that the system also satisfies the mentioned values of the phase and gain margin. Therefore, only the modulus margin is used in this thesis to determine if a design meets the robustness requirement. The region for which a system does not meet the requirement on the modulus margin of 6 dB is indicated with the red circle in Figure 2.3.

2.4. Test case

This section defines a test case of a simple controlled system that will be used throughout this thesis. Even though the test case is relatively simple, it is representative of more complex systems as this system possesses the aspects that are important in controlled motion system design, such are the combination of rigid-body modes and flexible modes. The simple controlled system is a two-dimensional free-free flexible beam, and the positioning task is to move it in the direction perpendicular to the longitudinal axis of this beam. The beam has a length of $L = 4m$, and the height and width are both 0.01 meters. The density of the beam is $\rho = 1000kg/m^3$ and the Young's modulus $E = 10^{10}N/m^2$. Euler-Bernoulli beam theory is used as the beam model, and the number of elements in the finite element formulation is 40. The derivation of the mass and stiffness matrices for this problem can be found in numerous finite element references [9] [8]. The system possesses two rigid-body modes, one tilt and one lift mode. Figure 2.4 shows the first eight mode shapes of the system. Mode one and mode two are the lift and tilt modes respectively, and modes three till eight are the first six flexible modes.

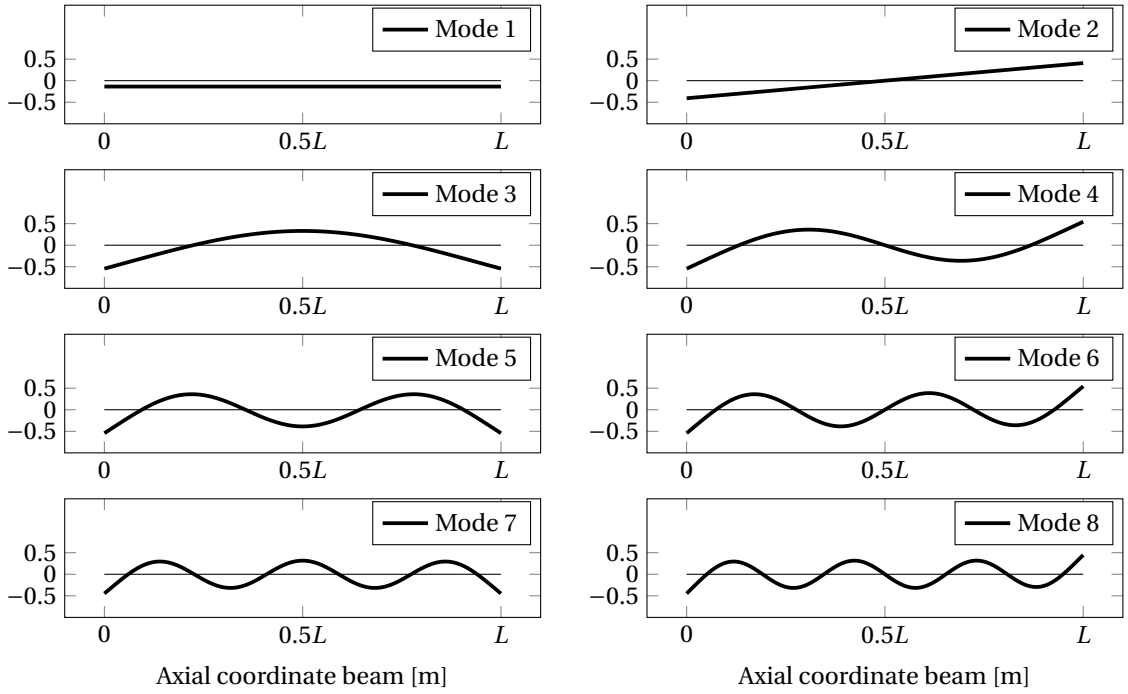

Figure 2.4: The first eight modeshapes of a free-free Euler-Bernoulli beam. Mode 1 and mode 2 are the translational and rotational modes, respectively. Modes 3 to 8 are the first six vibration modes.

Two actuators and two sensors are needed to drive the system because the system possesses two rigid-body modes. The configuration of the system, beam with the actuator and sensor arrangement, is symmetric with respect to the midpoint of the beam. Thus one parameter, a coordinate along the x-axis, is needed to determine the actuator arrangement, and the same holds for the sensor arrangement. Figure 2.5 shows a sketch of the system considered.

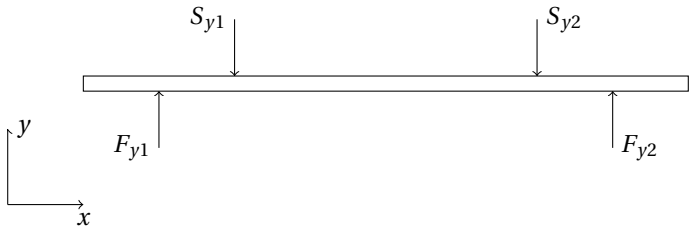

Figure 2.5: Sketch of the plant, modeled as a Bernouilli-Euler beam, and the actuator and sensor arrangement. Two actuators, F_{y1} and F_{y2}, and two sensors, S_{y1} and S_{y2}, are used to control the two rigid-body modes. The arrangement of both the actuators and sensors is symmetric. One coordinate is needed to define the positions of the two actuators and one coordinate is needed to define the positions of the two sensors.

The system model consists of a mechanical part and a control part. Models of other subsystems that normally comprise a controlled motion system, such as actuators and sensors, are omitted. The reason why only the mechanics are considered, besides the controller, is because the mechanical part is often the most determining factor for the total system performance [20]. Figure 2.6 shows the control structure of the feedback loop considered in this section.

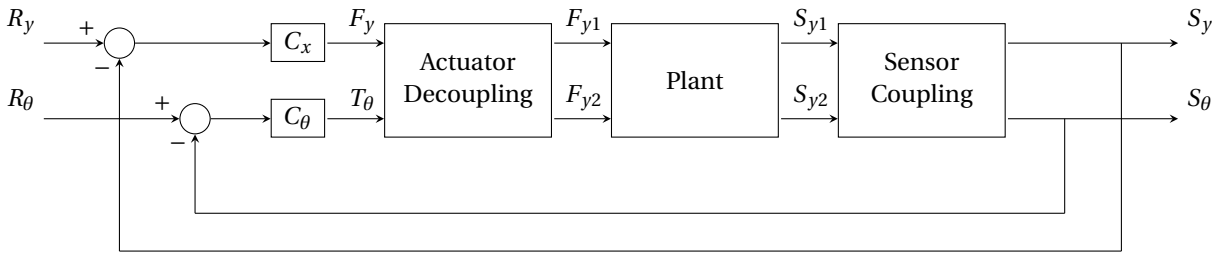

Figure 2.6: Block diagram of the control structure that is used throughout this thesis. The plant is a beam modeled as a Bernouilli-Euler beam. The sensor coupling matrix maps the two sensor measurements into the pure translation y and pure rotation θ. The actuator decoupling matrix distributes the force F_y and torque T_θ over the two actuators F_{y1} and F_{y2}.

By adopting the actuator decoupling and sensor coupling from the work of [2], two SISO control systems are realized. One system for rotation along the z-axis and one system for translation along the y-axis. In the following analysis only the control system for the translation is considered.

3

Input/Output criteria

This chapter discusses concepts from control theory that has been used by researchers to find optimal Input/Output (I/O) configurations in flexible mechanical structures. The notions of the Controllability Gramian and Observability Gramian and system norms like the $\mathscr{H}_2$-norm and $\mathscr{H}_\infty$-norm are defined. The last section discusses the limitations of the derived I/O criteria for mechatronic motion systems.

3.1. Controllability and Observability Gramians

The concepts discussed in this section are the concepts of controllability and observability. Controllability and observability are structural properties in linear time-invariant (LTI) systems in the state-space form in Eq. (2.9), discussed in the previous section. The controllability and observability for a system with triple matrices (**A**, **B**, **C**) are defined [29] as follows:

Definition 1 The dynamical system described by the pair (**A**, **B**) is said to be *controllable* if, for any initial state $x(0) = x_0$, $t_1 > 0$ and final state x_1, there exists a (piecewise continuous) input $u(t)$ such that the solution of Eq. (2.9) satisfies $x(t_1) = x_1$. Otherwise, the system or the pair (**A**, **B**) is said to be *uncontrollable*

Definition 2 The dynamical system described by the pair (**C**, **A**) is said to be *observable* if, for any $t_1 > 0$, the initial state $x(0) = x_0$ can be determined from the time history of the input $u(t)$ and the output $y(t)$ in the interval of $[0, t_1]$. Otherwise, the system, or (**C**, **A**), is said to be *unobservable*

Controllability and observability are both important properties of a control system and play a crucial role during the design process. Several qualitative criteria that provide a *yes* or *no* answer exists to determine whether a system is controllable and observable. These criteria are helpful for the control designer since these criteria are easy to compute and provide quick answers on whether or not a system is controllable and observable. However, from an optimization viewpoint, a quantitative measure indicating the degree of controllability and observability is preferred. Very efficient solution methods for optimization problems exist that use continuous model functions and continuous derivatives is the main reason [17] for the preference of quantitative measures. In control theory, the so-called controllability and observability Gramians comprise quantitative information regarding controllability and observability respectively, and are defined as:

$$\mathbf{W}_\mathrm{c}(t) = \int_0^t \mathrm{e}^{\mathbf{A}\tau}\mathbf{B}\mathbf{B}^T\mathrm{e}^{\mathbf{A}^T\tau}\mathrm{d}\tau, \tag{3.1}$$

$$\mathbf{W}_\mathrm{o}(t) = \int_0^t \mathrm{e}^{\mathbf{A}^T\tau}\mathbf{C}^T\mathbf{C}\mathrm{e}^{\mathbf{A}\tau}\mathrm{d}\tau, \tag{3.2}$$

where $\mathbf{W}_\mathrm{c}(t)$ is the controllability Gramian, $\mathbf{W}_\mathrm{o}(t)$ is the observability Gramian, and the matrices (**A**, **B**, **C**) refer to the matrices of the state-space model of the flexible mechanical system as discussed. The system is controllable if the controllability Gramian is positive definite for any $t > 0$. For the system to be observable, the observability Gramian must be positive definite for any $t > 0$. These two criteria provide a qualitative answer. However, the values of the Gramian matrices contain information on *how* controllable and observable

a system is. This fact makes the use of Gramians in optimization interesting because they are suited for well-developed solution methods. It is generally known that $\mathbf{W}_\mathrm{c}(t)$ and $\mathbf{W}_\mathrm{o}(t)$ satisfy the differential Lyapunov equations [5]:

$$\frac{\mathrm{d}\mathbf{W}_\mathrm{c}(t)}{\mathrm{d}t} = \mathbf{A}\mathbf{W}_\mathrm{c}(t) + \mathbf{W}_\mathrm{c}(t)\mathbf{A}^T + \mathbf{B}\mathbf{B}^T, \tag{3.3}$$

$$\frac{\mathrm{d}\mathbf{W}_\mathrm{o}(t)}{\mathrm{d}t} = \mathbf{A}^T\mathbf{W}_\mathrm{o}(t) + \mathbf{W}_\mathrm{o}(t)\mathbf{A} + \mathbf{C}^T\mathbf{C}. \tag{3.4}$$

When $\mathbf{A}$ is asymptotically stable, which is the case for flexible mechanical structure models without rigid body modes, then the Gramians $\mathbf{W}_\mathrm{c}(t)$ and $\mathbf{W}_\mathrm{o}(t)$ reaches a steady state for $t = T \to \infty$. The solution for the steady state Gramians are then the solution of the following Lyapunov equations:

$$\mathbf{A}\mathbf{W}_\mathrm{c} + \mathbf{W}_\mathrm{c}\mathbf{A}^T + \mathbf{B}\mathbf{B}^T = \mathbf{0}, \tag{3.5}$$

$$\mathbf{A}^T\mathbf{W}_\mathrm{o} + \mathbf{W}_\mathrm{o}\mathbf{A} + \mathbf{C}^T\mathbf{C} = \mathbf{0}. \tag{3.6}$$

Eq. (3.5) and Eq. (3.6) are not valid for systems with rigid-body modes. However, vibrations often determine the performance of controlled motion systems. Especially how vibrations are excited by forces and measured by sensors is an essential part of controlled motion system design. It is common practice to locate the actuators and sensors in the nodes of the vibration modes of the lowest order because they are most likely the most determinantal for the system performance. One interpretation of the controllability Gramain is that it contains information on the amount of energy a controller needs to provide to change a mode from one energy state to another. This interpretation becomes clear by looking at a general optimization problem in control engineering. The optimization problem is to find the control input that minimizes the control energy required to bring the system from state $\mathbf{x}_0$ at $t = 0$ to state $\mathbf{x}_T$ at $t = T$:

$$\text{minimize} \qquad J(\mathbf{u}) = \int_0^T \mathbf{u}^\mathrm{T}(t)\,\mathbf{u}(t)\,\mathrm{d}t, \tag{3.7}$$

where $\mathbf{u}(t)$ is the control input. The analytical solution for the control input [6] of an LTI system, such as the flexible structure model derived in the previous, section is given by:

$$\mathbf{u}(t) = -\mathbf{B}^\mathrm{T} e^{\mathbf{A}(T-t)}\mathbf{W}_\mathrm{c}^{-1}(T)\left(e^{\mathbf{A}T}\mathbf{x}_0 - \mathbf{x}_T\right), \tag{3.8}$$

and the corresponding control energy [6] is given by:

$$J = \left(e^{\mathbf{A}T}\mathbf{x}_0 - \mathbf{x}_T\right)^\mathrm{T}\mathbf{W}_\mathrm{c}^{-1}(T)\left(e^{\mathbf{A}T}\mathbf{x}_0 - \mathbf{x}_T\right). \tag{3.9}$$

The analytical solution in Eq. (3.8) and the corresponding energy in Eq. (3.9) only hold when the system is controllable. The term $\left(e^{\mathbf{A}T}\mathbf{x}_0 - \mathbf{x}_T\right)^\mathrm{T}\left(e^{\mathbf{A}T}\mathbf{x}_0 - \mathbf{x}_T\right)$ in Eq. (3.9) is the energy difference of the state at $t = T$ due to the free-response from $\mathbf{x}_0$ at $t = 0$ and the desired state $\mathbf{x}_T$ at $t = T$. Therefore, the controllability Gramian can be viewed as a scaling between the difference in state energy that the controller must overcome and the correct control energy to overcome this. If $\mathbf{W}_\mathrm{c}(T)$ is small or $\mathbf{W}_\mathrm{c}^{-1}(T)$ is large, it means that some state transitions require a large amount of input energy.
Based on the fact that vibrations are often the limiting factor of the performance of a controlled motion system, it can be interesting to use the Gramians in an optimization setting to determine actuator and sensor locations. For engineering purposes, it is desirable to replace the matrices with a single quality factor. Therefore, Muller and Weber [14] proposed the following three scalar criteria for optimization:

$$\begin{aligned}
&1.\quad \underset{\mathbf{x}}{\text{minimize}} \quad \overline{\lambda}\left(\mathbf{W}_\mathrm{c}(\mathbf{x}, T)^{-1}\right),\\
&2.\quad \underset{\mathbf{x}}{\text{minimize}} \quad \mathrm{tr}\left(\mathbf{W}_\mathrm{c}(\mathbf{x}, T)\right),\\
&3.\quad \underset{\mathbf{x}}{\text{minimize}} \quad \det\left(\mathbf{W}_\mathrm{c}(\mathbf{x}, T)\right),
\end{aligned} \tag{3.10}$$

where $\overline{\lambda}$ means the highest eigenvalue. The three criteria proposed by Muller and Weber are generally applicable to any dynamic system in the state-space form. Hac and Liu [6] investigated the use of the controllability Gramain as an optimization measure specifically for flexible structures in the modal state-space description. Hac and Liu show that the controllability Gramian, and thus the optimal actuator arrangement, strongly depends on the time T. The variation in optimal actuator arrangements for different times T is due to the

oscillatory nature of the homogenous response of flexible modes. Therefore Hac and Liu use the steady-state solution of the controllability Gramian to eliminate the dependence on T. Gawronski [4] and Hac and Liu [6] show that when the damping ratio's ζ_i are small, which is the case in metal structures, and the natural frequencies ω_i are well spaced, the controllability Gramian simplifies to:

$$\mathbf{W}_{\mathrm{c},i} = \mathrm{diag}\left(\frac{\beta_i}{4\zeta_i\omega_i}, \frac{\beta_i}{4\zeta_i\omega_i}\right), \tag{3.11}$$

where β_i is the sum of the actuator contributions for a particular mode:

$$\beta_i = \sum_{q=1}^{r} \boldsymbol{\phi}_i^{\mathrm{T}} \mathbf{E}(:,q), \tag{3.12}$$

where $\mathbf{E}(:,q)$ is the contribution of actuator q. With this relatively simple form of the controllablity Gramian in Eq. (3.12) ends the discussion on placement criteria based on Gramians. The discussion mainly focussed on controllability. However, the concepts of controllability and observability are complementary and this discussion also applies to the observability Gramian.

3.2. $\mathscr{H}_2$ and $\mathscr{H}_\infty$ system norms

The concepts of controllability and observability were the topic of the previous section. This section gives a short introduction of two other concepts, the so-called system norms, that have been applied often in determining actuator and sensor locations in an optimization setting. Both of these system norms are based on the transfer function in Eq. (2.12). This transfer function of the state-space system ($\mathbf{A}$, $\mathbf{B}$, $\mathbf{C}$) with m outputs and r inputs is:

$$\mathbf{G}(\omega) = \mathbf{C}\left(j\omega\mathbf{I} - \mathbf{A}\right)^{-1}\mathbf{B}, \tag{3.13}$$

where $\mathbf{G}(\omega)$ is a $m \times r$ matrix that describes the relation between the r inputs and m outputs in the frequency domain. The definition of the $\mathscr{H}_2$-norm of the system in Eq. (3.13) is defined as:

$$\|\mathrm{G}\|_2^2 = \frac{1}{2\pi}\int_{-\infty}^{\infty} \mathrm{tr}\left[\mathbf{G}^*(\omega)\,\mathbf{G}(\omega)\right] \mathrm{d}\omega, \tag{3.14}$$

where $\mathbf{G}^*(\omega)$ is the complex-conjugate transpose of $\mathbf{G}(\omega)$. The term $\mathrm{tr}\left[\mathbf{G}^*(\omega)\,\mathbf{G}(\omega)\right]$ in Eq. (3.14) is the sum of the squared magnitudes of all the elements of $\mathbf{G}(\omega)$, thus from each input to each output, and is integrated over all the frequencies. The $\mathscr{H}_2$-norm simulates an input of $F(\omega) = 1$ in the frequency domain and the inverse Fourier transform of this input is the impulse function $f(t) = \delta(t)$. Thus, an interpretation is that it is a measure for the response intensity at each output due to an impulse at each input. The $\mathscr{H}_2$-norm is related [4] to the controllability Gramian $\mathbf{W}_\mathrm{c}$ and observability Gramian $\mathbf{W}_\mathrm{o}$ via:

$$\|\mathrm{G}\|_2 = \sqrt{\mathrm{tr}\left(\mathbf{C}^T\mathbf{C}\mathbf{W}_\mathrm{c}\right)} = \sqrt{\mathrm{tr}\left(\mathbf{B}\mathbf{B}^T\mathbf{W}_\mathrm{o}\right)}. \tag{3.15}$$

T. Gawronski [4] and Hac and Liu [6] derived the controllability Gramian given in Eq. (3.12) based on two assumptions. The first assumption is that the damping ratios ζ_i are small, and the second assumption is that the natural frequencies ω_i are well spaced. Based on these two assumptions, the $\mathscr{H}_2$-norm for a single mode i can be approximated as:

$$\|\mathrm{G}_i\|_2 \cong \frac{\|\mathbf{B}_{\mathbf{m}i}\|_2\,\|\mathbf{C}_{\mathbf{m}i}\|_2}{2\sqrt{\zeta_i\omega_i}}, \tag{3.16}$$

where $\|\mathbf{B}_{\mathbf{m}i}\|_2$ and $\|\mathbf{C}_{\mathbf{m}i}\|_2$ are the norm of the modal state-space input matrix and the norm of the modal state-space output matrix of mode i respectively. The energy norm for a single mode in Eq. (3.16) shows that if that mode is uncontrollable, then there is no energy transmitted into this mode, and therefore the norm is zero. The norm is zero as well if that mode is unobservable.

The second system norm that is used in locating actuator and sensor positions in an optimization problem is the $\mathscr{H}_\infty$-norm and is defined as:

$$\|\mathrm{G}\|_\infty = \sup_{u(t)\neq 0} \frac{\|\mathbf{y}(t)\|_2}{\|\mathbf{u}(t)\|_2}, \tag{3.17}$$

or, alternatively as:

$$\|\mathrm{G}\|_\infty = \max_{\omega} \quad \sigma_{\max}\left(\mathbf{G}(\omega)\right), \tag{3.18}$$

where $\sigma_{\max}(\mathbf{G}(\omega))$ is the largest singular value of $\mathbf{G}(\omega)$. Rewritting Eq. (3.17) to 1 shows that the $\mathscr{H}_\infty$-norm provides an upper bound of the average system output to the average system input. For a single-input-single-output (SISO) system this upper bound is the peak of the transfer function. Figure 3.1 show both the $\mathscr{H}_2$-norm and $\mathscr{H}_\infty$-norm of a SISO system. The $\mathscr{H}_2$-norm is the area under the curve and the $\mathscr{H}_\infty$-norm is the highest value of $\mathbf{G}(\omega)$.

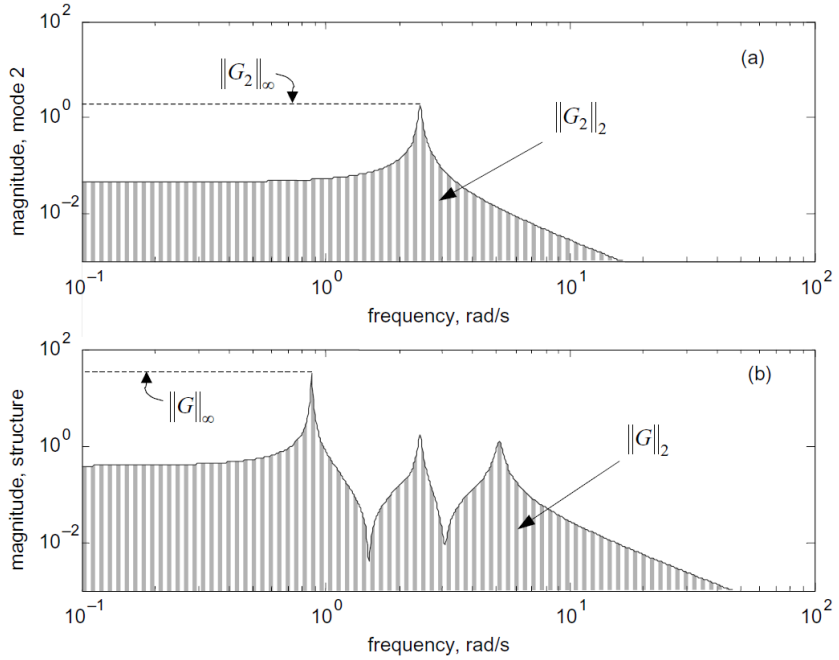

Figure 3.1: $\mathscr{H}_2$ and $\mathscr{H}_\infty$ norms (a) of a single mode; and (b) of the system.

3.3. The usefulness of criteria in designing motion systems

The criteria discussed in the previous sections are continuous functions of the actuator and sensor locations. The first-order derivatives are also continuous functions, except for a specific case. The case for which the first-order derivatives become discontinuous is shown later in this section. Apart from this particular case, the criteria are well suited to use in an optimization setting because efficient solution methods for optimization problems that use continuous model functions and continuous derivatives exist. Therefore the criteria were used a lot by researchers in determining actuator and sensor locations in an optimization setting. The majority of these optimization problems were static mechanical structures, like bridges or fixed-fixed plate, shell, or beam structures [13] [12], in which the actuators and sensors are used in active control of unwanted structural vibrations. In vibration control, the actuator and sensor configuration should result in the highest possible controllability or energy norm of the set with considered modes. There are two positive effects for a well-chosen actuator configuration. The first positive effect is that the energy required for suppressing vibrations is less relative to a system with an actuator and sensor configuration with a lower controllability or energy norm. The second positive effect is that it takes less time to bring the structure back to an acceptable state after vibrations occur. Static shape control, the second application, is about controlling one or a few modes. The modes to be controlled are often the first bending or the first torsional mode. The objective is to maximize the controllability or energy norm of the first bending or the first torsional mode while minimizing the effect of the actuators on higher-order modes. The idea is that the required energy to activate the desired mode is low while the required energy for the remaining modes is high. The literature shows that usage of the discussed criteria can aid in designing systems regarding vibration control.

However, little literature is available in which the concepts of the Gramians or energy norms are applied to motion systems with rigid-body modes. In general, vibrations are the limiting factor of feedback-controlled motion systems. Thus using the concepts of the Gramians or energy norms to minimize the effect of vibrations present in the feedback loop could be justified. However, the question arises of how effective these criteria are in designing motion systems in terms of performance. This section discusses the concepts of the Gramians and energy norms within the context of motion systems. It tries to answer how useful they are in

designing motion systems.

With the aid of the Python control toolbox [15], a Python script was written to determine the highest possible bandwidth as a function of the actuator location. The sensor locations are at x=0, x=1, x=2. Thus at 0, 25, and 50 percent of the beam. Figure 3.2 shows the normalized result of the simulation with x=2.

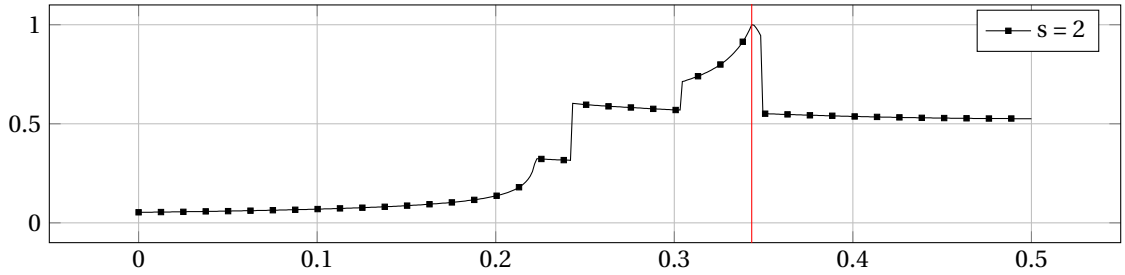

Figure 3.2: Normalized bandwidth as a function of the actuator location for sensor position s=2.

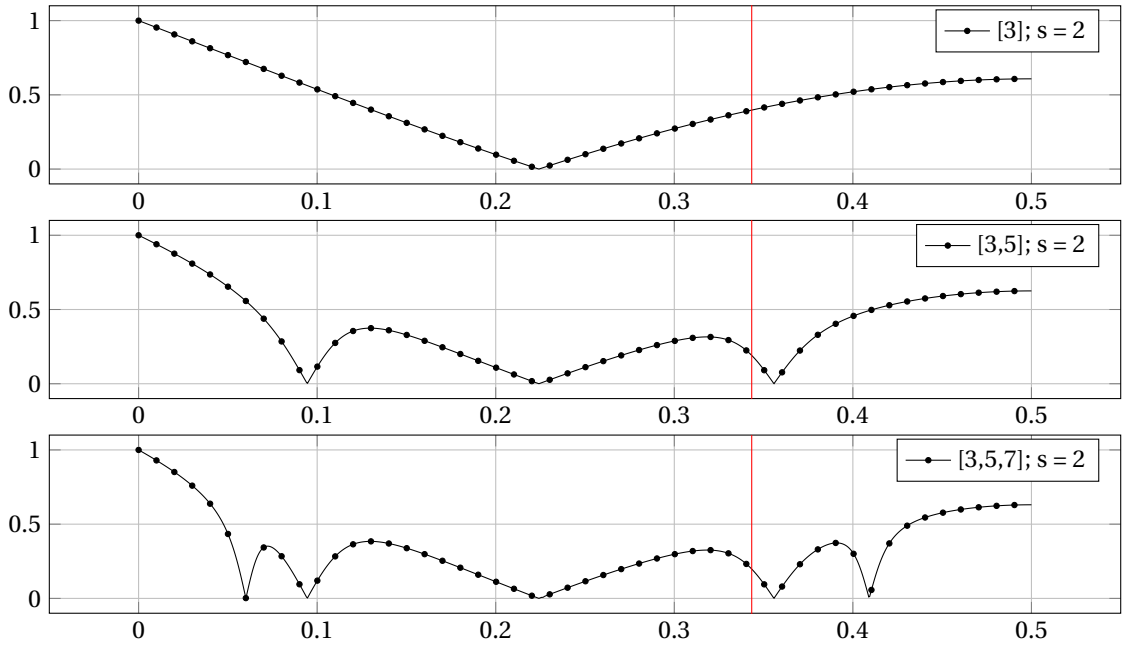

Figure 3.3: The H2-norm for three sets of modes as a function of the actuator position for sensor position s=2.

The result for $s = 2$ is compared with the H2-norm as a function of actuator location for three different sets of modes. Figure 3.3 shows the result for the H2-norm. The first thing to notice is that no single local optimum for the bandwidth coincides with a local optimum of the H2-norm. The best actuator location regarding bandwidth is at 0.34 percent of the beam or at $x = 1.14$ m. The bandwidth at this location is 494 rad/s. The local minima of the H2-norm is when the actuator is located at $x = 0.89$ m. The maximum achievable bandwidth at this location is 186 rad/s. This simple test shows that energy norms are not suited to use for optimizing controlled motion systems for which high bandwidth is important.

4

Robustness constraints

This chapter gives the derivation and modeling of stability constraints. These constraints are a central part of a new integrated optimization approach that this thesis explores. This chapter also discusses limitations, as in model assumptions, and strengths of using stability constraints. The testing of these constraints in an optimization problem is the topic of chapter 4.

4.1. Model

4.1.1. Structural model

The transfer function of a damped flexible structure can be expressed as a superposition of rigid-body modes and flexible modes:

$$G(s) = \sum_{i=1}^{m} G_i(s) + \sum_{j=m+1}^{m+n} G_j(s), \tag{4.1}$$

where the first term is the summation of the m rigid-body modal transfer functions and the second term is the summation of the n flexible modal transfer functions. The first important step is that a plant with one rigid-body and one flexible mode is considered for now. It might seem a crude oversimplification at first, which is true. Designing motion systems requires taking into account multiple flexible modes in combination with the desired rigid-body mode. The reason is that more than one mode may be close to violating the robustness criteria in a final design. Also, the set of modes that are crucial regarding stability may vary during the design process when different designs are considered, especially in optimization. However, one of the main points of this work is that, based on a simple system with only one rigid-body mode and one flexible mode, a robustness response surface can be constructed that can be used for systems with multiple modes as well. For now a system with one rigid-body mode and just one flexible mode is considered:

$$G(s) = \frac{\phi_{\text{rb,s}}\phi_{\text{rb,a}}}{\mathcal{M}_{\text{rb}}s^2} + \frac{\phi_{\text{fl,s}}\phi_{\text{fl,a}}}{\mathcal{M}_{\text{fl}}\left(s^2 + 2\zeta\omega_{\text{fl}}s + \omega_{\text{fl}}^2\right)}, \tag{4.2}$$

where $\phi_{\text{rb,s}}$ and $\phi_{\text{rb,a}}$ are the modal contributions of the rigid-body mode at the sensor location and actuator location respectively. The modal contributions to the total transfer function due to the flexible mode at the sensor location and actuator location are $\phi_{\text{fl,s}}$ and $\phi_{\text{fl,a}}$ respectively. $\mathcal{M}_{\text{rb}}$ is the modal mass of the rigid body mode and $\mathcal{M}_{\text{fl}}$ is the modal mass of the flexible mode, and ω_{fl} is the eigenfrequency of the flexible mode. The damping model is defined as $c = 2\zeta\omega_{\text{fl}}$.

Now it is generally known that machine dynamics can be detrimental on the performance of controlled motion systems. Rankers [19] investigated the effect of machine dynamics on the system performance during his Ph.D. research. Rankers identified four types of basic characteristics observed in the frequency response of mechanical systems. For the single-mode system in Eq. (4.2), the type of characteristic of the frequency response depends on the interaction between the rigid-body mode and the flexible mode. These types are

identified by introducing a variable α as

$$\alpha = \frac{\frac{\phi_{\mathrm{fl,s}}\phi_{\mathrm{fl,a}}}{\mathcal{M}_{\mathrm{fl}}}}{\frac{\phi_{\mathrm{rb,s}}\phi_{\mathrm{rb,a}}}{\mathcal{M}_{\mathrm{rb}}}}. \tag{4.3}$$

The parameter α relates the high-frequency contribution of the flexible mode to that of the rigid-body mode. The four characteristic dynamic behavior patterns are identified based on the magnitude and sign of α. Figure 4.1 shows these patterns for a single-mode system without damping ($\zeta = 0$) for different values of α. The

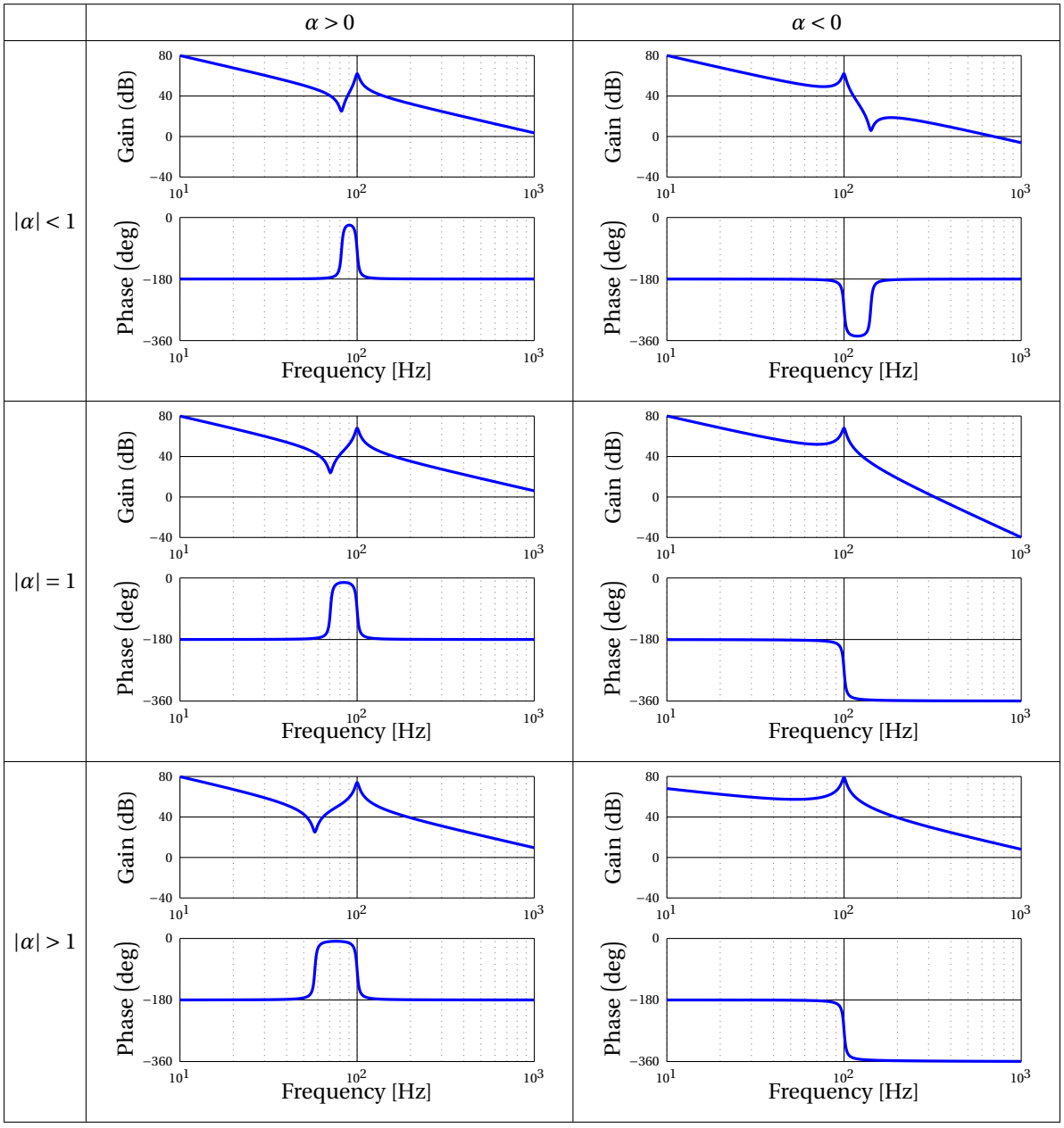

Figure 4.1: Bode plots of a system with one rigid body and one flexible mode for different values of α

dynamic response for $\alpha > 0$ is characterized by a -2slope/zero/pole/-2slope behavior. The anti-resonance (zero) is located left of the resonance (pole). The relative distance between the anti-resonance and the resonance increases as the absolute value of α becomes larger. The increasing distance is because the location of the zero shifts toward the left while the location of the pole remains unchanged. An $-1 < \alpha < 0$ results in a -2slope/pole/zero/-2slope behavior. Now the anti-resonance is located right of the resonance. The rel-

ative distance between the zero and pole increases with the increasing magnitude of alpha, while the pole location remains unchanged. The third and fourth types of system characteristics occur for $\alpha = -1$ and $\alpha < -1$. For $\alpha = -1$, the system has a -2slope/pole/-4slope behavior and if $\alpha < -1$, the systems behavior is a -2slope/pole/-2slope. No anti-resonance is present for systems that are of type three or four. One important observation that is worth mentioning at this point is that the phase always returns to $-180°$ in the high-frequency range for all systems, except if $\alpha \leq -1$. For systems with $\alpha \leq -1$ the phase goes to $-360°$ after the eigenfrequency ω_{fl} of the flexible mode. This type of behavior is called a "non-minimum phase" system which means that the system starts moving the direction opposite to the direction of the input force. This behavior type is undesired and can seriously limit the performance of a controlled motion system, especially if this behavior occurs at the lower frequency range. One note is that the value $\alpha = -1$, which is the point between non-minimum phase behavior and behavior with an anti-resonance, is true for a system with no damping. In the case of a lightly damped system, this value slightly changes as is shown later.

Now, the single-mode system of mode m can be written as a function of α instead of the conventional or textbook form in Eq. (4.2) as:

$$G_m(s) = K_m \left(\frac{1}{s^2} + \frac{\alpha_m}{s^2 + 2\zeta\omega_m s + \omega_m^2} \right), \tag{4.4}$$

where α_m is the dimensionless modal parameter of mode m. It contains information, based on the magnitude and sign, on the shape of the single-mode system, and K_m is a constant factor that is not a function of frequency. Changing K_m results in a vertical shift of the FRF, but it does not influence the 'shape' of the FRF. The interesting difference between the two descriptions is that, by combining the modal parameters into α, the 'shape' of the FRF is a function of α and the eigenfrequency of the mode ω_m only, while five parameters in Eq. (4.2) determine the shape of the FRF due to the modal contributions at the actuator and sensor locations. So α combines the modal information into one dimensionless parameter. The single-mode system structural model in the form of Eq. (4.4) will be used in the open-loop system to determine stability and robustness later on.

As mentioned before, in practice, a set of modes have to be considered during the design of a motion system. The FRF of the total system is the result of the interaction of each mode with the rest of the modes. Now the question arises how to calculate the characteristic dynamic behavior α_m, that contains information on the shape of the frequency response, of mode m that is part of a system comprising a set of modes. What follows are two methods to compute α_m. The first method is an extension of Eq. (4.3) and is only valid if modes are well-spaced. The second method uses the zeros and poles of the complete system.
The modal parameter in Eq. (4.3) is the ratio of the high-frequency contribution of the flexible mode to that of the rigid-body mode. Before deriving the mathematical expression for α_m, an assumption is made on the structural part of the system. This assumption is that the eigenfrequencies of the relevant modes are well-spaced. That the modes must be well-spaced is a vague term, and the question is 'how' well-spaced modes must be. The qualitative answer is that the effect of the resonance or anti-resonance of the previous mode is faded away enough before the interaction with mode m takes place. This depends on the value and sign of α. If the values of α of two consecutive modes are low, then the eigenfrequencies can be closer together. If this is the case, then α_m is the ratio between the high-frequency contribution of flexible mode m to the high-frequency contribution of the system comprising all the previous flexible modes including the rigid-body mode. Consider the transfer function of one rigid-body mode and m flexible modes expressed in modal parameters:

$$G(s) = \frac{\phi_{\text{rb,s}}\phi_{\text{rb,a}}}{\mathcal{M}_{\text{rb}} s^2} + \sum_{i=1}^{m-1} \frac{\phi_{i,\text{s}}\phi_{i,\text{a}}}{\mathcal{M}_i \left(s^2 + 2\zeta\omega_i s + \omega_i^2 \right)} + \frac{\phi_{m,\text{s}}\phi_{m,\text{a}}}{\mathcal{M}_m \left(s^2 + 2\zeta\omega_m s + \omega_m^2 \right)}. \tag{4.5}$$

Then α_m is the ratio between the high-frequency contribution of mode m and the sum of the high-frequency contributions of all the other modes in Eq. (4.5):

$$\begin{aligned}\alpha_m &= \lim_{s\to+\infty} \frac{\dfrac{\phi_{m,\mathrm{s}}\phi_{m,\mathrm{a}}}{\mathcal{M}_m\left(s^2+2\zeta\omega_m s+\omega_m^2\right)}}{\dfrac{\phi_{\mathrm{rb,s}}\phi_{\mathrm{rb,a}}}{\mathcal{M}_{\mathrm{rb}}s^2}+\sum_{i=1}^{m-1}\dfrac{\phi_{i,\mathrm{s}}\phi_{i,\mathrm{a}}}{\mathcal{M}_i\left(s^2+2\zeta\omega_i s+\omega_i^2\right)}}, \\ \alpha_m &= \frac{\dfrac{\phi_{m,\mathrm{s}}\phi_{m,\mathrm{a}}}{\mathcal{M}_m}}{\dfrac{\phi_{\mathrm{rb,s}}\phi_{\mathrm{rb,a}}}{\mathcal{M}_{\mathrm{rb}}}+\sum_{i=1}^{m-1}\dfrac{\phi_{i,\mathrm{s}}\phi_{i,\mathrm{a}}}{\mathcal{M}_i}}.\end{aligned} \tag{4.6}$$

It turns out that computing α_m's with Eq. (4.6) is not an accurate method for practical systems. Modes are most likely not well-spaced enough such that the dynamics of other modes do not influence the values of α_m. The second method is based on the zeros and poles of the complete system and is valid irrespective of whether modes are well-spaced or not. First, consider the case for which the mode results in an anti-resonance, thus $\alpha_m > -1$. Figure 4.2 shows the asymptotic behavior of such a system. The logarithmic scales of magnitude and frequency give a linear asymptotic behavior before and after the pole/zero pair, often called the mass-line, and have a slope of -2. Expressions for the low-frequency and high-frequency asymptotes are obtained by taking the limit of $G_m(s)$, defined in Eq. (4.4), as s approaches zero and infinity, respectively. The low-frequency asymptote L_a and high-frequency asymptote H_a are:

$$\begin{aligned}L_a &= K_m\frac{1}{s^2}, \\ H_a &= K_m\frac{(1+\alpha_m)}{s^2} = (1+\alpha_m)\,L_a.\end{aligned} \tag{4.7}$$

Eq. (4.4) learns that the level of the high-frequency asymptote H_a exceeds the low-frequency asymptote L_a by a factor $(1+\alpha_m)$.

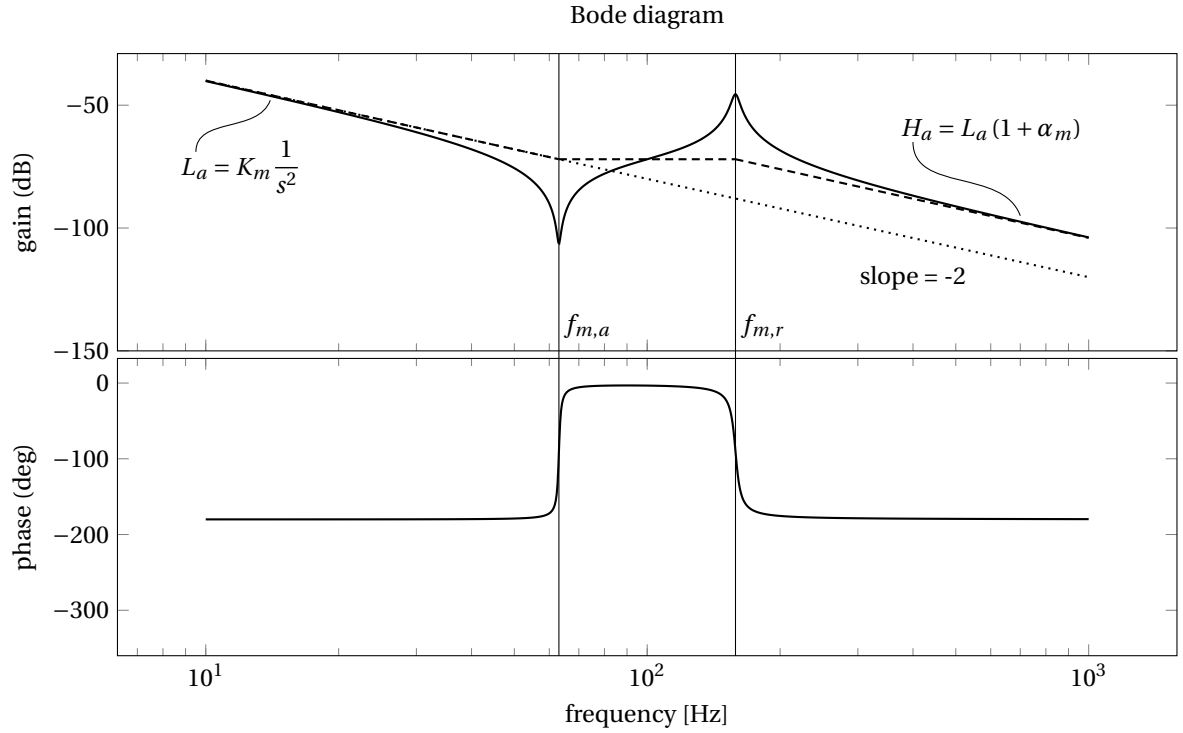

Figure 4.2: The dynamics present in the total system FRF can be approximated by single-mode systems, each of which is a function of the modal parameter α_m and the constant mapping factor K_m.

From the asymptotic behavior shown in Figure 4.2, one can deduce that the high-frequency asymptote exceeds the low-frequency asymptote by a factor $\left(f_r/f_a\right)^2$. Setting this factor equal to $(1+\alpha_m)$, the dimensionless modal parameter α_m of mode m can be expressed as a function of the poles and zeros:

$$\alpha_m = \left(\frac{f_{m,\mathrm{r}}}{f_{m,\mathrm{a}}}\right)^2 - 1, \tag{4.8}$$

where $f_{m,\mathrm{r}}$ and $f_{m,\mathrm{a}}$ are the frequency of the resonance and anti-resonance of mode m respectively. The frequency of the anti-resonance corresponds with the frequency, which is the imaginary part, of the zero z_m of mode m. The frequency of the resonance corresponds with the frequency of the pole p_m of mode m. For non-minimum phase behavior, no anti-resonance occurs. In this case, the frequency of the zero is equal to zero ($\mathrm{Im}(z_m) = 0$), and Eq. (4.8) is not valid to compute α_m anymore.

Eq. (4.4) is used to derive α_m as a function of z_m for a non-minimum phase mode. Plugging in z_m in Eq. (4.4) and solving for α_m gives the following expressions for α_m:

$$\alpha_m = -\left(\frac{\omega_m}{\mathrm{Re}(z_m)}\right)^2 - 1 - \frac{2\zeta\omega_m}{\mathrm{Re}(z_m)}, \qquad \alpha_m < \zeta^2 - 1, \tag{4.9}$$

and

$$\alpha_m = \zeta^2 - 1. \tag{4.10}$$

The boundary between non-minimum phase behavior and behavior with an anti-resonance is $\alpha = \zeta^2 - 1$ for damped systems instead of -1. This automatically means that Eq. (4.8) is valid if $\alpha_m > \zeta^2 - 1$. Now the question arises which expression to use for computing α_m. This is determined by the zero z_m. If the system has an anti-resonance due to mode m, then the zero z_m is a complex conjugate pair. If two zeros exist that are both real, one negative and one positive, than the mode is non-minimum phase and Eq. (4.9) is used to compute α_m. An example follows to show how well a set of single-mode systems can resemble the dynamics of the total plant. The plant of the test case defined in Section 2.4 is considered in this example. A two-dimensional free-free flexible beam with a length of 1 meter modeled with Euler-Bernoulli beam theory. The location of the actuator and sensor are at 0.25 and 0.1 meters, respectively. This results in a system in which the first five modes are controllable and observable, and one of these modes shows non-minimum phase behavior. The dimensionless modal parameters α are obtained via the strategy presented earlier in this section. The single-mode systems are mapped onto the corresponding pole of the total plant by computing the factor K:

$$K = \frac{\left|G_t(s)\big|_{s=j\omega_{P_m}}\right|}{\left|G_m(s)\big|_{s=j\omega_{P_m}}\right|}. \tag{4.11}$$

Figure 4.3 shows the plant together with the resulting single-mode systems. The FRF's of the single-mode systems are plotted only for the frequency range at which the dynamics of the (anti)-resonance are present. The reason is to prevent that Figure 4.3 becomes unclear due to the excess of lines.

There are two observations worth mentioning. The first one is that some single-mode systems are more capable of resembling the total plant dynamics than others. The single-mode system of mode one, for example, shows virtually no error with the dynamics in the total system FRF, while the capability of mode three to resemble the frequency range after the anti-resonance is lost quickly with the effect that this introduces an error. There is a combination of two factors that influence this error. The first one is the magnitude and sign of alpha of two consecutive modes. The dynamics of one mode extend to a broader frequency range as the magnitude of alpha increases. The first reason is that the frequency of the anti-resonance moves away from the frequency of the resonance. The second reason is that the magnitude of the dynamics is damped out less quickly for frequencies away from the (anti-)resonance. The magnitude of the dynamics of one mode superposes with the dynamics of other modes in the total system FRF, which a single-mode system can not capture. However, looking at the stability and robustness of a controlled motion system, the frequency range around the bandwidth is most crucial. The mode dynamics in this frequency range are most likely responsible for not meeting the robustness criteria or even absolute stability. Therefore, a set of single-mode systems can probably resemble the dynamics of the total plant around the bandwidth frequency because the dynamics are likely to have a small magnitude of α. The second factor that influences the error is if the eigenfrequencies

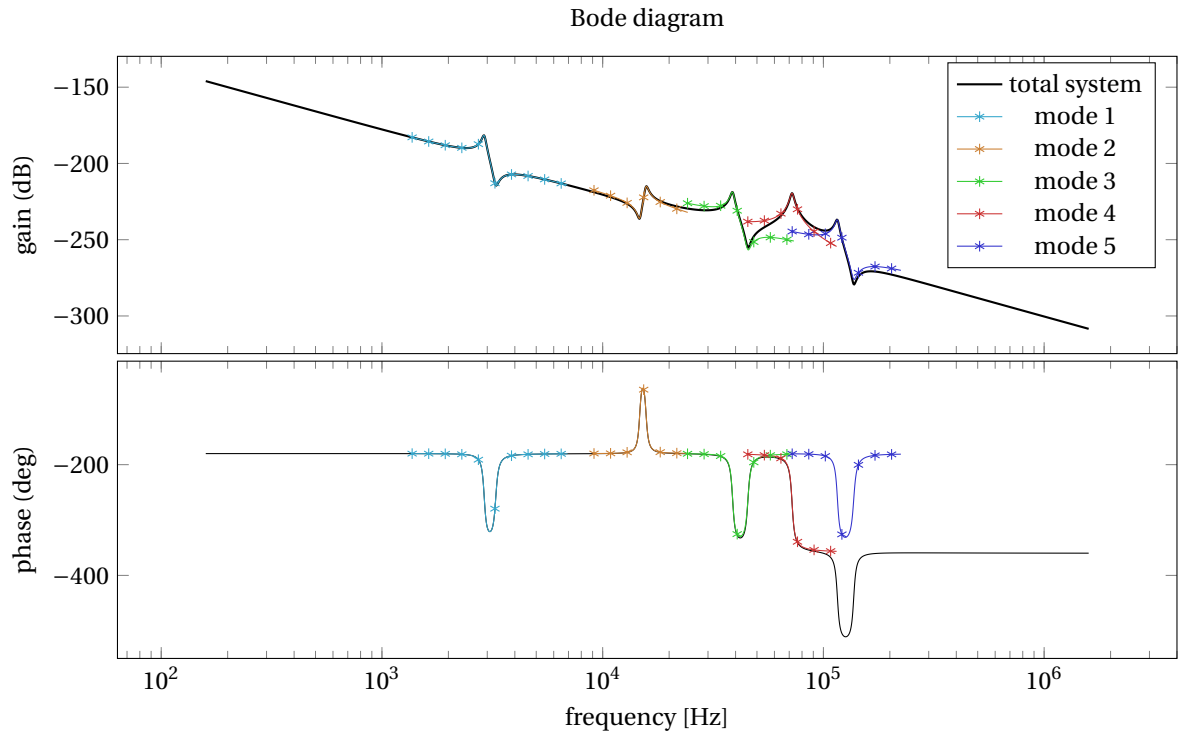

Figure 4.3: The dynamics present in the total system FRF can be approximated by single-mode systems, each of which is a function of the modal parameter α_m and the constant mapping factor K_m.

of two consecutive modes are not well-spaced. In practice, the relative distance between eigenfrequencies decreases as the mode number increases. On the other hand, the modes in the lower frequency range limit the controller bandwidth.

The fourth mode shows non-minimum phase behavior ($\alpha \leq -1$). The absence of an anti-resonance characterizes this behavior, but more importantly, a permanent phase shift of $-180°$ occurs. The permanent phase shift opposes the behavior of other system types, which always return to -180 degrees after the (anti-)resonance. The result is that the phase of the single-mode systems that come after the non-minimum phase mode is off by 180°, as shown in Figure 4.3. Non-minimum phase behavior is highly undesired as it can seriously endanger stability. In defining an optimization problem, an option is to define an inequality constraint, like $g(\boldsymbol{x}) = \alpha - 1$, to prevent non-minimum phase behavior.

4.1.2. Controller and open-loop model

The Nyquist criterion is applied to the open-loop system to determine the stability and robustness of the closed-loop system. The open-loop system is the product of the controller transfer function and the transfer function of the mechanical plant, which were discussed in the last two sections. Inserting both the mechanical model of Eq. (4.4) and controller model of Eq. (2.15) in the open-loop system, defined as $OL(s) = C(s)G(s)$, results in the following open-loop system:

$$OL_m(s) = K_m \left(\frac{1}{s^2} + \frac{\alpha_m}{s^2 + 2\zeta\omega_m s + \omega_m^2} \right) \frac{1}{3} \left| \frac{1}{G(2\pi f_c)} \right| \left(1 + \frac{2\pi f_c}{10s} + \frac{\frac{3s}{2\pi f_c}}{\frac{s}{6\pi f_c} + 1} \right), \tag{4.12}$$

where f_c is the desired bandwidth frequency in Hz. The system in Eq. (4.12) is slightly rewritten by introducing a relative bandwidth C:

$$C_m = \frac{\omega_{bw}}{\omega_m}, \tag{4.13}$$

where C is the relative bandwidth and f_{fl} is the eigenfrequency of the flexible mode in Hz. Inserting Eq. (4.13) in Eq. (4.12) results in:

$$OL_m(s) = \underbrace{K_m \frac{1}{3} \left| \frac{1}{G\left(2\pi C \omega_{fl}\right)} \right|}_{\text{gain}} \underbrace{\left(\frac{1}{s^2} + \frac{\alpha_m}{s^2 + 2\zeta\omega_m s + \omega_m^2} \right) \left(1 + \frac{2\pi C \omega_{fl}}{10s} + \frac{\frac{3s}{2\pi C \omega_{fl}}}{\frac{s}{6\pi C \omega_{fl}} + 1} \right)}_{\text{shape}}. \tag{4.14}$$

The open-loop system in Eq. (4.14) can be seen as a product of two parts. The first part is a constant gain that is independent of the frequency. The second part is a function of the frequency and describes the 'shape' of the open-loop FRF. Now the open-loop system is only a function of three parameters: α, the relative bandwidth C, and the eigenfrequency of the flexible mode ω_{fl}. Only α and C change the shape of the FRF and these parameters influence the stability and robustness. However, a change in ω_{fl} results in a horizontal shift of the FRF and does not influence the stability and robustness, which is shown in Figure 4.4. This means that

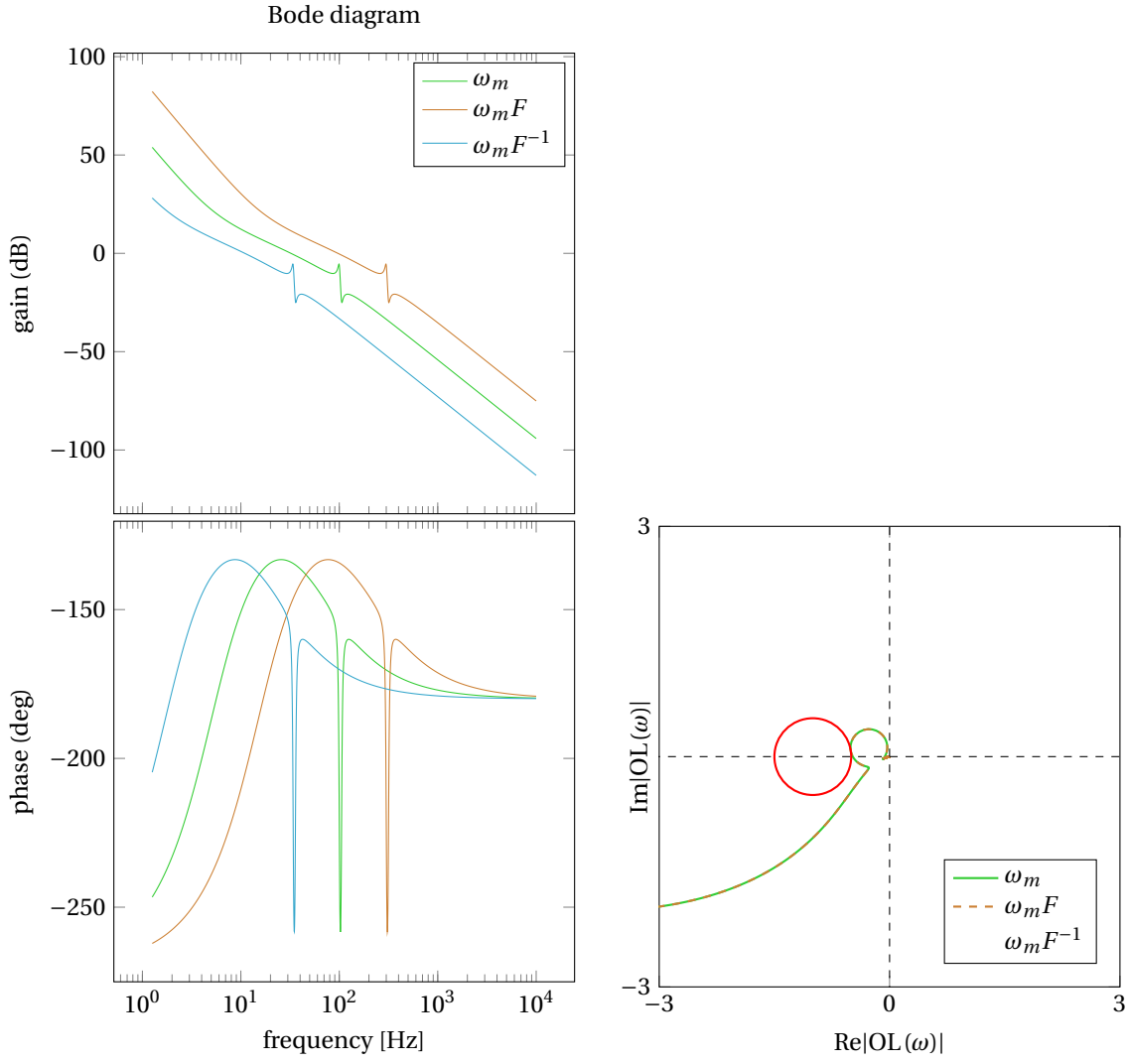

(a) Interaction

(b) Interaction

Figure 4.4: Stability and robustness of the open-loop system in Eq. (4.14) is only a function of the modal parameter α_m and the relative bandwidth C_m. (a) Three systems with different eigenfrequencies but with the same value for the modal parameter and relative bandwidth. (b) The robustness for the three system is the same.

the stability and robustness of the system in Eq. (4.14) is completely determined by just two parameters: α

and C. Thus any change in the design, whether it is a change in the topology or the location of actuators and sensors, does not influence the stability and robustness if α and C remain constant.
Now that the robustness is a function of two variables, Eq. (4.14) can be used to construct a response surface for the robustness of a closed-loop controlled system that comprises one rigid-body mode, a flexible mode, and a PID controller. The response surface is general and can be used to evaluate if a design meets the robustness criteria.

4.2. Relative stability response surface of a single-mode system

The open-loop transfer function of a controlled motion system was derived in the previous section. The derivation of this function was based on a mechanical model comprising of a rigid-body mode and just one flexible mode. This mechanical model is a crude oversimplification of reality because, in practice, a system contains infinite flexible modes. However, the derived model can be used in determining the robustness of a system comprising multiple flexible modes. Section 4.3 explains how and under what conditions. This section looks into the relative stability of the single-mode system derived in the previous section.

The stability of the system in Eq. (4.14) is a function of two parameters: α and C. The parameter α determines the shape of the plant frequency response, and C determines the shape of the controller frequency response, as discussed in the previous section. The fact that just two parameters determine stability allows visualizing the three stability margins via three-dimensional plots. The Python Programming Language [25] with the aid of the Python package "Python Control System Library" [15] is used to generate such a plot. Figure 4.5a shows the Modulus Margin ΔM in decibel as a function of positive values of α up to $\alpha = 100$ and the relative bandwidth C from three decades before to two decades after $C = 1$. The stability response surface in

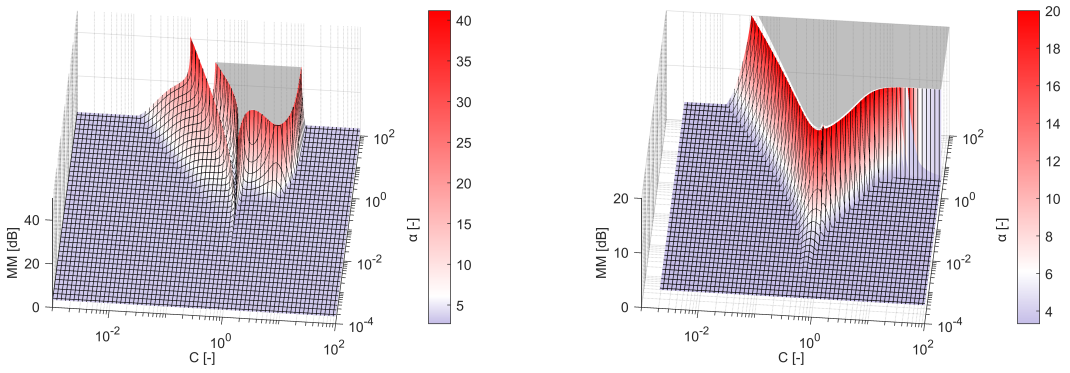

(a) Interaction (b) Interaction

Figure 4.5: The robustness response surfaces of a single-mode system for (a) positive values of α and (b) negative values of α.

Figure 4.5a reveals a plane at which the modulus margin is constant and two profiles nearby $C = 1$. The figure also shows a region indicated by a grey plane. This region is where absolute stability is not met, or in other words, where the controlled motion system is unstable. The modulus margin is not plotted in the unstable region for two reasons. The first reason is that a system must be stable in the absolute sense before one can determine relative stability. The second reason is that the modulus margin can meet the robustness criteria, even if the system is unstable. Therefore, it is not clear in Figure 4.5a whether a system is stable and robust if the unstable region is not indicated. The modulus margin goes to infinity at a point of transition from absolute stability to instability. Therefore, the surface is capped at a modulus margin of 30 dB at the transition points to make Figure 4.5a clearer.

The region of the stability response surface that complies with the robustness criteria of $\Delta M \leq 6$ dB is indicated by the color blue. For the most part, this region is a flat plane with a constant modulus margin of $\Delta M = 3.4$ dB. The mass line of the system determines the modulus margin at this plane. The resonance and anti-resonance play no role, which can be confirmed by looking at the Nyquist plot of different systems on

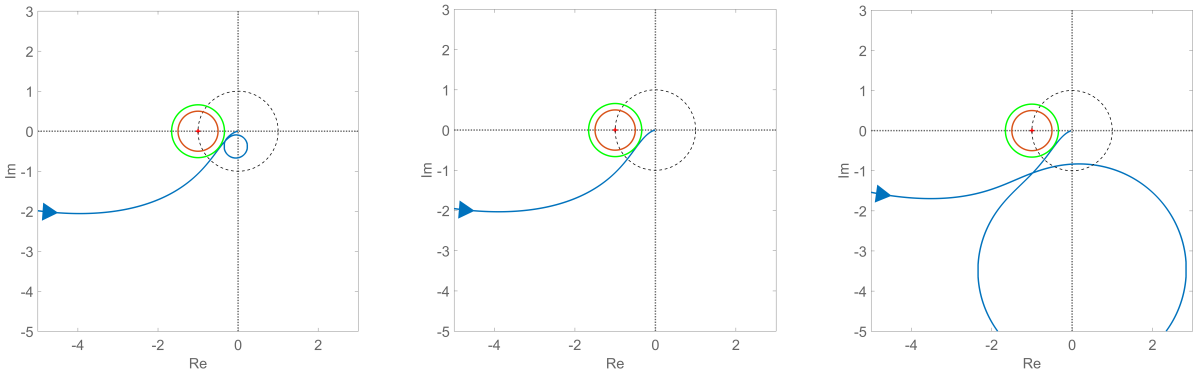

Figure 4.6: Nyquist plots for three different systems with the same modulus margin of ΔM = 3.4 dB, indicated by the green circle. For each system, the modulus margin is determined by the mass line and not by the resonance and anti-resonance.

this plane. Figure 4.6 shows the Nyquist plots of three systems evaluated at three different locations. The modal parameter of the system in the middle in Figure 4.6 is $\alpha = 0$, meaning that the system only consists of one rigid-body mode and no flexible mode. The shape of the Nyquist plot does not depend on the choice of the controller bandwidth, and the value for C is not relevant for this case. The modal parameter of the systems depicted on the left and right in Figure 4.6 is $\alpha = 0.1$. For the left system, the controller bandwidth is located left at the eigenfrequency of the flexible mode at $C = 0.35$. The modulus margin is determined by the mass line left of the eigenfrequency. The controller bandwidth of the right system is chosen right from the eigenfrequency of the flexible mode at $C = 2$. In this case, the mass line right of the eigenfrequency determines the modulus margin of the system. The surface learns that a stable motion system is feasible if the bandwidth frequency is chosen some distance from the eigenfrequency of the flexible mode. The minimum distance required increases for systems with a higher α as the resonance plays a more prominent role in the controlled system.
The stability response surface in Figure 4.5a reveals, besides the plane, two distinct profiles. It shows that robustness can be an issue if the bandwidth is close to the eigenfrequency of the flexible mode as both these profiles have regions that do not comply with the robustness criteria of $\Delta M \leq 6$. The robustness of the left

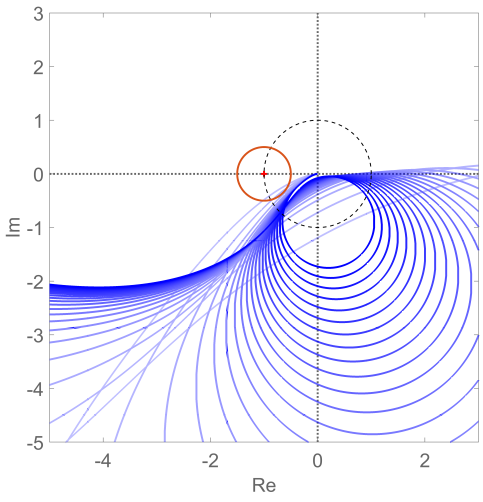

Figure 4.7: Nyquist plots of systems on the left side of left profile of the modulus response surface in Figure 4.5a.

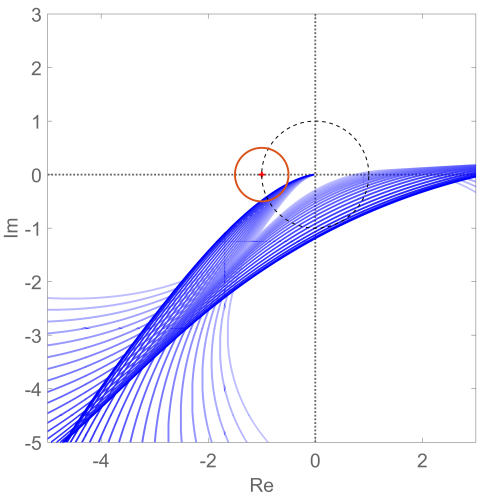

Figure 4.8: Nyquist plots of systems on the right side of left profile of the modulus response surface in Figure 4.5a.

profile in Figure 4.5a is determined by the resonance of the system. The anti-resonance determines the mod-

ulus margin of the right profile. That the left and right profile are a consequence of the resonance and anti-resonance respectively can be confirmed by looking at Nyquist plots in these regions. Figure 4.7 and Figure 4.8 show a set Nyquist plots with systems located at the left profile. Figure 4.7 shows a set of systems with constant $\alpha \approx 0.22$. The relative bandwidth is increased from $C_1 \approx 0.40$ to $C_2 \approx 0.90$. The modulus margin varies from $\Delta M_1 = 4$ dB, for which the system meets the robustness criteria, to $\Delta M_2 = 8$ dB, for which the system fails the criteria. The set of systems shown in Figure 4.8 have the same constant α as in Figure 4.7, $\alpha \approx 0.22$. But for this set the relative bandwidth is increased from $C_2 \approx 0.90$ to $C_3 \approx 0.95$. Now the modulus margin varies from $\Delta M_2 = 8$ dB back to $\Delta M_3 = 4$ dB. Both Figure 4.7 and Figure 4.8 show that the resonance of the single-mode system is determinative for the modulus margin and thus for the fact whether the robustness criteria is met or not.
Figure 4.9 and Figure 4.10 show a set Nyquist plots with systems located at the right profile in Figure 4.5a. The modal parameter is again kept constant at $\alpha \approx 0.42$. The relative bandwidth is increased from $C_4 \approx 0.95$ to $C_5 = 1$ in Figure 4.9. The modulus margin varies from $\Delta M_4 = 4$ dB, for which the system meets the robustness criteria, to $\Delta M_5 = \infty$ dB, for which the system is at a transition point between stable and unstable. In Figure 4.10 the relative bandwidth is increased from $C_5 = 1$ to $C_6 \approx 1.15$ and the modulus margin goes back from $\Delta M_5 = \infty$ dB to $\Delta M_6 = 4$ dB. Both Figure 4.9 and Figure 4.10 show that the anti-resonance of the single-mode system is determinative for the modulus margin and thus for the fact whether the robustness criteria is met or not.

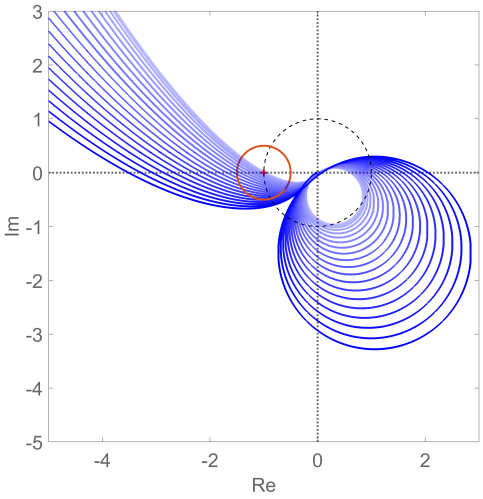

Figure 4.9: Nyquist plots of systems on the left side of right profile of the modulus response surface in Figure 4.5a.

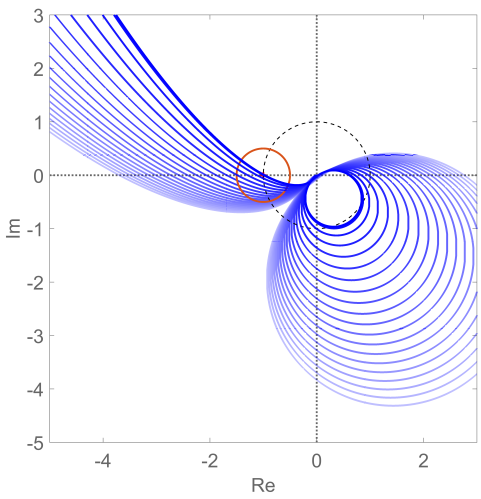

Figure 4.10: Nyquist plots of systems on the right side of right profile of the modulus response surface in Figure 4.5a.

This concludes the discussion of the stability response surfaces for a single-mode system. The following section discusses multi-mode systems. The main focus is how and under what conditions a stability response surface can be used on a multi-mode system. The reader is referred to Appendix A for the graphs and discussion of stability response surfaces for the gain margin and the phase margin. The reason is that the modulus margin is the most important in controlled system design. If the robustness criterion regarding the modulus is met, it automatically means that the system also satisfies the criteria regarding the gain and phase margins, see [20].

A similar analysis for the profile shown in Figure 4.5a could be made. However, the only thing that is mentioned here is that for $C > 1$ stability is lost if $\alpha < -1$. A system with $\alpha < -1$ is known as a non-minimum phase system as discussed and it is not possible to create a stable system if the bandwidth is placed after the resonance frequency.

4.3. Relative stability response surface of a multi-mode system

The relative stability response surfaces discussed in Section 4.2 are based on a structural system with one rigid-body mode and one flexible mode. In reality, structural systems comprise infinite flexible modes. In controlled motion system design, it must be ensured that the total system complies with the robustness criteria. The design engineer must take into account the set with the most important modes regarding performance and stability. In this section, a different version of a stability response surface is derived with the aim to use these surfaces on systems comprising multiple flexible modes.

Evaluating the robustness of a single-mode system via the stability response surface discussed in Section 4.2 requires two dimensionless parameters. The first parameter is the relative bandwidth C and is defined in Eq. (4.13) as the ratio between the bandwidth frequency f_c and the eigenfrequency of the flexible mode ω_{fl}. The definition of the relative bandwidth does not change for multiple mode systems, but each mode results in a different relative bandwidth because of the difference in eigenfrequency:

$$C_n = \frac{f_c}{\omega_n}, \tag{4.15}$$

where C_n is the relative bandwidth of mode n, f_c is the bandwidth frequency, and ω_n is the eigenfrequency of flexible mode n. The second dimensionless parameter is the modal parameter α and the computation of α_m for mode m is discussed in Section 4.1.1.

The stability response surface of a single-mode is not suited to analyze the robustness of a multi-mode system by evaluating the surface at different locations for each mode. The reason why is a shift in the gain takes place after an interaction. This shift in the gain is cumulative and can become larger or smaller with each interaction between a mode and the rest of the system. This effect is shown in Figure 4.11.

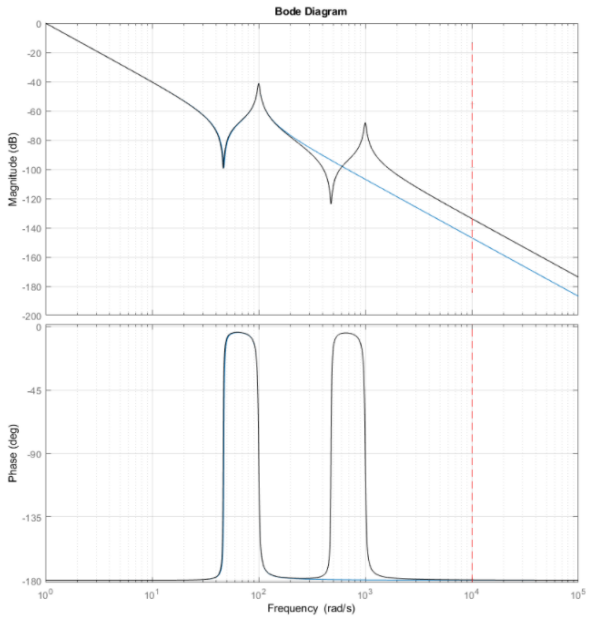

Figure 4.11: A shift in the gain occurs in multi-mode systems. The figure shows a difference in controller gain of a controller with bandwidth frequency of $f_{bw} = 10^4$ [rad/s] between the single-mode system indicated in blue and the total system indicated in black. This effect has to be compensated for.

The figure shows a positive shift of the gain in the high-frequency range due to the second flexible mode. The larger the value of α, the greater the increase or decrease in the gain. The gain increases if α is positive and decreases if α is negative. This cumulative effect is not embedded in the information a stability response surface of a single-mode system provides. This can be explained using Figure 4.11. Assume the controller bandwidth $f_c = 10^4$ rad/s, then the controller gain is determined by the gain of the plant at this frequency, the black mass-line. However, the controller gain for the first mode embedded in the stability response surface

is determined by the gain of the blue mass-line. There is a difference between the controller gain used in obtaining the stability response surface and the true controller gain of the complete system. To create a stability response surface for a multi-mode system, the following extra parameter, besides α and C, is introduced:

$$\Delta G = |G_t(s)|_{2\pi f_c} - |G_i(s)|_{2\pi f_c}, \tag{4.16}$$

where $|G_t(s)|_{2\pi f_c}$ is the gain of the total plant evaluated at the controller bandwidth frequency f_c. $|G_i(s)|_{2\pi f_c}$ is the gain of the reduced system of the mode of interest. The robustness of a multi-mode system with well-spaced modes is a function of three parameters; α, C, and ΔG. A single-mode system with any α and C, but with a constant $\Delta G = 0$, results in a certain modulus margin. The modulus margin is the same as the single-mode stability surface because $\Delta G = 0$. To create a multi-mode stability surface, ΔG is increased or decreased until the modulus margin for that system is 6 dB, the robustness criteria. The ΔG for which the single-mode system results in a modulus margin of 6 dB is then plotted along the third axis. For positive α, this results in two surfaces shown in Figure 4.12 and Figure 4.13.

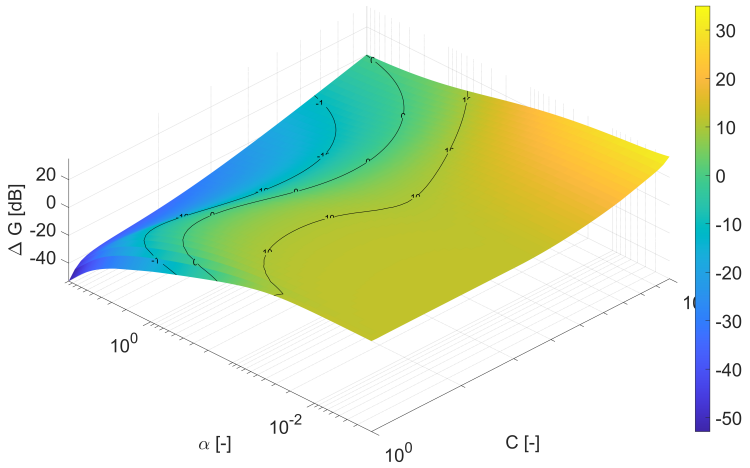

Figure 4.12: Stability response surface of a multi-mode system of the modulus margin for positive values of α and $C > 1$.

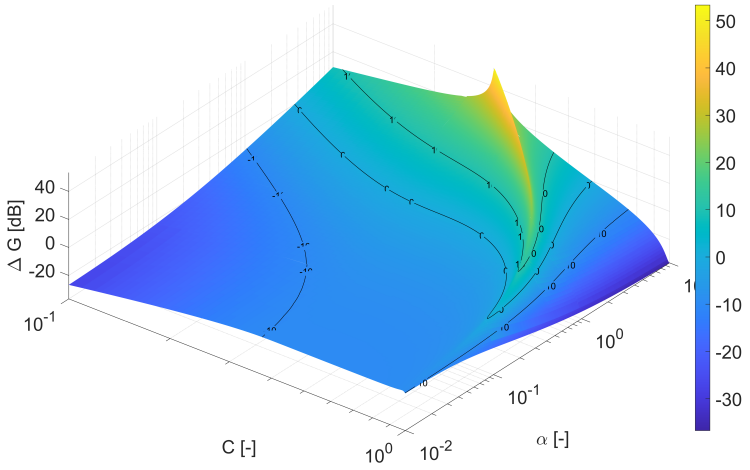

Figure 4.13: Stability response surface of a multi-mode system of the modulus margin for positive values of α and $C < 1$.

The way to interpret these surfaces is as follows. The three parameters of a single-mode m are computed, thus the relative bandwidth C_m, the modal parameter α_m, and the difference of the gain with the complete

system ΔG_m in dB. Then if the point $(C_m, \alpha_m, \Delta G_m)$ lies above the surface in Figure 4.12 or under the surface in Figure 4.13, then that mode is violating the robustness criterion of the complete system.
Figure 4.14 shows two surfaces for negative α and $C < 1$.

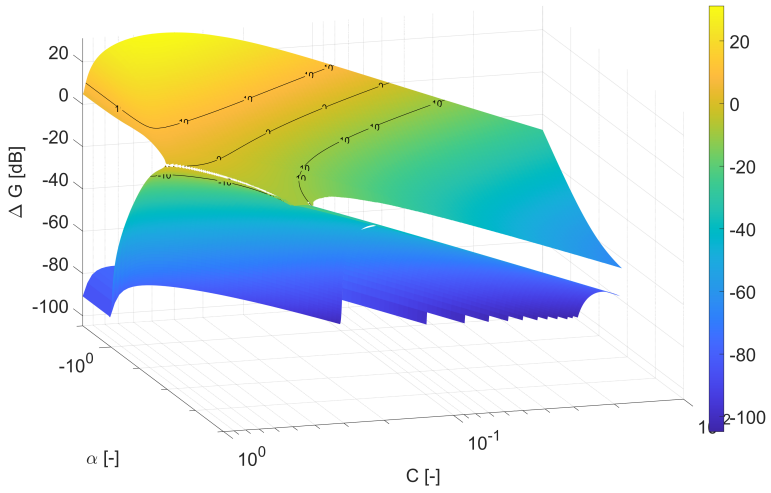

Figure 4.14: Stability response surface of a multi-mode system of the modulus margin for positive values of α and $C > 1$.

If the point $(C_m, \alpha_m$ lies inside the domain of the surfaces in Figure 4.14, then the point $(C_m, \alpha_m, \Delta G_m)$ must be either above the top surface or under the bottom surface for that mode not to violate the robustness of the complete system.

4.4. NURBS interpolation of relative stability response surface

The robustness response surfaces plotted in the previous section are surface plots based on sets of three-dimensional data points obtained via simulations. No information is available in between these data points. From an optimization point of view, it is beneficial to use a mathematical model that can describe the surface continuously compared to the set with finite data points. A continuous model makes evaluating any point in the domain straightforward and possibly provides analytical information on the derivative of the surface. Analytical derivatives allow gradient-based optimization algorithms. The surfaces obtained in Section 4.4 are smooth but with a wide variation in the gradient. This variation in the gradient makes it difficult to model these surfaces with interpolation techniques and require careful attention. This section describes the theory and process in obtaining the mathematical models of the robustness surfaces.

Different techniques exist to model surfaces using a set of finite data points. In this thesis, nonrational B-spline surfaces are used. A B-spline surface is well suited to create accurate representations of the robustness surfaces obtained in Section 4.4 for a few reasons. The first reason is that B-spline surfaces are capable of representing free-form surfaces that are relatively complex precisely. The second reason is that the theory has an easy-to-understand geometric interpretation. It does not require much effort to learn the theory regarding B-spline surfaces and to apply it. To create a mathematical model of the surfaces using B-spline surfaces, an open-source Python library is used. This Python library, developed by the Department of Mechanical Engineering of Iowa State University [1], is a great tool to create and evaluate B-spline surfaces. Most of the theory that follows is found in The NURBS Book by Les A. Piegl [18], and sometimes the reader is referred to papers for additional details.

A nonrational B-spline surface uses piecewise polynomial functions. Before stating the definition of these so-called B-spline basis functions, let $U = \{u_0, \cdots, u_m\}$ be a nondecreasing sequence of real numbers. For example $u_i \leq u_{i+1}$, $i = 0, \cdots, m-1$. The u_i are called knots, and U is the knot vector. Then the B-spline basis

function is defined as:

$$
\begin{aligned}
N_{i,0}(u) &= \begin{cases} 1 & \text{if } u_i \le u < u_{i+1} \\ 0 & \text{otherwise} \end{cases}, \\
N_{i,p}(u) &= \frac{u-u_i}{u_{i+p}-u_i} N_{i,p-1}(u) + \frac{u_{i+p+1}-u}{u_{i+p+1}-u_{i+1}} N_{i+1,p-1}(u),
\end{aligned}
\tag{4.17}
$$

where $N_{i,p}(u)$ is the ith B-spline basis function of degree p. Eq. (4.17) shows that evaluating the B-spline of degree p requires a recursion of evaluations of lower-order functions starting at $p = 0$ to $p = p-1$. In this thesis, cubic curves ($p = 3$) are used to guarantee C^2 continuity. The first and second derivatives of the surface model are continuous, and this makes the model suited for gradient-based optimization algorithms using analytical derivatives.

A nonrational B-spline surface uses the B-spline basis functions in two directions, u and v. A surface of degree p in the u direction and degree q in the v direction is defined as:

$$
\mathbf{S}(u,v) = \sum_{i=0}^{n} \sum_{j=0}^{m} N_{i,p}(u) N_{j,q}(v) \mathbf{P}_{i,j} \qquad 0 \le u, v \le 1, \tag{4.18}
$$

where $N_{i,p}(u)$ and $N_{j,q}(v)$ are the nonrational B-spline basis functions as defined in Eq. (4.17). $\mathbf{P}_{i,j} \in \mathbb{R}^3$ are so-called control points. The set of all control points forms a bidirectional control net and determines the shape of the surface globally. The B-spline surface $\mathbf{S}(u,v)$ is a smooth surface that resembles the global shape determined by the control net. There are a few things to note here. First, the control points do not coincide with the interpolated surface $\mathbf{S}(u,v)$. Second, the control points are different from the data points that define the surface that must be interpolated. The surface model $\mathbf{S}(u,v)$ is a parametric function. The coordinates u and v correspond to an unique point on the surface and are normalized to $[0,1]$. To evaluate the B-spline basis functions at the boundaries of the normalized domain, the knot vectors U and V have the following form:

$$
U = \left\{ \underbrace{0, \cdots, 0}_{p+1}, u_{p+1}, \cdots, u_{r-p-1}, \underbrace{1, \cdots, 1}_{p+1} \right\}, \tag{4.19}
$$

$$
V = \left\{ \underbrace{0, \cdots, 0}_{q+1}, v_{q+1}, \cdots, v_{s-q-1}, \underbrace{1, \cdots, 1}_{q+1} \right\}. \tag{4.20}
$$

Figure 4.15 shows an example of a control net with twenty control points. Straight lines connecting the control points reveal the global shape of the surface. Figure 4.16 shows an example of a nonrational B-spline surface based on the control net in Figure 4.15.

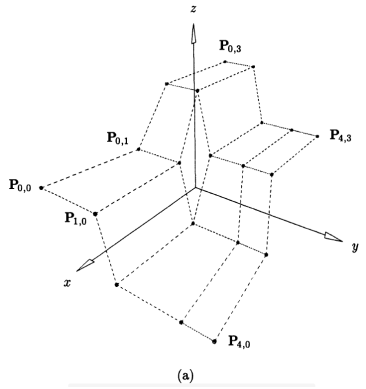

Figure 4.15: A control net with twenty control points. The control points are connected via straight lines, revealing the global shape of the surface model.

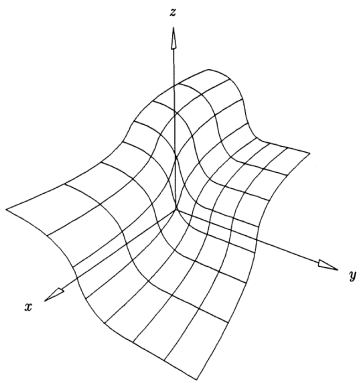

Figure 4.16: The interpolated surface model based on the control net depicted in Figure 4.15. The control points do not coincide with the surface.

To construct a surface model $\mathbf{S}(u,v)$ using Eq. (4.18) that interpolates a surface described by points data requires determining a control net $\{\mathbf{P}_{i,j}\}$, knot vectors U and V, and selection of the B-spline polynomial order p. As mentioned before, cubic curves ($p=3$) are used. The order $p=3$ ensures that the first and second derivatives of the surface model are continuous. It facilitates the use of analytical derivatives of the surface in gradient-based optimization algorithms up to the second derivative.

Many methods to determine knot vectors and a control net to interpolate a surface to point data exist in the literature. The theory of the steps used in this thesis is found in The NURBS Book by Les A. Piegl [18]. Let us assume a set of $(n+1)\times(m+1)$ data points $\{\mathbf{Q}_{k,l}\}$, $k=0,\cdots,n$ and $l=0,\cdots,m$ that describes a surface. To construct a B-spline surface of degree (p,q) that interpolates these points, the following must hold:

$$\mathbf{Q}_{k,l}=\mathbf{S}(\bar{u}_k,\bar{v}_l)=\sum_{i=0}^{n}\sum_{j=0}^{m}N_{i,p}(\bar{u}_k)\,N_{j,q}(\bar{v}_l)\,\mathbf{P}_{i,j}, \tag{4.21}$$

where $\bar{u}_k$ and $\bar{v}_l$ are the parametric coordinates on the B-spline surface that correspond to the data point $\mathbf{Q}_{k,l}$. The first step is to determine these parametric coordinates. Multiple methods exist of choosing $\bar{u}_k$ and $\bar{v}_l$. The most widely used method is the method of chord length because it is generally adequate [18]. In general, it gives a good uniform parameterization. However, in this thesis, a newer method is used. This method proposed by Lee [10] gives better results than the chord length method when the data takes sharp turns [18]. This is the case with the robustness response surfaces, especially at the transition from where the mass-line determines the robustness to where the resonance determines the robustness. The method is also known as the centripetal method and is defined as follows:

$$\begin{cases} \bar{u}_0^l=0, \quad \bar{v}_k^0=0, \quad \bar{u}_n^l=1, \quad \bar{v}_k^m=1, & \forall\, k,l \\ \bar{u}_k^l=\bar{u}_{k-1}^l+\dfrac{\sqrt{|\mathbf{Q}_{k,l}-\mathbf{Q}_{k-1,l}|}}{\sum_{s=1}^{m}\sqrt{|\mathbf{Q}_{s,l}-\mathbf{Q}_{s-1,l}|}}, & k=1,\cdots,m, \quad l=0,\cdots,n \\ \bar{v}_k^l=\bar{v}_k^{l-1}+\dfrac{\sqrt{|\mathbf{Q}_{k,l}-\mathbf{Q}_{k,l-1}|}}{\sum_{t=1}^{n}\sqrt{|\mathbf{Q}_{s,l}-\mathbf{Q}_{s,l-1}|}}. & k=0,\cdots,m, \quad l=1,\cdots,n \end{cases} \tag{4.22}$$

The next step is to construct the knot vectors U and V by choosing proper knots u_i and v_j. The most straightforward method is to choose the knots such that they are equally spaced. However, this method is not recommended [18]. Instead, a technique used by many, for example in [27], is applied. In this technique, the knots are determined by averaging the parameterization of the data points obtained via equation Eq. (4.22). First, a reduced set of $\bar{u}_k$ and $\bar{v}_l$ is obtained by averaging across all $\bar{u}_k^l$, $l=0,\cdots,m$, $\bar{v}_k^l$, $m=0,\cdots,n$ via:

$$\bar{u}_k=\frac{1}{m+1}\sum_{l=0}^{m}\bar{u}_k^l, \qquad k=0,\cdots,n \tag{4.23}$$

$$\bar{v}_l=\frac{1}{n+1}\sum_{k=0}^{n}\bar{v}_k^l. \qquad l=0,\cdots,m \tag{4.24}$$

Then to obtain the knots and the knot vectors, another averaging is applied. Each knot is the average of p neighboring parameters. With this method the knots reflect the distribution of $\bar{u}_k$ and $\bar{v}_l$. The knots that define the knot vector becomes:

$$\begin{aligned} u_0=\cdots=u_p=0 \qquad & u_{m-p}=\cdots=u_m=1 \\ u_{j+p}=\frac{1}{p}\textstyle\sum_{i=j}^{j+p-1}\bar{u}_i \qquad & j=1,\cdots,n-p \end{aligned} \tag{4.25}$$

The main result of this method is that equal numbers of data points are located inside the support domain of all of the B-splines, $N_{i,p}(\bar{u}_k)=0$ if $|i-k|\geq p$. If this is the case, it is guaranteed that the system of linear equations in Eq. (4.21) is non-singular or not ill-conditioned. Hence, the control net $\{\mathbf{P}_{i,j}\}$ can be calculated by Gaussian elimination.

To obtain the NURBS models, the robustness response surfaces described in Section 4.3 are first divided in patches. The reason for this is that the complete surface shows large variations in gradients. To model the

surface regions with large gradients accurately requires a dense grid of control points. Evaluating a point in a region that is rather smooth would be unnecessarily computationally costly. Therefore, to reduce computational time, the surface is divided into rather smooth patches and patches containing large variations in gradients. The number of control points is equal to the number of data points that define the surface. Thus the number of data points needs to be reduced to obtain a NURB model that is computationally attractive. This was done with the aid of Python as follows. The first and third row of the data points is selected initially and linear lines between the points of the first row and third row are computed. The distances of the data points of the second row to the linear lines are then computed and if one of the distances is greater than a certain threshold, the rows are kept in the surface model. The second row is removed if all distances are smaller than the threshold which reduces the set of data points. This method is repeated for all rows and the same is done for the columns. The result is a reduced data set of the surface patches without compromising accuracy. Figure 4.17 shows two examples of this process, one patch with a small variation in the gradient and one patch with a large variation in the gradient.

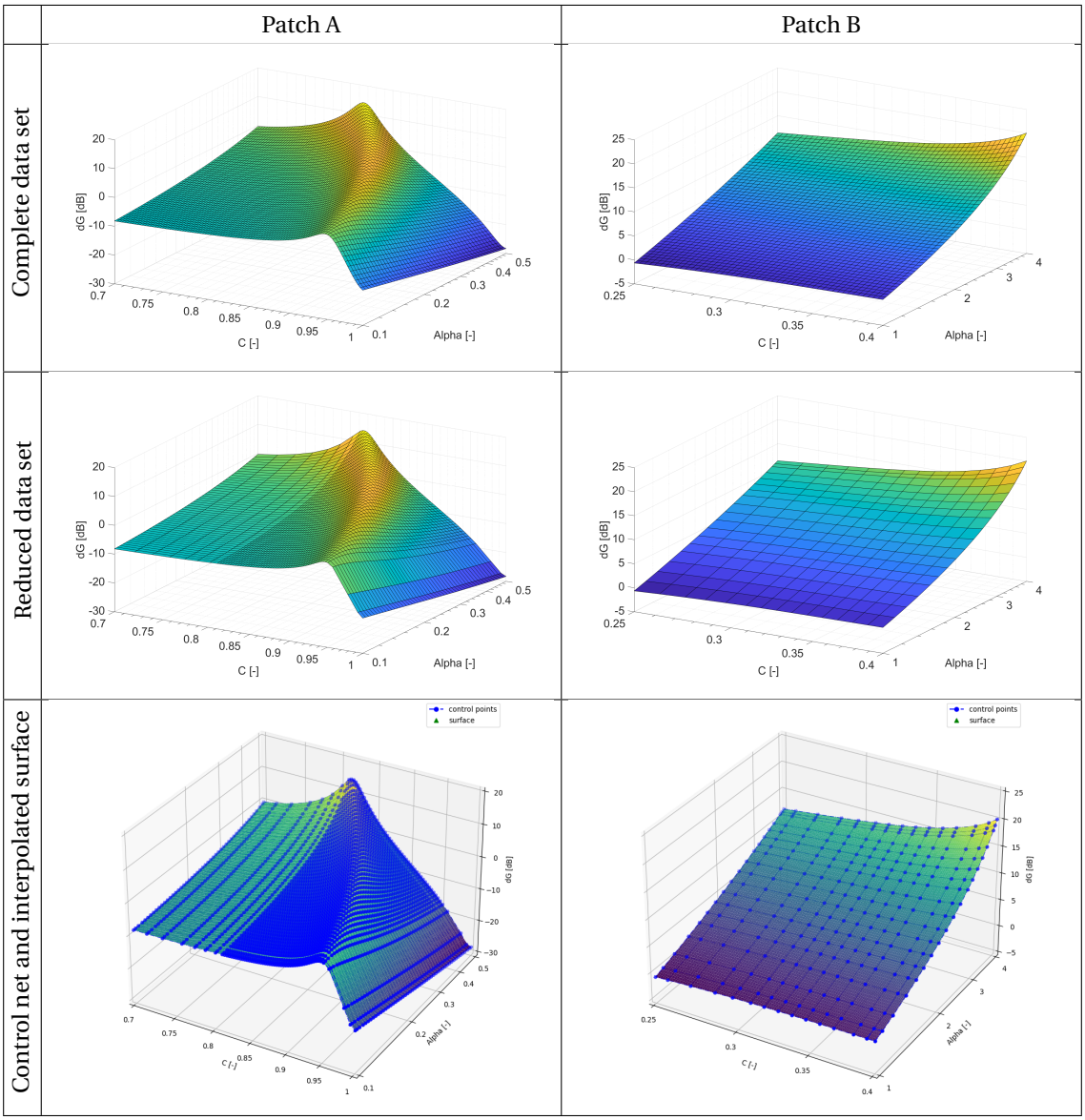

Figure 4.17: The complete data set, reduced data set, and the control net with the interpolated surface for two patches.

5

Optimization

The application of the robustness constraint derived in Chapter 4 in an optimization problem is studied in this chapter. This chapter starts with the optimization problem statement, plus details are given on modeling aspects and the solution procedure. The remainder of this chapter presents examples of optimizations and their results for different parameterizations, such as actuator placement, actuator and sensor placement, and shape optimization.

5.1. Optimization problem statement and its solution

In formulating an optimization problem with the robustness response surface as an constraint, one is free to choose the objective function and to add other constraints. The bandwidth frequency usually determines the performance of a controlled motion system. Increasing the bandwidth decreases the system's rise time, which means a faster operation or better tracking in a tracking task. Increasing the bandwidth also improves the disturbance rejection of the controlled system. The bandwidth of systems that must carry out repetitive tasks many times often must be as high as possible as it increases throughput and can reduce cost. So the objective of the optimization problem in this thesis is to maximize the bandwidth frequency of the controller. The objective function is defined as the inverse of the bandwidth to comply with the negative null form. As for the constraints, no extra constraints are imposed other than the robustness response surface constraint and the constraint on the structural modal parameter α. The problem stated in the negative null form:

$$
\begin{aligned}
\underset{\mathbf{x}}{\text{minimize}} \quad & f(\mathbf{x}) = \omega_{\text{bw}}^{-p} \\
\text{subject to} \quad & \pm S_{i,m} \mp \Delta G_m \leq 0 && \forall m \in \{1,2,\cdots,n\} \\
& -\left(\alpha_j + 1\right) \leq 0 && \forall j \in \{1,2,\cdots,n-1\} \\
& C_m = \frac{\omega_{bw}}{\omega_m} \\
& \alpha_m = \begin{cases} \left(\dfrac{\operatorname{Im}\left(p_m\right)}{\operatorname{Im}\left(z_m\right)}\right)^2 - 1 & \text{if } \alpha_m > \zeta^2 - 1 \quad \text{(complex zero pair)} \\ -\left(\dfrac{\omega_m}{\operatorname{Re}\left(z_m\right)}\right)^2 - 1 - \dfrac{2\zeta\omega_m}{\operatorname{Re}\left(z_m\right)} & \text{if } \alpha_m < \zeta^2 - 1 \quad \text{(real zero pair)} \\ \zeta^2 - 1 & \text{if } \alpha_m = \zeta^2 - 1 \quad \text{(one real zero)} \end{cases}, \\
& \Delta G_m = \left| \frac{G_t(\omega_{bw})}{K_m G_m(\omega_{bw})} \right|_{\text{dB}} \\
& K_m = \frac{|G_t(\omega_{Pm})|}{|G_m(\omega_{Pm})|} \\
& \mathbf{K}\boldsymbol{\phi}_m = \omega_m^2 \mathbf{M}\boldsymbol{\phi}_m \\
& \mathbf{0} < \underline{\mathbf{x}} \leq \mathbf{x} \leq \overline{\mathbf{x}}
\end{aligned}
\tag{5.1}
$$

where ω_{bw} is the bandwidth frequency and p is a penalty on the objective function. $S_{i,m}$ is the NURBS surface patch that is active for mode m, evaluated at the the relative bandwidth C_m and modal parameter α_m

of mode m. The active patch is identified by looping over all patches and selecting the one for which the point (C_m, α_m) lies in its domain. The domains of patches for positive α do not overlap. For negative α some patches share the same or parts of their domain. If two patches are active, the constraint is computed for both and the most critial value is set as contraint for that particular mode. The robustness constraint value is set to -100 if C_m lies outside the domain of C of the patches. The difference in frequency between the bandwidth and the eigenfrequency is such that the mode will not endanger the robustness of the system in this case. There are two possibilities if C_m lies inside the domain of the patches but α_m is not. If the value of α_m is between zero and the minimum value of α at C_m, then α_m is set to this minimum value α. The robustness constraint value is set to -100 if α_m is greater than the maximum value of α. However, α's greater than the maximum value of the surface is practically impossible and has never occurred in any optimization case. The number of robustness constraints is equal to the number of modes n considered in the optimization. However, the number of α constraints is equal to $n-1$. The primary purpose of this constraint is to prevent a permanent phase shift after the resonance of the mode so that the robustness constraint of the succeeding mode is valid. There is no need to impose the α constraint on the last mode because the succeeding mode is not considered in the optimization. Additionally, non-minimum phase behavior is undesired in general. In the problem statement, ΔG_m is the difference in gain, in decibel, between the single-mode system G_m and the total system G_t at the bandwidth frequency. K_m is the mapping factor that maps the single-mode system onto the total system at the frequency of the pole ω_{P_m}.

The optimization problem is solved using the Method of Moving Asymptotes (MMA), a gradient-based method proposed by K. Svanberg [22]. A convex approximation of the optimization problem is constructed and solved with this technique and is one of the most popular choices of methods in structural topology optimization. Initially, the optimizations did not run smoothly. The optimizer did not converge to a local optimum and kept oscillating between designs. The reason for these oscillations was the robustness constraint of the mode for which the modal parameters α switched sign in each iteration. The optimizer especially had difficulties for $C_m \approx 1$, so when the bandwidth frequency is close to the eigenfrequency of mode m. In this situation, the robustness is very sensitive to design changes.
MMA can deal with oscillations with the correct MMA settings for the specific problem. The recommendations concerning design variable limits and scaling proposed by K. Svanberg [23] are applied in the process to find the correct MMA settings. The objective function is scaled before the first iteration to $f_0(\mathbf{x}) = 100$. The bounds of the design variables are $0.1 \leq \mathbf{x} \leq 100$. The bounds of the physical variables are mapped onto the design variable bounds via a linear mapping, so there is a linear relationship between the physical and design variables. The bandwidth variable is not physically bounded, but in the optimization the bandwidth variable is bounded with respect to the eigenfrequency of the lowest mode. The bound is set to $0.01\omega_1 \leq \omega_{\text{bw}} \leq 10\omega_1$, where ω_1 is the eigenfrequency of the lowest mode considered. Smooth convergence to (local) optima is evetually achieved by selecting the right move limit setting of the MMA. Table 5.1 states important MMA settings regarding convergence and operation.

convergence options		
tolX		$10^{-4} - 30^{-4}$
maxIt		200
operational options		
MMA subproblem approximation		first order
x_min	ω_{bw}	0.1
	p_a	1.0
	p_s	1.0
x_max	ω_{bw}	100
	p_a	10
	p_s	10
move limit		0.02 - 0.05
p		0.2

Table 5.1: MMA convergence and operational options

5.2. Actuator placement

This section gives examples of designs obtained by solving the optimization problem statement presented in Section 5.1. The actuator position p_a along the Bernouilli-Euler beam and the controller bandwidth ω_{bw} are the only design variables considered in this section. The position of the sensor and the beam's shape are thus fixed during the optimization. Figure 5.1 presents a schematic of the problem. The optimized designs are compared to designs that were determined by hand using engineering design principles.

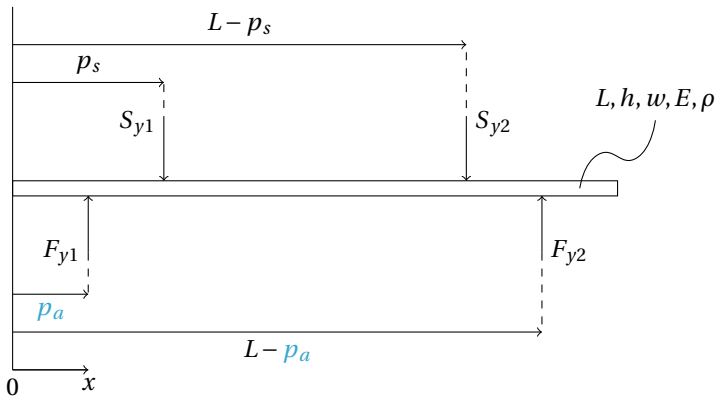

Figure 5.1: Sketch of the actuator placement problem. The plant, modeled as an Euler-Bernoulli beam, and the sensor arrangement are constant throughout the optimization. The actuator position p_a is the design variable. Note that only one design variable is needed to define the positions of both actuators due to the choice that the arrangement of both the actuators and sensors is symmetric.

The beam parameters used in this section are: length $L = 1$ [m], height $h = 0.2$ [m], width $w = 0.1$ [m], Young's modulus $E = 20 \times 10^{10}$ [N/m^2], and density $\rho = 1000$ [kg/m^3]. Optimization runs for different sensor pair locations p_s are done, where $p_s \in$ [0.0, 0.1, 0.224, 0.3, 0.4]. For each sensor pair, multiple optimization runs, each with different initial designs regarding actuator location, were performed. The initial controller bandwidth is set relatively low at one percent of the eigenfrequency of the first flexible mode, $\omega_{bw,0} = 0.01 \times \omega_1$. Starting with this bandwidth frequency ensures that the robustness constraints are satisfied at the beginning of the optimization. However, it does not assure that the constraints regarding the α's are satisfied since they are independent of the controller.
The methodology to obtain designs using engineering design principles is as follows. Multiple unique actuator locations are selected for each sensor considered. These locations are the nodes of the flexible modes and the sensor location under consideration (collocated system). Then, with the aid of Python, a controller is designed for each design by selecting the highest bandwidth frequency possible, thus without violating the robustness criteria. The design with the highest controller bandwidth is selected and compared with the design obtained via optimization.

Table 5.2 presents the designs obtained using the explained methodology and optimization. The second last column gives the ratio of the bandwidth of the optimized system, bw_{opt}, to the bandwidth of the system obtained using engineering principles, bw_{ep}. This ratio is a performance measure of the optimized system relative to the system obtained via engineering principles. The second last column shows that the optimized system does not always perform better. What now follows is a discussion on the results.

	Actuator placement							
	Design using engineering principles		Design using optimization					
			initial design		final design			
p_s [m]	p_a [m]	bw_{ep} [rad/s]	p_a [m]	bw_0 [rad/s]	p_a [m]	bw_{opt} [rad/s]	bw_{opt}/bw_{ep} [-]	case
0	0.224	8.384×10^3	0.0	182.68	0.1678	7.9943×10^3	0.954	A
			0.1		0.1678	7.9945×10^3	0.954	A
			0.2		0.2259	8.4152×10^3	1.004	B
			0.3		0.2259	8.4153×10^3	1.004	B
			0.4		0.2259	8.4152×10^3	1.004	B
			0.5		0.2259	8.4153×10^3	1.004	B
0.1	0.224	4.3878×10^4	0.0	182.68	0.1390	8.8861×10^4	2.025	C
			0.1		0.1391	8.8865×10^4	2.025	C
			0.2		0.1391	8.8865×10^4	2.025	C
			0.3		0.1391	8.8865×10^4	2.025	C
			0.4		0.1391	8.8865×10^4	2.025	C
			0.5		-	-	-	
0.224	0.094	4.5230×10^4	0.0	182.68	0.1363	4.5005×10^4	0.955	D
			0.1		0.1363	4.5004×10^4	0.955	D
			0.2		0.1363	4.5005×10^4	0.955	D
			0.3		0.3164	5.2314×10^4	1.157	E
			0.4		0.3164	5.2314×10^4	1.157	E
			0.5		0.3164	5.2317×10^4	1.157	E
0.3	0.355	6.5856×10^4	0.0	182.68	0.2486	4.8178×10^4	0.732	F
			0.1		0.2486	4.8178×10^4	0.732	F
			0.2		0.2486	4.8178×10^4	0.732	F
			0.3		0.2486	4.8178×10^4	0.732	F
			0.4		0.2486	4.8178×10^4	0.732	F
			0.5		0.2486	4.8178×10^4	0.732	F
			0.335	6.5856×10^4	0.3570	9.8650×10^4	1.498	G

Table 5.2: Final designs of the actuator placement problem using optimization for different initial conditions and designs using engineering principles.

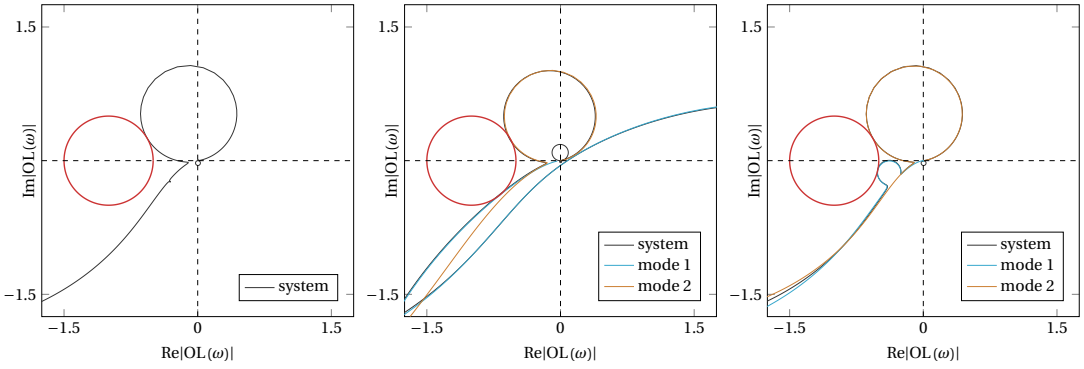

Figure 5.2: The final designs of the actuator placement problem for sensor location $p_s = 0$ [m]. (left) Design using engineering principles with a bandwidth of $bw_{ep} \approx 1334$ [Hz]. (middle) Design using optimization with a bandwidth of $bw_{opt} \approx 1272$ [Hz]. (right) Design using optimization with a bandwidth of $bw_{opt} \approx 1339$ [Hz].

The system designs with the sensor location at $p_s = 0$ have the worst performance because all modes have high observability. Therefore the actuator was placed at the node of the first flexible mode in the design using

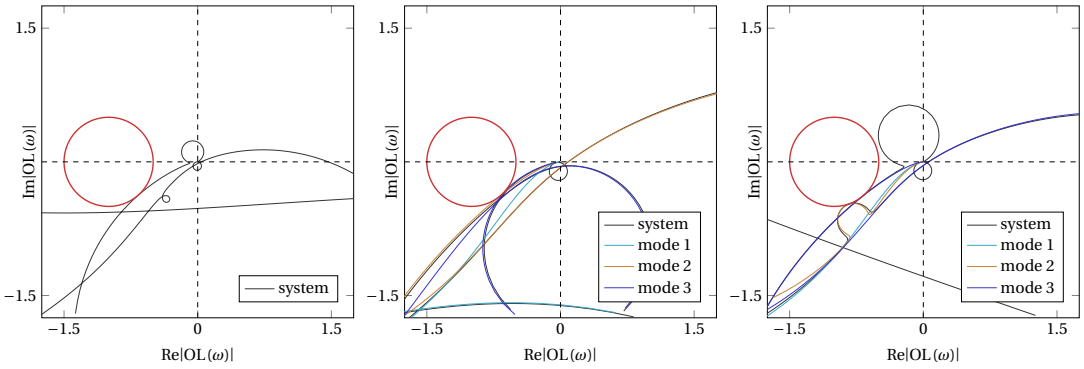

Figure 5.3: The final designs of the actuator placement problem for sensor location $p_s = 0$ [m]. (left) Design using engineering principles with a bandwidth of $bw_{ep} \approx 10481$ [Hz]. (middle) Design using optimization with a bandwidth of $bw_{opt} \approx 6778$ [Hz]. (right) Design using optimization with a bandwidth of $bw_{opt} \approx 15701$ [Hz].

engineering principles (EP). The result is that the second mode is the limiting factor and restricts the controller to a bandwidth of $bw_{ep} \approx 1334$ [Hz]. For the designs using optimization, the optimizer converged to two optima. One, design A, performs slightly less relative to the EP design. The second, design B, performs marginally better. Figure 5.2 shows the Nyquist plots of the three designs. The figure shows that two robustness constraints are active for the optimized designs, one for the first flexible mode and one for the second mode. Design B is just a slight improvement of the EP design with a small adjusted actuator position away from the node of the first mode. The high observability of all modes prevents further design improvement. It is safe to say that design B is the global optimum for this simple system and is close to the EP design. Just two modes were considered in the optimization resulting in designs A and B. Adding more flexible modes to the optimization results in designs that perform less or lead to situations in which the optimization does not converge. It is due to the high observability of the modes in combination with the α constraint. The poor choice for the sensor position results in large values for α, and the α constraint is not satisfied if $\alpha < -1$. However, the α constraint is only needed for the highest mode for which the robustness constraint is active and its previous modes. For the higher modes it does not matter. Thus for optimization, it is important to consider a set of modes with no more modes than the highest mode for which the robustness constraint is active in the final design. One strategy is to consider a low number of modes for optimization and add modes one by one until the optimized design ensures that the total system is robust too.

The second interesting set of designs is the one with the sensor location at $p_s = 0.3$. For the optimized designs, the optimizer converged to one optimum starting from five different initial actuator positions. However, the design performs way less than the EP design. Placing the actuator in the node of the second mode results in the highest controller bandwidth for the EP design method, with $bw_{ep} \approx 10481$ [Hz]. The first flexible mode is observable and controllable, but is not the limiting factor in this case. Removing the presence of the second mode in the transfer creates a frequency range between modes one and three suited to place the controller bandwidth. Mode 3 is the limiting factor for the EP design. The optimizer converges to a local optimum where modes 1 and 2 are the limiting factor, with $bw_{ep} \approx 7668$ [Hz]. Now the question arises if it is possible that an initial design results in a system that performs better than the EP design. Selecting the EP design as the initial design for optimization is the only initial design that results in a better feasible design with a $bw_{ep} \approx 15701$ [Hz]. In this design, modes 2 and 3 are the limiting factor. If the initial design slightly deviates from the EP design but is infeasible, the optimizer does not converge or does converge to a system with lower bandwidth. Figure 5.3 shows the Nyquist plots of the three designs.

The case of $p_s = 0.1$ [m] is the last example of the actuator placement problem. It is a good example where the design obtained using optimization performs much better in comparison to the EP design. Placing the actuator in the node of the first mode results in the best EP design, with a bandwidth of $bw_{ep} \approx 6983$ [Hz]. The fourth flexible mode is the limiting mode for this design. The optimizer converged to one optimum for all initial actuator positions except for $p_a = 0.5$ [m]. The α constraint was not satisfied, and the optimizer did not converge to a feasible design for this initial actuator position. The four other runs did converge to one optimum. With three active constraints, for modes one, three, and four, the bandwidth is limited to $bw_{ep} \approx 14143$

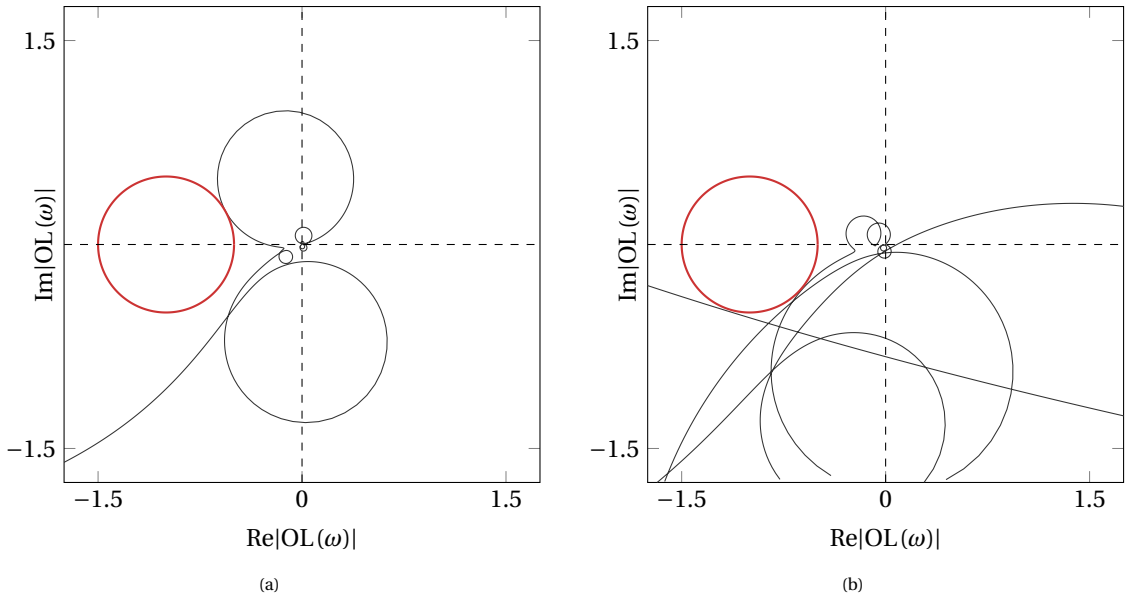

(a) (b)

Figure 5.4: The final designs of the actuator placement problem. (a) Design using engineering design principles with a bandwidth of $\text{bw}_{\text{ep}} \approx 6983$ [Hz]. (b) Design using optimization with a bandwidth of $\text{bw}_{\text{opt}} \approx 14143$ [Hz].

[Hz]. The optimized design performs significantly better compared to the EP design with an increased bandwidth of factor two. Figure 5.4 shows the Nyquist plots of the EP design and optimized design. Figure 5.5 shows the optimizer's performance for the case with initial actuator location $p_a = 0.4$ [m]. The optimizer's performance of case C can be found in Apendix A. It visually presents a well-performing optimization run, where, in the end, three robustness constraints are active.

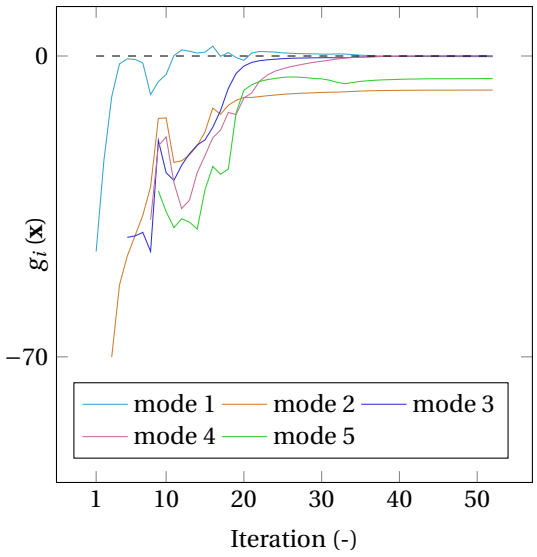

(a)

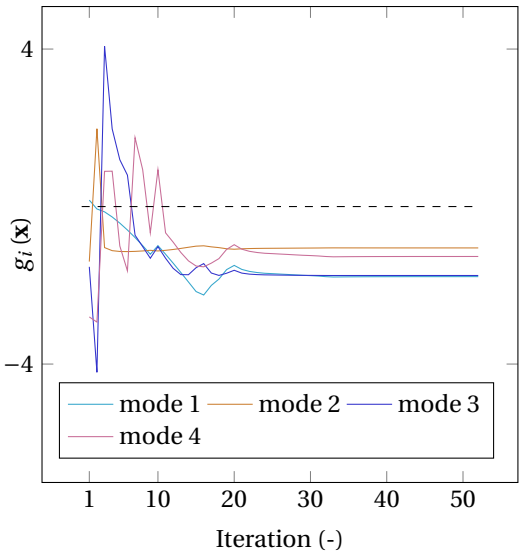

(b)

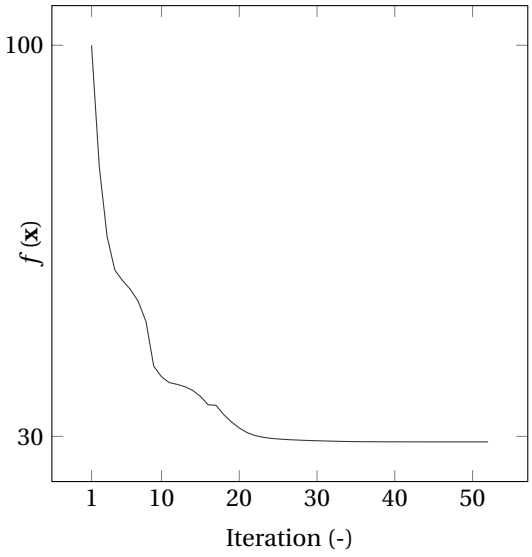

(c)

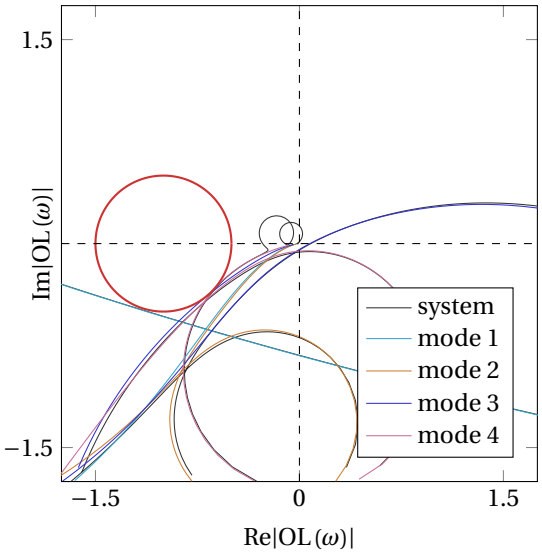

(d)

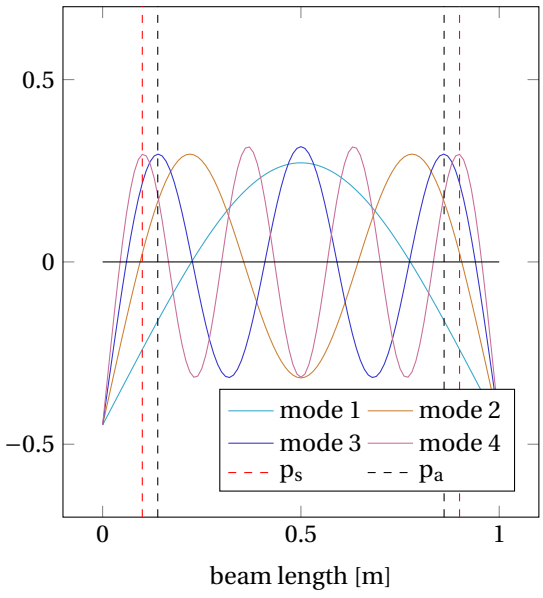

(e)

CASE C: moet in subsection 'actuator placement'

Figure 5.5

5.3. Actuator and sensor placement

The actuator position and the controller bandwidth were the design variables of the previous section. In this section, the sensor location is added to the design variables. The shape of the beam is again constant throughout the optimization. Figure 5.6 presents a schematic of the actuator and sensor placement problem. The beam parameters are the same as in the previous section. Multiple optimized designs, each with different initial designs, are compared to a system obtained using engineering design principles.

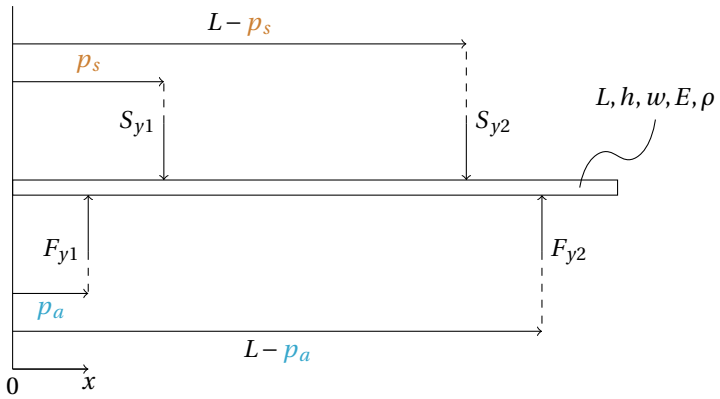

Figure 5.6: Sketch of the actuator and sensor placement problem. The plant, modeled as an Euler-Bernoulli beam, is constant throughout the optimization. The actuator position p_a and the sensor position p_s are the design variables. Note that only one design variable is needed to define the positions of both actuators and one design variable is needed to define the positions of both sensors due to the choice that the arrangement of both the actuators and sensors is symmetric.

For the design using engineering principles, the sensor pair location is at the nodes of the first flexible mode $p_s = [0.223 \quad 0.776]$, and the actuator pair location is at the nodes of the second mode $p_a = [0.0945 \quad 0.9055]$. The result is that the first mode is not observable, and the second mode is not controllable, and therefore they will not be the limiting factor in controller design. It turns out that the fourth flexible mode is the limiting factor for this setup and limits the bandwidth to bw = 45148 [rad/s] or bw = 7186 [Hz]. Figure 5.8 shows the Nyquist plot of the open-loop transfer. The figure displays that the fourth mode is the one that limits the maximum attainable bandwidth.
Five simulation runs were done for the design using optimization, each simulation with a unique initial design. Table 5.3 presents these five initial designs and the resulting final designs. The optimizer converged four times to optimum A with a controller bandwidth of bw ≈ 8871 [Hz]. Only one time did the optimizer converge to optimum B with a controller bandwidth of bw ≈ 7891 [Hz]. The open-loop Nyquist plot of the EP design

Actuator and sensor placement							
Design using optimization							
initial design			final design				
p_a [m]	p_s [m]	bw_0 [rad/s]	p_a [m]	p_s [m]	bw_{opt} [rad/s]	bw_{opt}/bw_{ep} [-]	case
0.00	0.00		0.3122	0.2376	5.5460×10^4	1.228	A
0.50	0.50		0.2368	0.3120	5.5743×10^4	1.235	A
0.50	0.00	182.68	0.2369	0.3120	5.5737×10^4	1.235	A
0.25	0.25		0.2020	0.1327	4.9579×10^4	1.098	B
0.40	0.10		0.2370	0.3120	5.5758×10^4	1.235	A
0.14	0.10	8.8865×10^4	0.1735	0.0974	9.8393×10^4	2.192	C

Table 5.3: Initial and final designs of the actuator and sensor placement problem using optimization.

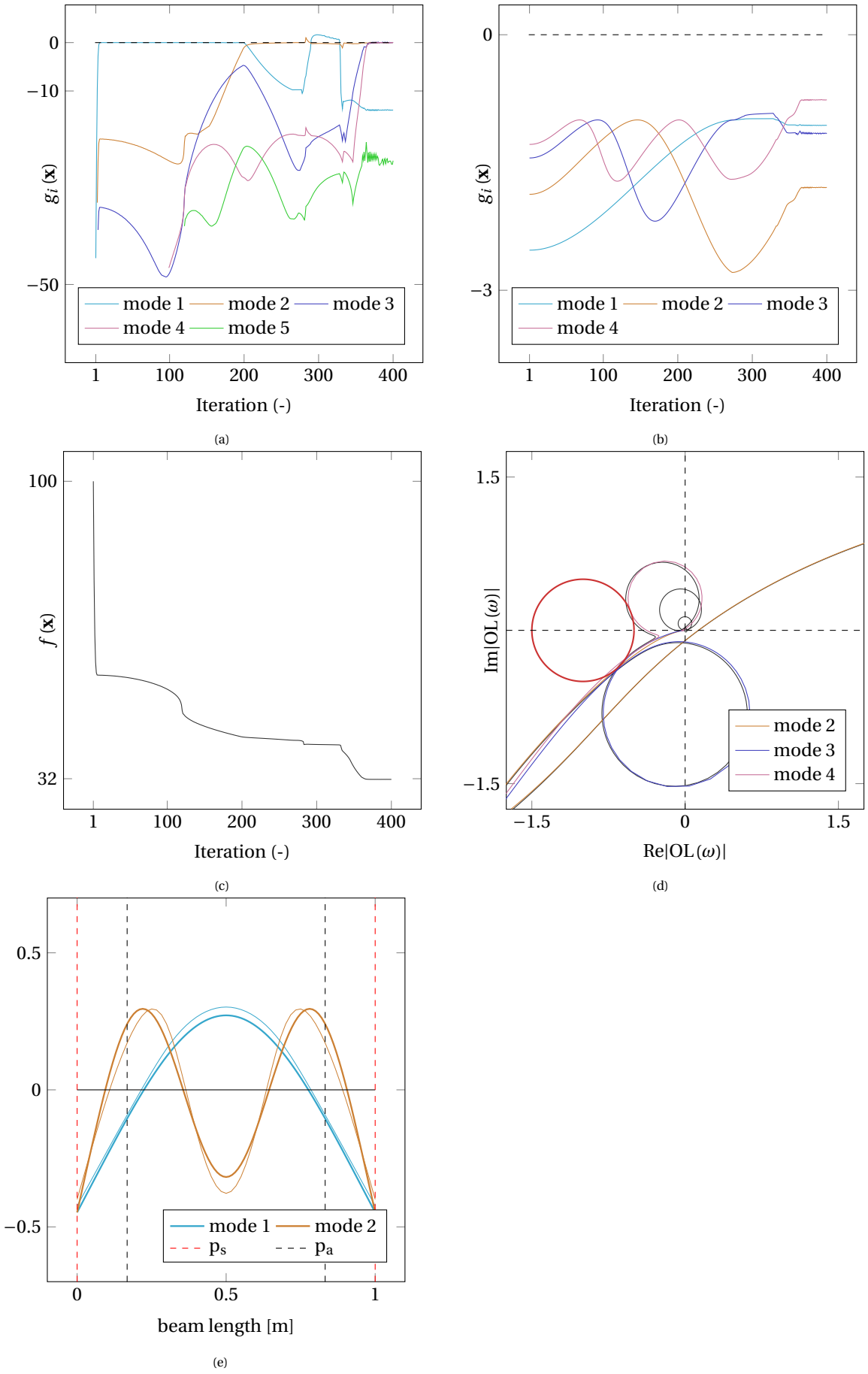

Figure 5.7: Optimization performance of design A of the actuator and sensor placement problem with an initial sensor location of $p_s = 0.1$ [m] and initial actuator location of $p_a = 0.4$ [m].(a) Robustness constraints with modes two, three, and four as active constraints in the final design. (b) α constraints. (c) Objective functions. (d) Nyquist plot of the open-loop.

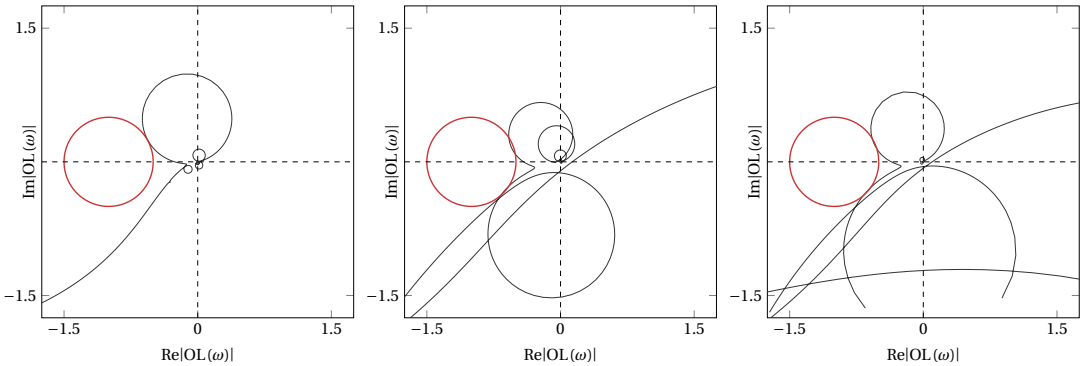

Figure 5.8: The open-loop Nyquist plots the final designs of the actuator and sensor placement problem. (left) Design using engineering principles with a bandwidth of $bw_{ep} \approx 7186$ [Hz]. (middle) Design A using optimization with a bandwidth of $bw_{opt} \approx 8872$ [Hz]. (right) Design B using optimization with a bandwidth of $bw_{opt} \approx 7891$ [Hz].

and the two optimized designs are shown in Figure 5.8. Three robustness constraints are active in design A for modes two, three, and four. For design B, two robustness constraints are active. The limiting modes are three and four. Figure 5.7 shows the optimizer's performance for design A with initial sensor location $p_s = 0.1$ [m] and actuator location $p_a = 0.4$ [m]. Both designs A and B perform better compared to the EP design. The introduction of more design freedom by adding the sensor position as a design variable makes the optimization method more advantageous than the EP method. Comparing the designs of the actuator and sensor placement problem to the designs of the actuator placement problem shows that the optimizer converged to a local optimum. The highest bandwidth obtained in the actuator placement problem was for $p_s = 0.1$ [m] with bw ≈ 14143 [Hz], which is significantly better than the actuator and sensor placement designs. The question arises if an initial design for the actuator and sensor problem may result in a system that performs better than the best design obtained in the actuator placement problem. Selecting the best actuator placement design as the initial design for the actuator and sensor problem does result in a better feasible design with a bandwidth of bw ≈ 15755 [Hz]. The robustness constraints of again three modes are active, but this time it are modes one, four, and five. Design C performs significantly better compared with the EP design, with a ratio of $bw_{opt}/bw_{ep} = 2.192$.

Figure 5.9 shows the open-loop Nyquist plots of design A and the improved design. The figure also shows the Nyquist plots of the single-mode systems of the active modes. Where the approximation of the total system with single-mode systems is very accurate in the previous examples, this is not the case for the situations depicted in the figure. The single-mode system of mode four in design A does not accurately resemble the dynamics of the frequency region around mode four. Though the dynamics are dominated by mode four, the influence of the preceding mode and succeeding mode is large enough to result in an error in the Modulus Margin (MM). The MM of the total system turns out to be 6.35 dB and does not comply with the robustness criteria of 6 dB. The source of this error lies in the accuracy of the single-mode plant model and not the controller. A few factors determine the magnitude of the error. The most significant factor is how well-spaced the modes around the frequency of interest are. The closer the eigenfrequencies of two consecutive modes are, the higher the change is that a single-mode system can not represent the dynamics well. The magnitude and the sign of alpha of a mode and its preceding and succeeding modes influence this error. The error is not cumulative, meaning that the approximation error of one mode has no relation with the approximation of another mode.

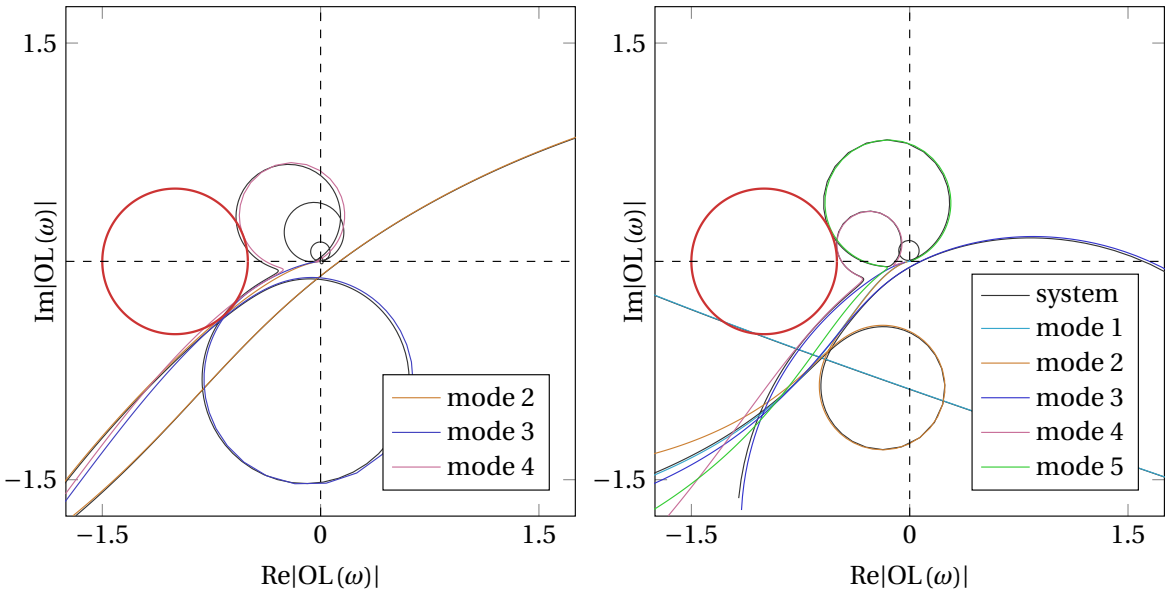

Figure 5.9: The open-loop Nyquist plots of the final designs of the actuator and sensor placement problem. (left) Design A with a bandwidth of 8871 [Hz]. In design A, modes 3 and 4 are active. (right) Improved design with the best performing design of the actuator placement problem as the initial design. In this design modes 1, 4, and 5 are active at a bandwidth of 15755 [Hz].

5.4. Shape optimization

This section presents examples of shape optimizations for fixed actuator and sensor configurations. The design variables are the heights of the Euler-Bernoulli beam elements. A design variable is assigned to two finite elements that have an equal distance to the center of the beam. So the two outer elements share the same design variable and thus have the same height. The beam is discretized with 60 elements for each case, which results in 30 design variables.

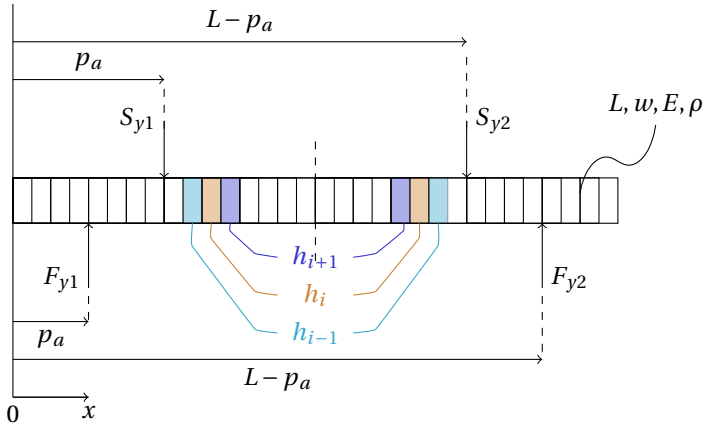

Figure 5.10: Sketch of the beam shape optimization problem. The actuator position p_a and the sensor position p_s are constant throughout the optimization. The plant, modeled as an Euler-Bernoulli beam, is discretized using Hermitian shape functions. One design variable is assigned to the two elements which have an equal distance with respect to the centre of the beam. The resulting designs are thereby symmetric.

The designs obtained using optimization in the actuator placement problem and the actuator/sensor placement problem are selected as initial designs for the shape optimization problem. Design A of the actuator placement problem from Section 5.2 is the starting point for the first case of shape optimization. Figure 5.11 shows both the initial and final design. Figure 5.12 shows the Nyquist plot of the open-loop system and the mode shapes of the initial design and final design. The constraints regarding modes 1 and 2 are active at the

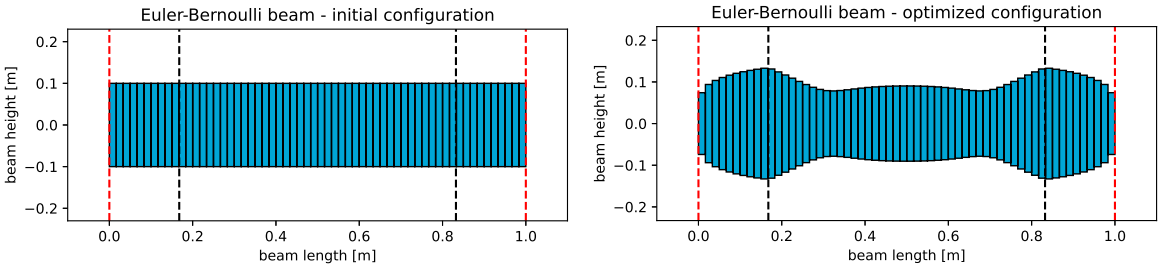

Figure 5.11: The final design of the beam height optimization problem A with fixed actuator and sensor configuration. The sensor pair is indicated by the red dashed lines and the actuator pair by the black dashed lines. (left) Initial configuration. (right) Optimized configuration.

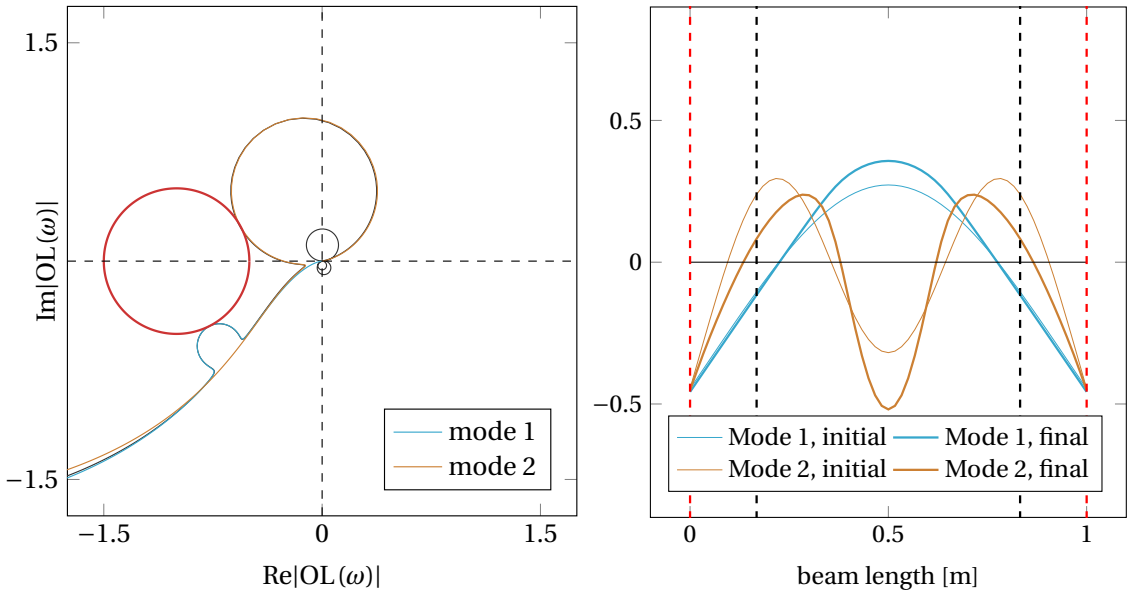

Figure 5.12: The final design of the beam height optimization problem A with fixed actuator and sensor configuration. (left) Nyquist plot of the open-loop system. (right) The mode shapes of the critical modes of the initial design and final design.

start of the optimization. Modes 1 and 2 are still the limiting factor in the final design, however, the bandwidth increased by a factor of 1.086 from $\text{bw}_1 \approx 1272$ [Hz] to $\text{bw}_{\text{opt}} \approx 1381$ [Hz]. The observability and controllability of the first mode and the observability of the second did not change much in the final design. The controllability of the second mode was reduced quite significantly. Figure 5.13 shows the final design and Figure 5.14
Design B of the actuator placement problem from Section 5.2 is the starting point for the first case of shape optimization. Figure 5.13 shows the final design of the beam and Figure 5.14 shows the Nyquist plot of the open-loop system together with the mode shapes of the initial design and final design. Again the shape optimization resulted in an improved design with an increase of bandwidth by a factor of 2.67 from $\text{bw}_1 \approx 1339$ [Hz] to $\text{bw}_{\text{opt}} \approx 3578$ [Hz]. One interesting observation to mention is that both the observability and controllability have increased in the final design. This result opposes the idea of minimizing the controllability and observability or the energy norm in order to obtain improved mechanical parts in perspective of control performance.

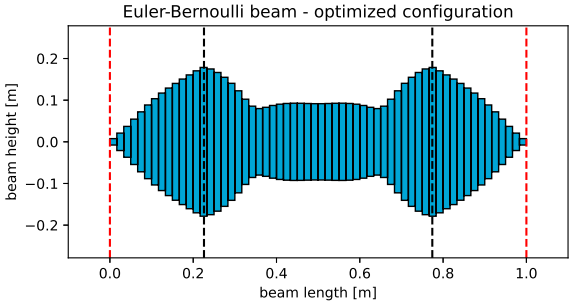

Figure 5.13: The final design of the beam height optimization problem B with fixed actuator and sensor configuration. The sensor pair is indicated by the red dashed lines and the actuator pair by the black dashed lines.

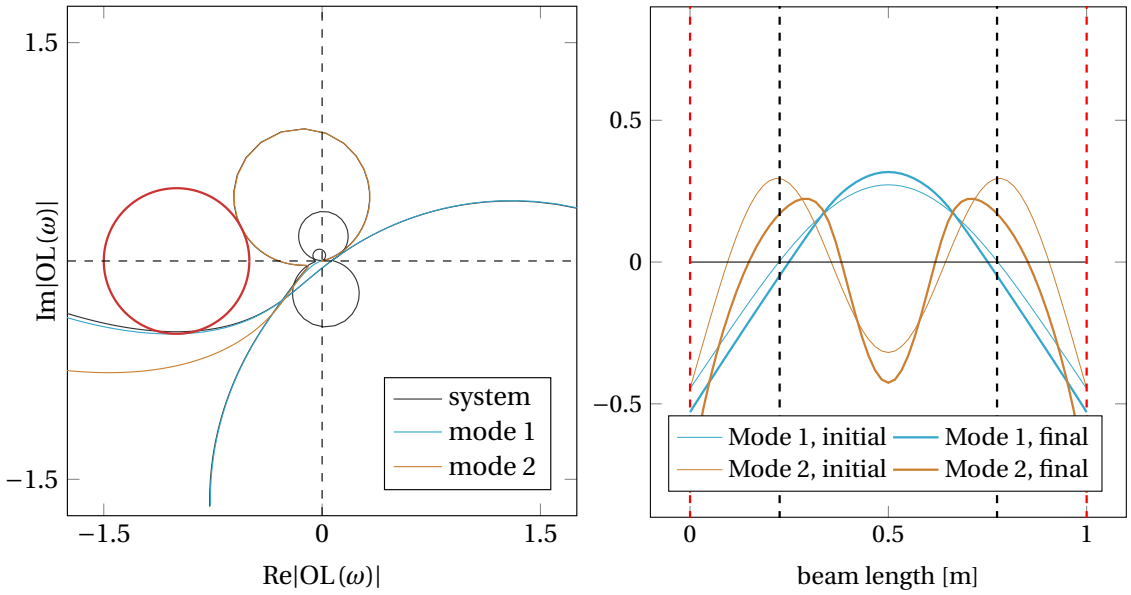

Figure 5.14: The final design of the beam height optimization problem B with fixed actuator and sensor configuration. (left) Nyquist plot of the open-loop system. (right) The mode shapes of the critical modes of the initial design and final design.

6

Conclusions and recommendations

6.1. Conclusions

The goal of this thesis has been to develop and test a new method for the design of controlled motion systems. The initial focus was to maximize the controller bandwidth by determining the actuator and sensor locations. The performance of placement criteria proposed in the literature in relation to controlled motion systems was investigated. Based on the conclusion that the criteria are not suited for designing high-performance motion systems it was decided to develop a method that includes control.

- Actuator and sensor placement criteria proposed in the literature, which was the starting point of this thesis, originate from two concepts. The concept of controllability and observability and the concept of energy norms like the $\mathscr{H}_2$-norm and $\mathscr{H}_\infty$-norm. In this thesis, it was shown with an example that the potential of these criteria in designing controlled motion systems is limited. The criteria contain information on the system's gain only while the stability and robustness of a motion system are determined by the gain and phase of the system. Including information on the system's phase gives a higher potential. There it is clear that a successful approach must include control.
- A new mathematical model that approximates the open loop of a controlled motion system was derived. The model is a set of transfer functions, each of which describes the open-loop response of an individual mode. Together, the transfer functions contain the open-loop response of the complete system. The robustness of each transfer function is a function of just three parameters. The accuracy of this approximation depends on the dynamics of other flexible modes present in the frequency range of the approximated mode, but the model was capable of decribing the critical modes in almost all 1D test cases well. The error of the approxation of one mode is independent of the approximations of the other modes, in other wordes the errors do not accumulate.
- Combinations of the three parameters for which the robustness is equal to a criterion was identified and resulted in a boundary surface. This boundary surface revealed areas with strong variations in gradients, especially if the frequency range of the mode dynamics is close to the bandwidth frequency. The boundary surface also revealed a discontinuity at the line where a system type changes from an anti-resonance followed by resonance to a resonance followed by an anti-resonance. A mathematical model using non-uniform rational B-splines (NURBS) of this surface allows fast evaluations of the robustness and sensitivities. The surface model is suited for gradient-based optimization methods.
- A new constraint regarding the robustness of the motion system is proposed. Instead of calculating the robustness of the complete system, each flexible mode is checked for robustness separately using the robustness response surface derived in this thesis. One advantage of this method is that the optimizer has information on the robustness of each mode separately. As a result, it shows well-performing optimization runs that converge to designs smoothly. The combination of the derived robustness response surface and a gradient-based optimization method contributes to stable convergence.
- The proposed method was used to generate designs by optimizing the actuator and actuator/sensor locations in a motion system. The optimizer converged to unconventional solutions where the positions did not coincide with the nodes of the modes in consideration. In each design, constraints of two

or more flexible modes were active. These observations differ from the common engineering principle to locate an actuator or sensor at the node of one of the first few modes. The optimized designs were compared with designs with sensor and actuator locations at the nodes. The proposed method results in designs with higher performance. However, sometimes the optimizer converges to a local optimum that performs less compared to a system obtained using engineering design principles. Setting the design obtained using engineering principles as the initial design for the optimizer results in an improved optimized design.

6.2. Recommendations

The result of this study is that the proposed method has great potential in designing motion systems. The method uses gradient-based optimization in which the robustness of a motion system is satisfied indirectly by ensuring the robustness of each mode individually. One benefit of the method is that it results in well-performing optimization runs that converge to feasible designs. Also, the use of a derived robustness response surface allows for gradient-based optimization methods. What follows are a few topics that are interesting for future research and development.

- The accuracy of the single-mode system model reduces for modes that are not well-spaced. One interesting idea to explore is to increase the model accuracy by appending the model with the model of the preceding and succeeding modes. The robustness constraint surfaces can then no longer be used anymore to evaluate the single-mode system for robustness. This will be done differently. However, the robustness is still evaluated for each mode individually which is beneficial for optimization. The single-mode model that resembles the open-loop in the frequency range of that mode will not be too complex.

- Another interesting idea to investigate is to develop a strategy to select initial designs for optimization. Especially the initial controller bandwidth is worth investigating. The optimization works well if the initial bandwidth is lower than the eigenfrequency of the first mode, but the optimizer likely converges to a local optimum. If the initial bandwidth is set relatively high and the initial design is not feasible, the optimizer might not converge.

- One method of designing motion systems is to maximize the first or a set of eigenfrequencies of the structural part via topology optimization. This approach focuses on the structure, and control is not taken into account. A very interesting idea to investigate a new formulation for designing motion systems is to include the anti-resonance frequency in the topology optimization. One example is to minimize the difference between the resonance and anti-resonance frequency of one mode, which is a measure of the magnitude of α.

- The proposed method has only been tested on a 1D test case. The error of the approximation can become unacceptable if mode dynamics interfere too much. It is known that the frequency density can increase as the dimension increases. It would be therefore interesting to investigate the performance of the method in a 2D and 3D case. 2D and 3D cases make topology optimization possible.

A

Design Cases

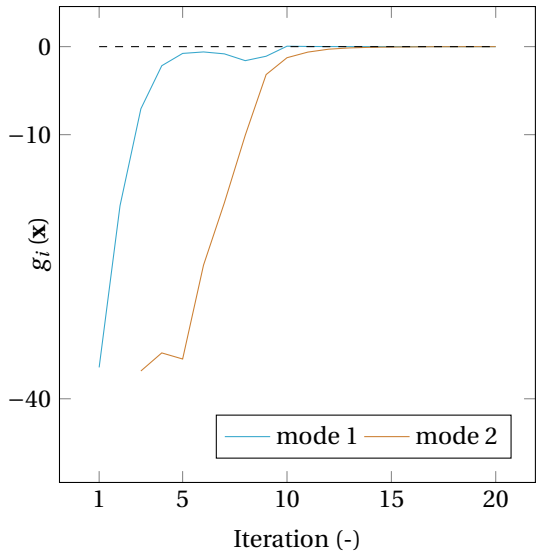

(a)

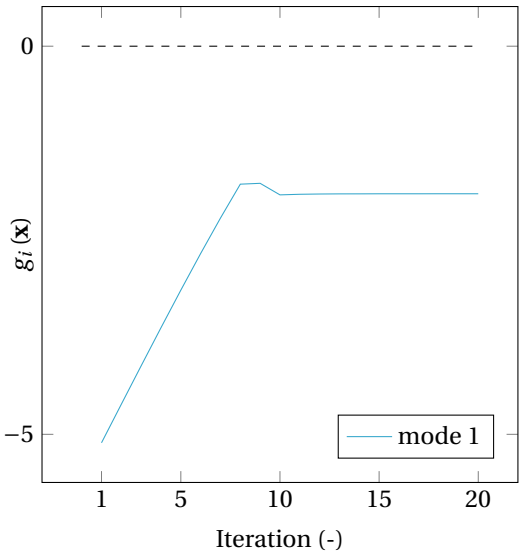

(b)

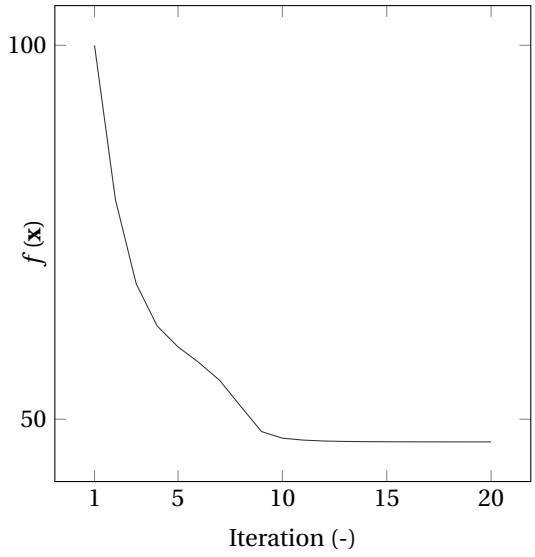

(c)

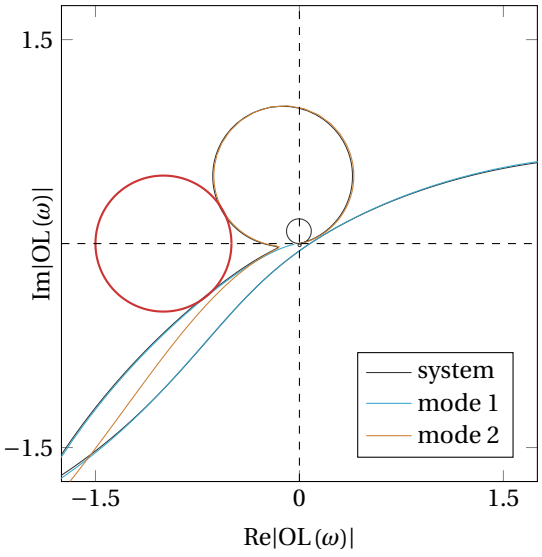

(d)

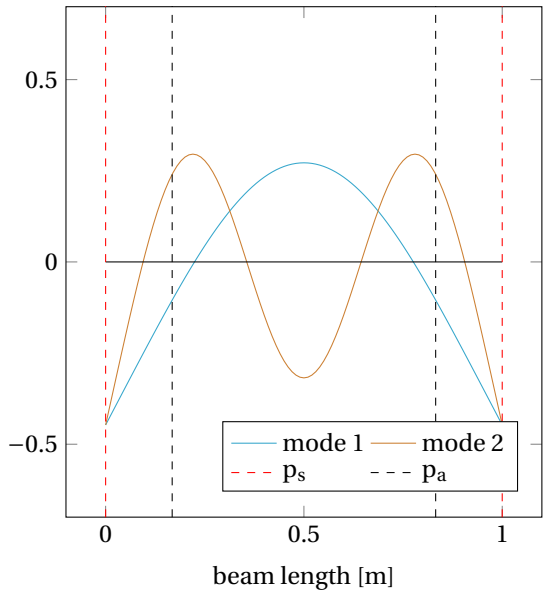

(e)

Optimization performance of design A of the actuator and sensor placement problem with an initial sensor location of $p_s = 0$ [m] and initial actuator location of $p_a = 0$ [m].(a) Robustness constraints with modes two and three as active constraints in the final design. (b) α constraints. (c) Objective functions. (d) Nyquist plot of the open-loop.

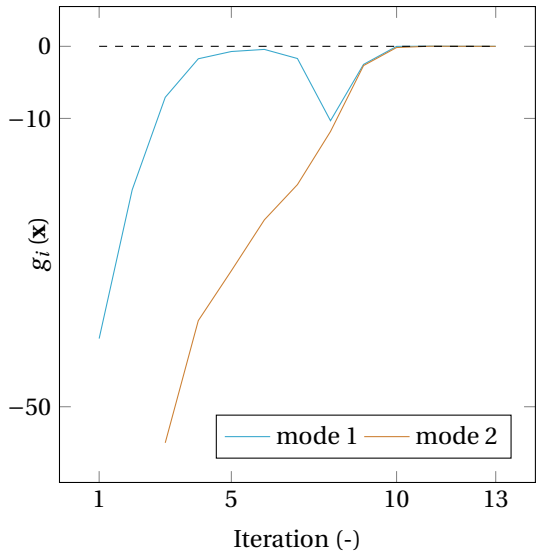

(a)

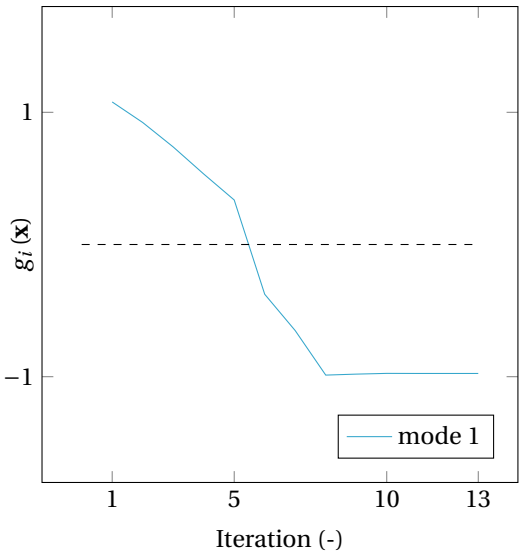

(b)

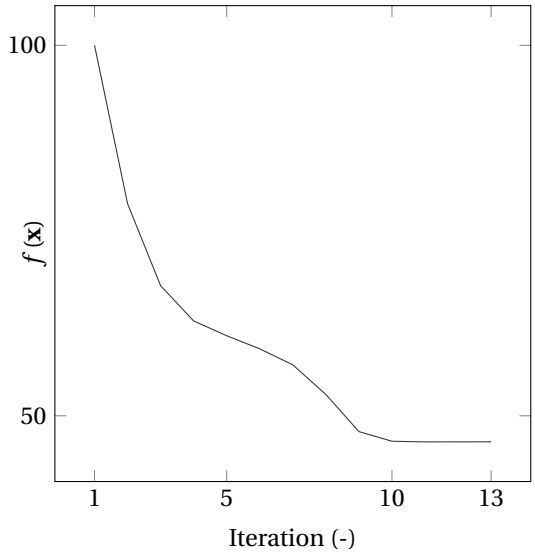

(c)

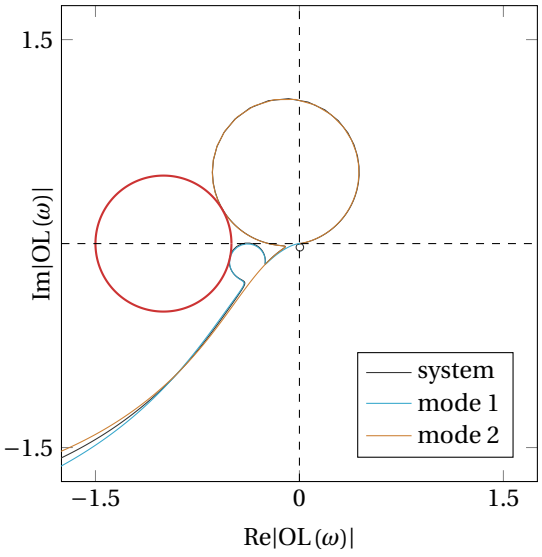

(d)

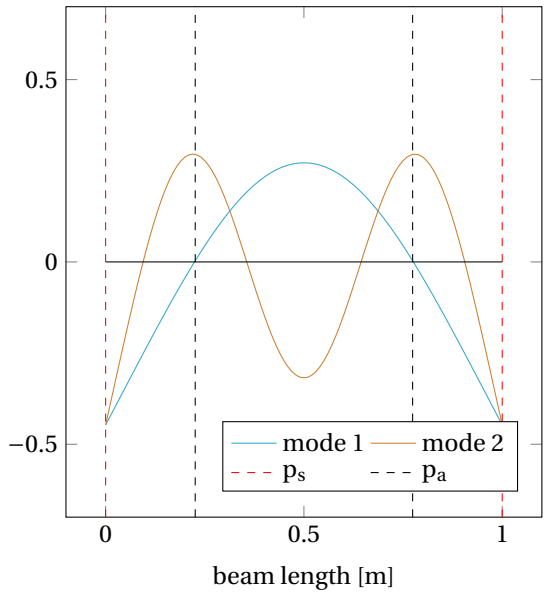

(e)

Optimization performance of design B of the actuator and sensor placement problem with an initial sensor location of $p_s = 0.1$ [m] and initial actuator location of $p_a = 0.4$ [m].(a) Robustness constraints with modes two and three as active constraints in the final design. (b) α constraints. (c) Objective functions. (d) Nyquist plot of the open-loop.

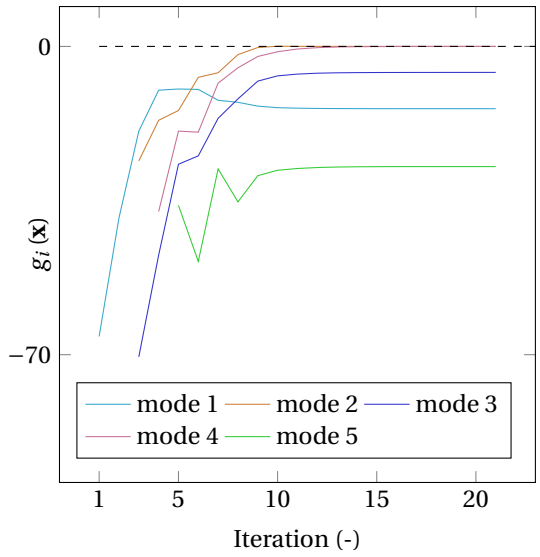

(a)

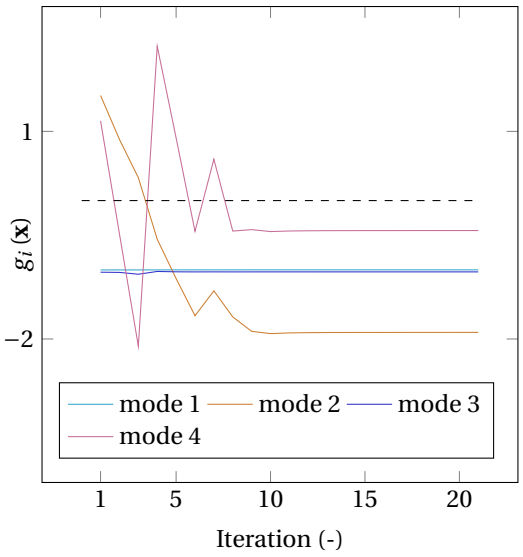

(b)

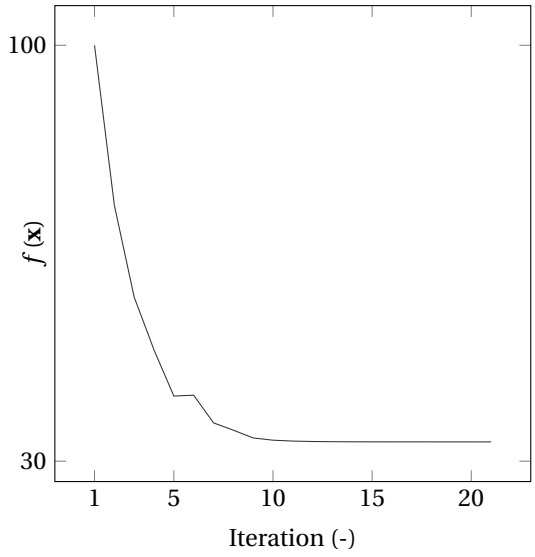

(c)

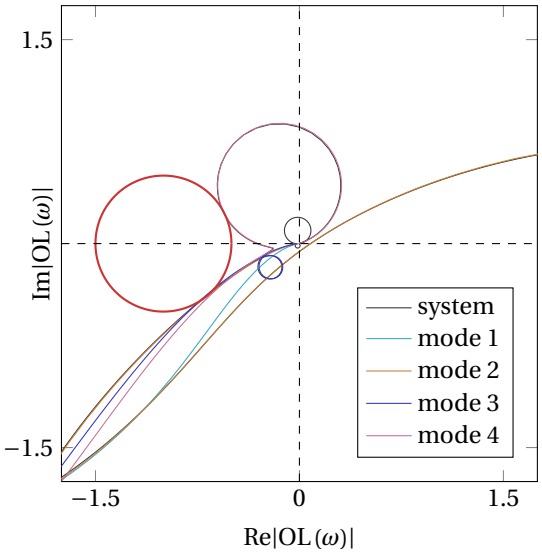

(d)

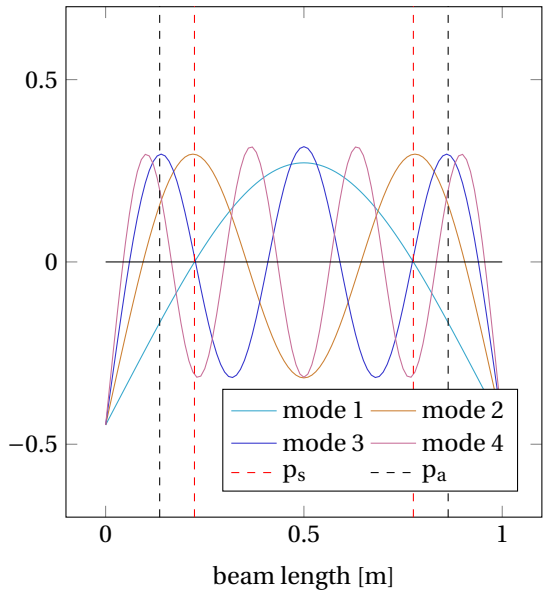

(e)

Optimization performance of design D of the actuator and sensor placement problem with an initial sensor location of $p_s = 0.224$ [m] and initial actuator location of $p_a = 0$ [m].(a) Robustness constraints with modes three and four as active constraints in the final design. (b) α constraints. (c) Objective functions. (d) Nyquist plot of the open-loop.

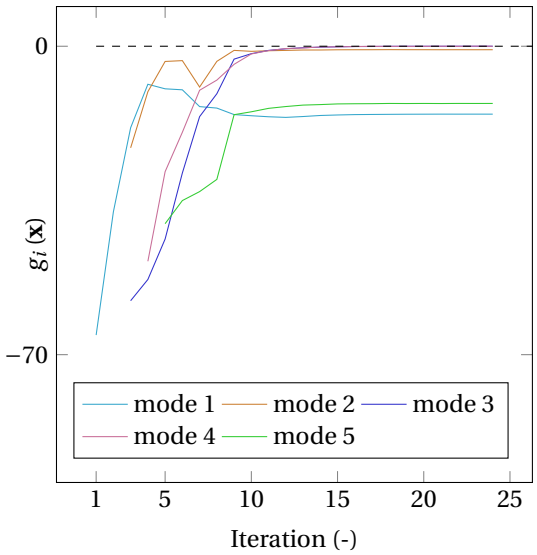

(a)

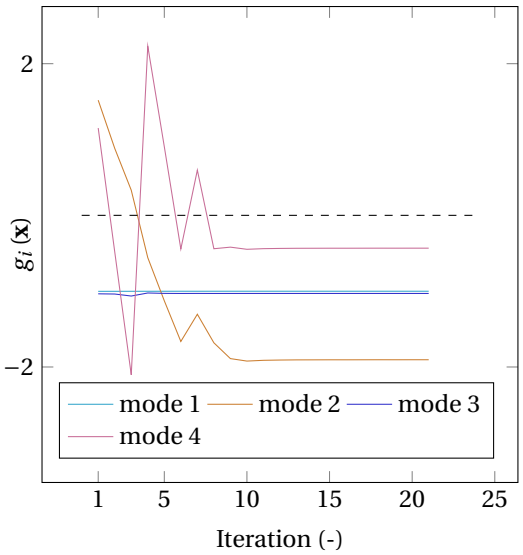

(b)

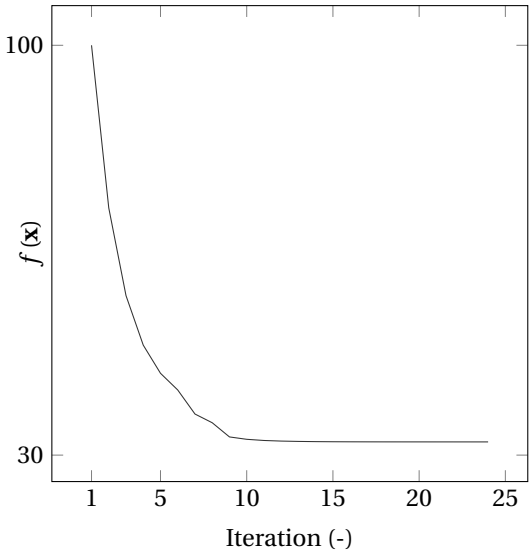

(c)

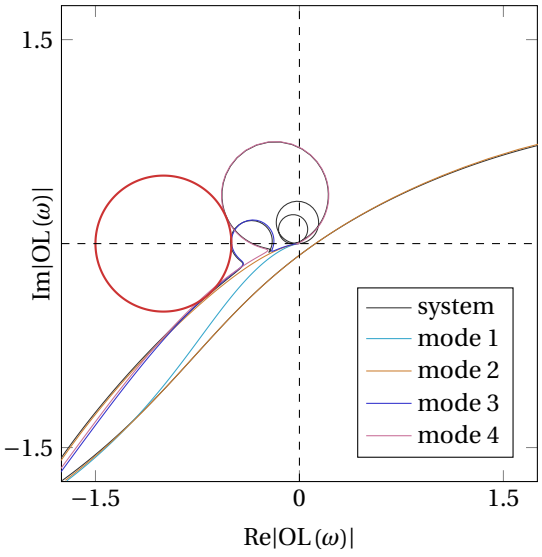

(d)

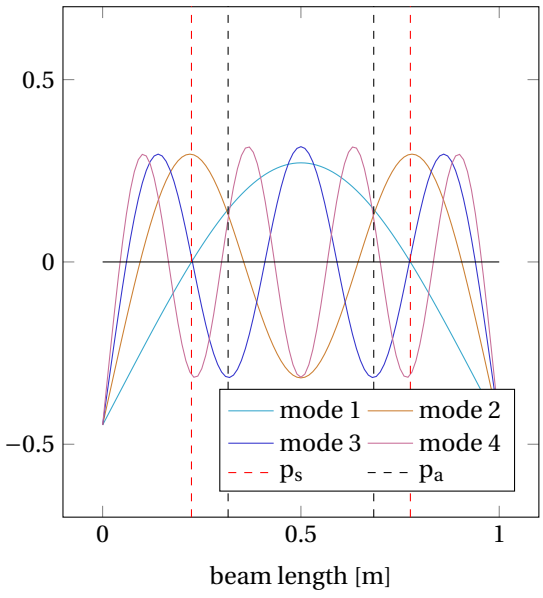

(e)

Optimization performance of design E of the actuator and sensor placement problem with an initial sensor location of $p_s = 0.224$ [m] and initial actuator location of $p_a = 0.5$ [m].(a) Robustness constraints with modes two and three as active constraints in the final design. (b) α constraints. (c) Objective functions. (d) Nyquist plot of the open-loop.

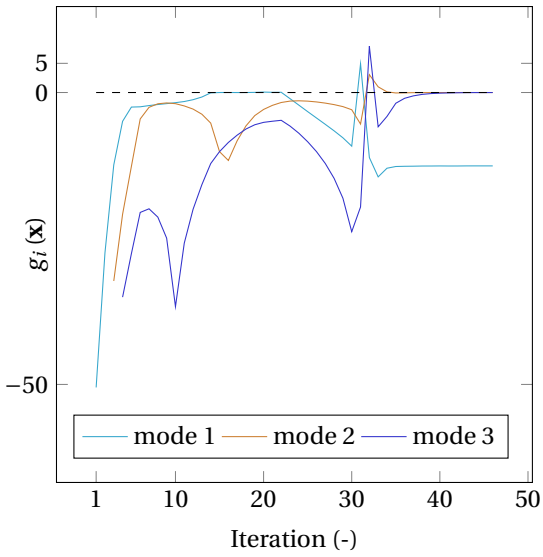

(a)

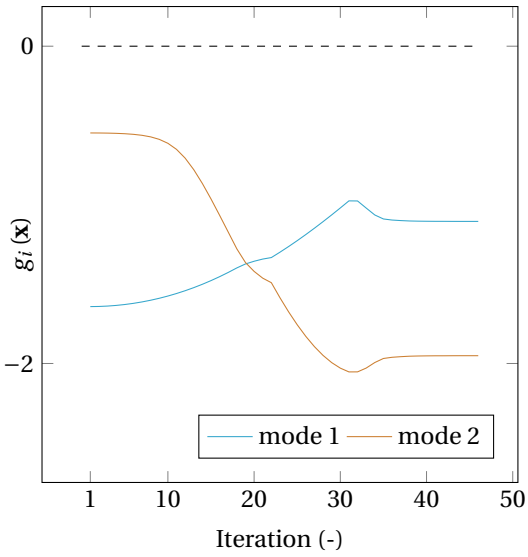

(b)

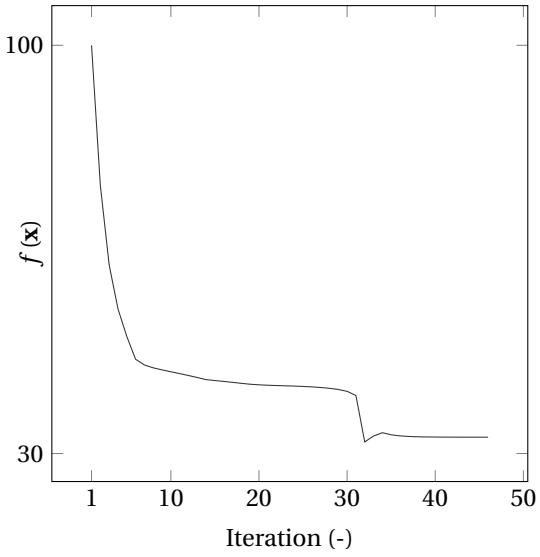

(c)

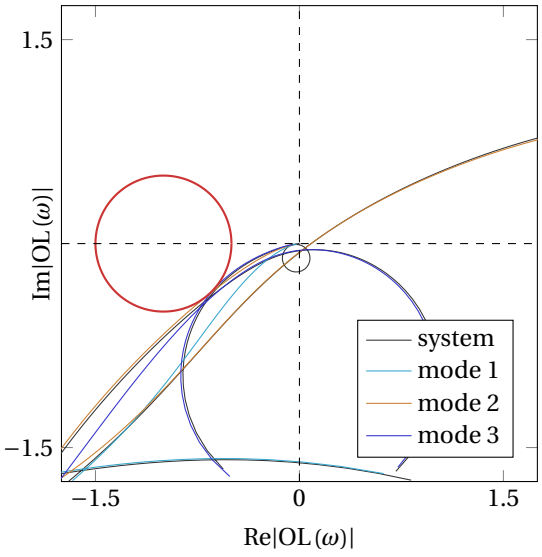

(d)

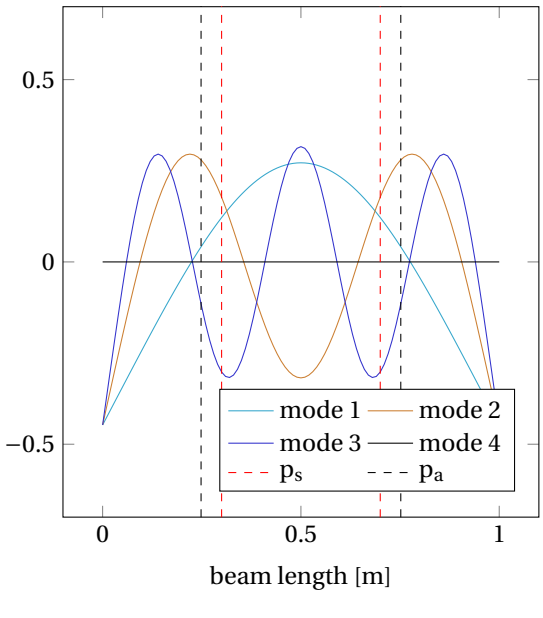

(e)

Optimization performance of design F of the actuator and sensor placement problem with an initial sensor location of $p_s = 0.3$ [m] and initial actuator location of $p_a = 0$ [m].(a) Robustness constraints with modes two and three as active constraints in the final design. (b) α constraints. (c) Objective functions. (d) Nyquist plot of the open-loop.

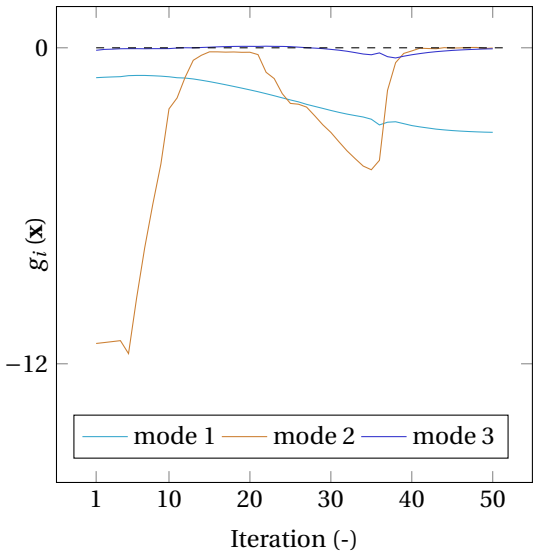

(a)

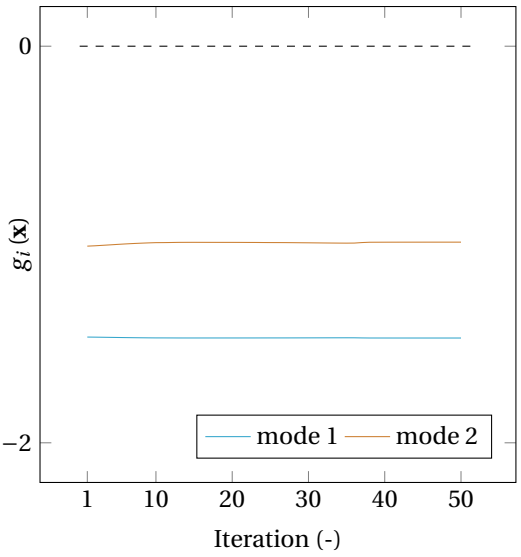

(b)

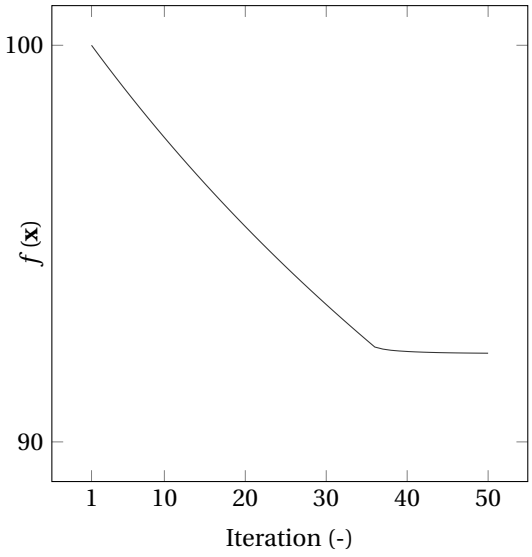

(c)

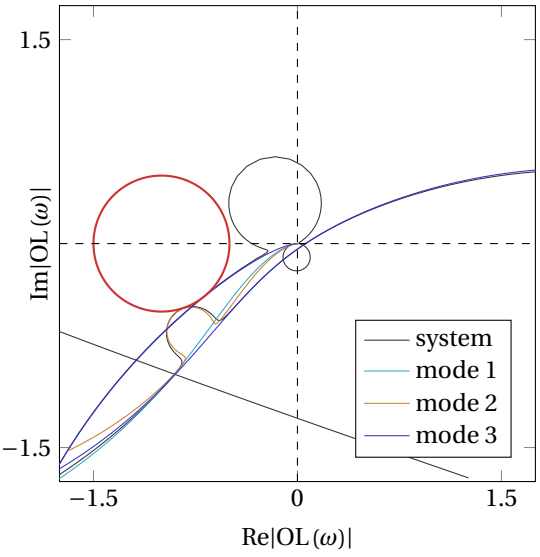

(d)

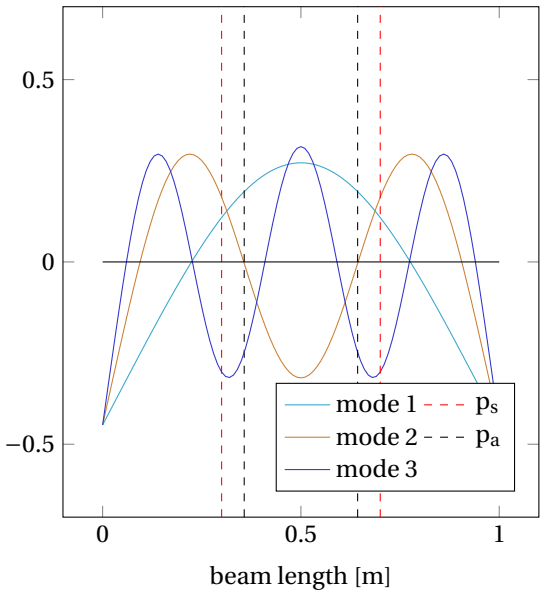

(e)

Optimization performance of design H of the actuator and sensor placement problem with an initial sensor location of $p_s = 0.335$ [m] and initial actuator location of $p_a = 0.357$ [m].(a) Robustness constraints with modes two and three as active constraints in the final design. (b) α constraints. (c) Objective functions. (d) Nyquist plot of the open-loop.

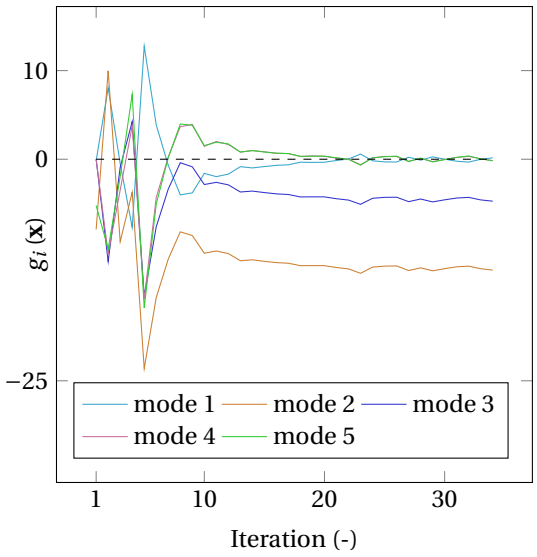

(a)

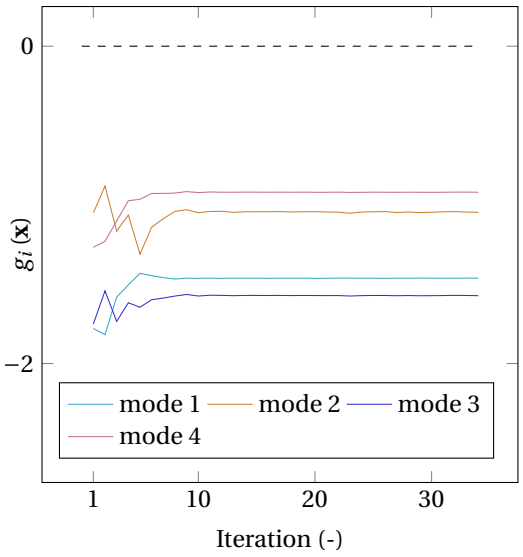

(b)

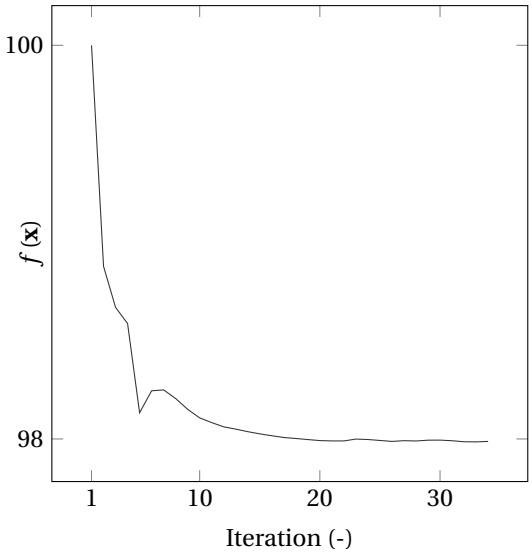

(c)

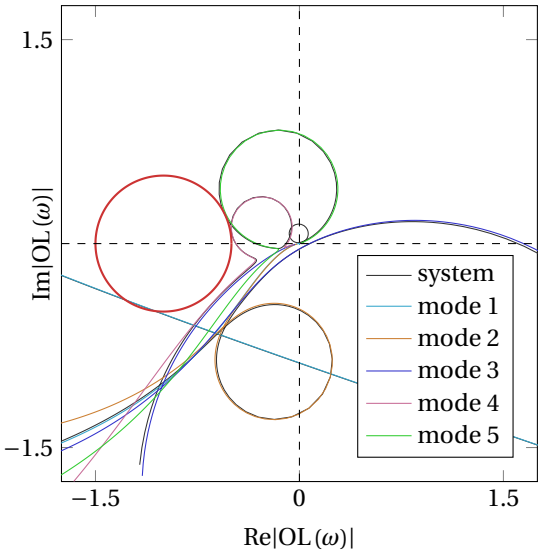

(d)

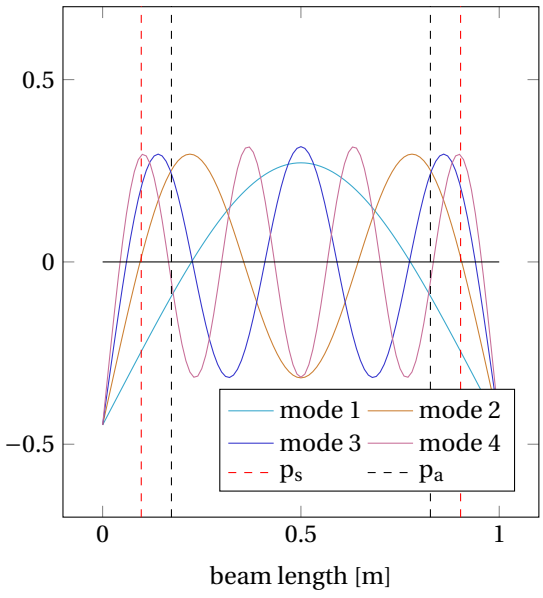

(e)

Optimization performance of design C of the actuator and sensor placement problem with an initial sensor location of $p_s = 0.1$ [m] and initial actuator location of $p_a = 0.4$ [m].(a) Robustness constraints with modes two, three, and four as active constraints in the final design. (b) α constraints. (c) Objective functions. (d) Nyquist plot of the open-loop.

Bibliography

[1] Onur Rauf Bingol and Adarsh Krishnamurthy. Nurbs-python: An open-source object-oriented nurbs modeling framework in python. *SoftwareX*, 9:85–94, 2019.

[2] Hans Butler. Position control in lithographic equipment [applications of control]. *IEEE Control Systems Magazine*, 31(5):28–47, 2011.

[3] Richard C Dorf and Robert H Bishop. *Modern control systems*. Pearson, 2011.

[4] Wodek Gawronski. *Advanced structural dynamics and active control of structures*. Springer Science & Business Media, 2004.

[5] Didier Georges. The use of observability and controllability gramians or functions for optimal sensor and actuator location in finite-dimensional systems. In *Proceedings of 1995 34th IEEE Conference on Decision and Control*, volume 4, pages 3319–3324. IEEE, 1995.

[6] A Hać and L Liu. Sensor and actuator location in motion control of flexible structures. *Journal of sound and vibration*, 167(2):239–261, 1993.

[7] Raphael T Haftka and Zafer Gürdal. *Elements of structural optimization*, volume 11. Springer Science & Business Media, 2012.

[8] Thomas JR Hughes. *The finite element method: linear static and dynamic finite element analysis*. Courier Corporation, 2012.

[9] Young W Kwon and Hyochoong Bang. *The finite element method using MATLAB*. CRC press, 2018.

[10] Eugene TY Lee. Choosing nodes in parametric curve interpolation. *Computer-Aided Design*, 21(6):363–370, 1989.

[11] Leonard Meirovitch. Analytical methods in vibrations. 1967.

[12] SOR Moheimani and Tom Ryall. Considerations on placement of piezoceramic actuators that are used in structural vibration control. In *Proceedings of the 38th IEEE Conference on Decision and Control (Cat. No. 99CH36304)*, volume 2, pages 1118–1123. IEEE, 1999.

[13] Kirsten Morris, Michael A Demetriou, and Steven D Yang. Using H2-control performance metrics for the optimal actuator location of distributed parameter systems. *IEEE Transactions on Automatic Control*, 60 (2):450–462, 2015.

[14] PC Müller and HI Weber. Analysis and optimization of certain qualities of controllability and observability for linear dynamical systems. *Automatica*, 8(3):237–246, 1972.

[15] Richard Murray and Scott Livingston. Python control systems library. *URL: http://python-control. readthedocs. io/en/latest/index. html*, 2018.

[16] Tom Oomen. Advanced motion control for precision mechatronics: Control, identification, and learning of complex systems. *IEEJ Journal of Industry Applications*, 7(2):127–140, 2018.

[17] Panos Y Papalambros and Douglass J Wilde. *Principles of optimal design: modeling and computation*. Cambridge university press, 2000.

[18] Les Piegl and Wayne Tiller. *The NURBS book*. Springer Science & Business Media, 1996.

[19] Adrian Mathias Rankers. Machine dynamics in mechatronic systems: An engineering approach. 1998.

[20] R Munnig Schmidt, Georg Schitter, and Adrian Rankers. *The Design of High Performance Mechatronics-: High-Tech Functionality by Multidisciplinary System Integration*. Ios Press, 2020.

[21] Ole Sigmund and Kurt Maute. Topology optimization approaches. *Structural and Multidisciplinary Optimization*, 48(6):1031–1055, 2013.

[22] Krister Svanberg. The method of moving asymptotes—a new method for structural optimization. *International journal for numerical methods in engineering*, 24(2):359–373, 1987.

[23] Krister Svanberg. The method of moving asymptotes-modelling aspects and solution schemes. *Lecture Notes for the DCAMM course Advanced Topics in Structural Optimization*, 1998.

[24] Gijs van der Veen, Matthijs Langelaar, Stan van der Meulen, Dick Laro, Wouter Aangenent, and Fred van Keulen. Integrating optimization in precision motion system design for optimal closed-loop control performance. *Mechatronics*, 47:1–13, 2017.

[25] Guido Van Rossum and Fred L. Drake. *Python 3 Reference Manual*. CreateSpace, Scotts Valley, CA, 2009. ISBN 1441412697.

[26] Jing Wang, Ming Zhang, Yu Zhu, Kaiming Yang, Xin Li, and Leijie Wang. Simultaneous optimization in ultra-precision motion systems. *Structural and Multidisciplinary Optimization*, 59(6):2273–2285, 2019.

[27] Wei-Cheng Xie, Xiu-Fen Zou, Jian-Dong Yang, and Jie-Bin Yang. Iteration and optimization scheme for the reconstruction of 3D surfaces based on non-uniform rational B-splines. *Computer-Aided Design*, 44 (11):1127–1140, 2012.

[28] Qing Zheng and Zhiqiang Gao. Motion control design optimization: problem and solutions. *International Journal of Intelligent Control and Systems*, 10(4):269–276, 2005.

[29] Kemin Zhou, John Comstock Doyle, Keith Glover, et al. *Robust and optimal control*, volume 40. Prentice hall New Jersey, 1996.